



TESIS DOCTORAL

IDENTIFICATION OF COHERENT MAGNETO-HYDRODYNAMIC MODES AND TRANSPORT IN PLASMAS OF THE TJ-II HELIAC

Autor:

Baojun Sun

Directores:

Daniel López Bruna

María Antonia Ochando García

Tutor:

Víctor Tribaldos Macía

DEPARTAMENTO DE FISICA

Leganés, septiembre de 2016



Universidad
Carlos III de Madrid
www.uc3m.es

[a entregar en la Oficina de Posgrado, una vez nombrado el Tribunal evaluador , para preparar el documento para la defensa de la tesis]

TESIS DOCTORAL

IDENTIFICATION OF COHERENT MAGNETO-HYDRODYNAMIC MODES AND TRANSPORT IN PLASMAS OF THE TJ-II HELIAC

Autor: Baojun Sun

Directores: Daniel López Bruna
Maria Antonia Ochando Garcia

Firma del Tribunal Calificador:

Firma

Presidente: (Nombre y apellidos)

Vocal: (Nombre y apellidos)

Secretario: (Nombre y apellidos)

Calificación:

Leganés/Getafe, de de

Acknowledgements

Once I recalled, the motivation that drove me to change major to fusion was twofold: 1. I saw fusion as the ultimate resource of energy and I expected to witness the construction of ITER; 2. I had the curiosity, the beliefs and the expectation. Chinese philosopher Chuang Tzu, said “newborn calves are not afraid of tigers”, this quote may describe my 5 year adventure. “Being as a newborn calf” makes me to be in trouble but also helps me to get out.

What is PhD? In the beginning, I didn't make myself this question seriously. As a newborn calf, I believed PhD as a chance and thought my PhD would innovate the research field. After about two years of turmoil, the question came again, what is PhD? I started to think PhD was about solving a unanswered question. My story was nearly ended there at that moment, but I was a lucky man, since I met with Daniel López Bruna (Daniel) and María Antonia Ochando García (Marian), and later on they became my Thesis directors. Daniel gave me a lot of supports, enough energy to push forward and more importantly, freedom to think. As to Marian, I am fully indebted, she shared her most valuable data, idea and knowledge with me. Moreover she taught me how to think, what to ask, when to stop, most importantly, the art of asking 'why'. Finally Marian and Daniel guided me to publish two journal papers, four conference papers, and this PhD thesis. A great honor to me.

My story ends here. So the question comes up again, what is PhD? Specifically, it is about finding a way out in a field, or more broadly, it can be viewed as an entrepreneurship training in the academic world. But there is a sad truth inside, you need to be lucky and to have the chance to meet people like Marian along the way.

Finally, I would like to thank all members of TJ-II team for providing me this broad research stage, limitless knowledge, insightful ideas, tons of experimental data support. I want to give my special thank to Carlos Hidalgo and to Francisco Castejón who made possible that I could join TJ-II. I am also indebted to professors in Universidad Carlos III de Madrid, especially Prof. José Ramón Martín Solís who managed plasma and nuclear fusion doctoral program, and Prof. Víctor Tribaldos Macía, my Thesis tutor, who taught and supported me in the university. I would also like to thank José Luis Velasco who taught me plasma physics and orbits computing. Furthermore, I appreciate all the help from Rocío Pañero Martín for her fabulous secretary work for our PhD students. Last but not least, I

want to thank my office mate and colleague Pedro Monreal for helping me to solve my linux troubles and for the fruitful discussions throughout my PhD here.

This work has been supported by China Scholarship Council (CSC) and the Spanish Government via the “Programa Estatal de Fomento de la Investigación Científica y Técnica de Excelencia” (ENE2014-52174-P).

Abstract

Magneto hydrodynamic (MHD) instabilities in magnetically confined plasmas are responsible for different phenomena of relevance in the transport of particles and energy. Plasma oscillations can limit the operational space of most experimental devices, therefore their study and understanding may lead to find the way to control them and achieving better plasma performance.

In the flexible heliac device TJ-II, an almost current-free and low magnetic shear stellarator, collective oscillations are commonly observed in plasmas heated with microwave or neutral particle beams. Frequently, low mode number oscillations, systematically linked to low order rational values of the rotational transform (namely, to their associated magnetic islands chain), are found to lead fast-particle and/or thermal-plasma confinement degradation. The present work summarizes some studies performed in the TJ-II stellarator to investigate the role of magnetic islands dynamics in plasma confinement.

Tearing mode (TM) activity is often detected as intense and coherent modes in Mirnov coils signal spectra during the low-confinement phase (L-mode) of neutral beam (NBI) heated plasmas. Their rotation speed is generally close to the plasma flow velocity and the resolved mode numbers correspond to the lowest rational values contained in the rotational transform profile of each magnetic configuration, so the measured mode frequencies are rather low (tens of kHz) and scale with their poloidal mode number. Nevertheless, under co-NBI heating (that flattens the magnetic shear profile), the rotating structures can become faster than the plasma flow, apparently driven by an additional velocity in the electron diamagnetic drift direction. At some critical plasma conditions dependent on plasma profiles, the TM may change their stable behaviour into a pulsed magnetic activity. Mirnov coil signals show repeated magnetic bursts and their spectrograms reveal that stable modes change into intermittent (with ≈ 1 ms repetition period) frequency stripes starting at around doubled frequency and rapidly (≈ 0.3 ms) decreasing to frequencies slightly above the stable rotation value. Coinciding with the magnetic pulses, collapses of small intensity local transport barriers are observed, akin to minor disruptions, and during the magnetic fluctuations-free periods, barriers build up again. This cyclic process, resembling an ELM-like phase, can be sustained, if heating and/or fuelling are not modified. As well, rotating islands, which in essence provide a wave for

the magnetic components, can interact with shear Alfvén waves giving rise to new coherent modes. This new coupling of TM with Alfvén waves has been identified for the first time in TJ-II in L-mode plasmas under full NBI power (≈ 0.9 MW).

On the other hand, magnetic islands can be locked in the laboratory frame, as is the magnetic field itself in stellarators. The interaction of shear-Alfvén waves with static magnetic island chains might open new gaps in the continuum spectrum, which would enable for the existence of weakly damped Alfvénic modes. This kind of wave coupling, MIAEs (magnetic island induced Alfvén eigenmode), has been proposed to explain the origin of some Alfvénic waves in the intermediate frequency range ($f_{TM} < f < f_{HAE}$) during NBI heating in TJ-II.

Acoustic like modes with frequencies in the range of 15-40 kHz have been first identified in TJ-II during Electron Cyclotron Resonance (ECR) heating, where a considerable population of fast electrons is generated. They exhibit standing wave like behaviour in the poloidal plane, as geodesic acoustic modes (GAM), but propagate at around the ion sound speed in the toroidal direction, as ion sound waves (ISW). Their fundamental mode number is ($m=2, n=1$), and frequency scales with acoustic speed. Modes can be occasionally bursting in intensity with rapid decreases in frequency ($\approx 20\%$), in coincidence with pulses of fast electron lost from the plasma core, which may suggest a nonlinear interaction of acoustic mode with fast electrons in velocity space. The necessary condition for exciting the acoustic modes is having finite size low-order magnetic islands in the plasma bulk, likely because the long confinement time of fast electrons in the vicinity of islands favours wave-fast electron interaction.

The results of the studies described in this thesis show that rational surfaces may help to regulate plasma transport due to the multiple means that they interact with thermal plasma, fast particle populations, and plasma waves. We hope that this work can contribute to future stellarator design and operation procedures.

Table of contents

List of figures	ix
1 Introduction	1
1.1 Rotational transform and magnetic island	3
1.1.1 Island impacts on toroidal fusion devices	4
1.2 The TJ-II Stellarator	5
1.3 Operation of TJ-II stellarator	6
1.3.1 Selective diagnostic layout	9
1.4 Overview of the work: Collective plasma oscillations and rational surfaces in TJ-II	10
2 Magnetic island dynamics in NBI plasma	13
2.1 Introduction	13
2.2 Overview of island dynamics phenomena	15
2.3 Steady rotation mode: Islands in plasma frame	18
2.3.1 Frequency scaling	18
2.3.2 Local electron temperature evolution	19
2.4 Bursting-chirping mode: Drifting islands in plasma frame	22
2.4.1 Frequency scaling in chirping mode	22
2.4.2 Relation between bursts and transport barrier breaking	23
2.5 Discussion	28
3 Alfvén wave including magnetic island effect	31
3.1 Introduction	31
3.2 Phenomenological aspects	33
3.3 Models for low-frequency AEs in TJ-II plasmas	36
3.3.1 Global Alfvén eigenmode above maximum of continuum spectrum	37
3.3.2 Alfvén eigenmode induced by stationary magnetic islands (MIAE) .	38

3.4	Experimental identification of GAE and MIAE	40
3.5	Coupling between rotating islands and shear-Alfvén waves	49
3.6	Discussion	53
4	Acoustic mode driven by fast electrons in ECR plasma	63
4.1	Introduction	63
4.2	Experimental setup and general features	64
4.2.1	Configuration dependence: island in the periphery	66
4.2.2	Density independence	67
4.2.3	Mass to charge ratio and electron temperature dependence	67
4.3	Identification of acoustic mode	69
4.4	Acoustic mode structure and its harmonics	74
4.5	Density limit for acoustic mode in relation to island unlocking	77
4.6	Discussion	79
5	Summary and discussion	81
	References	83

List of figures

1.1	Schematic view of tokamak concept. Toroidal field is generated by toroidal field coils, and magnetic field is only formed when plasma current is driven along the toroidal direction. Poloidal field coils are used to control plasma shape and axis position. Picture is from URL www.euro-fusion.org	3
1.2	Schematic view of TJ-II with toroidal, vertical and central coils in blue, helical coil in orange, and plasma in purple. Picture source: http://fusionwiki.ciemat.es/wiki/TJ-II	6
1.3	Measurement vs. Calculation. a) N=4, M=3; b) N=8, M=5; c) N=3, M=2.	7
1.4	Examples of electron temperature and density profiles during ECR a) and NBI b) heating.	8
1.5	Solid lines: rotational transform profiles used in TJ-II discharges; dotted lines: ι profiles modified by 1 kA current of a given shape; dashed curved line: ι profile modified by assuming -4 kA current; dashed horizontal lines indicate the lowest rational numbers.	9
1.6	a) Top view of TJ-II showing the position of several diagnostics and its heating systems; b) bolometer arrays in sector B7; c) poloidal array of Mirnov coils sited between sector D4 and D5 ($\phi = 45^\circ$).	11
2.1	TJ-II discharges #18998 (a-c) and #18997 (d-f). (a)&(d) Cross-power and (b)&(e) cross-phase spectrograms of Mirnov coil signals; (c)&(f) line average density \bar{n}_e , diamagnetic energy W_{dia} , H_α signal, and magnetic fluctuations ($5 \text{ kHz} \leq f \leq 100 \text{ kHz}$). Grey shading indicates plasma in L-mode, blue for H-mode, pink for an intermediate state characterized by bursting modes (see also figure 2.2.)	16
2.2	Detail of figure 2.1 for discharge #18997 around the establishment of the bursting mode, where its chirping nature can be appreciated in correlation with H_α pulses.	17

2.3	Frequency scaling with poloidal mode number in L-mode plasma during NBI heating. The shaded area covers values expected from ExB rotation.	19
2.4	NBI heated discharge # 37734 during a low density phase ($\bar{n}_e \approx 0.7 \times 10^{19} \text{ m}^{-3}$) and net plasma current $I_p \sim -4 \text{ kA}$. (a) Power spectrogram of magnetic fluctuations; (b) cross power spectrogram of two ECE channel signal, ECE3 ($\rho = 0.53$) and ECE4 ($\rho = 0.45$); (c) Fluctuations of these same ECE traces and magnetic fluctuations in the frequency band 9–13 kHz; and (d) line density and electron temperature at the indicated radii.	20
2.5	Zoom in of temperature fluctuations at $\rho = 0.53$ and $\rho = 0.45$ in figure 2.4c around $t = 1012 \text{ ms}$ (a) and $t = 1123 \text{ ms}$ (b).	21
2.6	Frequency scaling with poloidal mode number of the bursting chirping mode in NBI plasmas. Two fits are shown for the highest (red circles) and lowest (blue crosses) frequencies covered by the chirping. Coloured triangles indicate the frequency ranges expected for rotation with the u_E or $u_E + u_{*e}$ velocities.	22
2.7	TJ-II discharge #38555. (a) Cross-power and cross-phase (b) spectrograms of Mirnov coil data; (c) plasma parameters: \bar{n}_e , diamagnetic energy, H_α and Mirnov coil signals. The grey-shaded region indicates H-mode. (d) Detail of an MHD burst at the indicated times.	24
2.8	TJ-II discharge #38555. Time evolution of the electron temperature and radiation emissivities from different radii (labelled) showing the existence of a pivot point around mid minor radius; and Mirnov-coil signal ($5 \text{ kHz} \leq f \leq 100 \text{ kHz}$).	26
2.9	Discharge #39307 with $\iota = 3/2$ around $\rho = 0.5$. Time traces of: radiation emissivities from the indicated radii, Mirnov-coil signal ($5 \text{ kHz} \leq f \leq 100 \text{ kHz}$ frequency band) and V_{fl} from Langmuir probes at $\rho = 0.91$, $\rho = 0.89$ and $\rho = 0.87$. Shaded regions mark the longest time windows of H-mode.	27
2.10	TJ-II discharge #38776. (a) Spectrogram of Mirnov coil data; (b) line average density, H_α , diamagnetic energy and Mirnov-coil ($5 \text{ kHz} \leq f \leq 100 \text{ kHz}$) signals.	29
3.1	NBI heating phase in TJ-II discharge #28158. Spectrograms of Mirnov coil a) and bolometer b) signals. Mode labelled 1 has poloidal number $m = 5$ and is related with the rotation of $\iota = 8/5$ islands in the near edge region. Modes 2 and 3 are Alfvénic. c) Net toroidal current I_p , line-averaged density \bar{n}_e and H_α . A vertical line indicates the firing of the Thomson Scattering laser.	35

3.2	Shear Alfvén continuum spectrum for low mode number modes ($m < 9$) that below 400 kHz in #28158 at time $t=1200$ ms	36
3.3	Schematic plot of TJ-II rotational transform profile, typical peaked density profile (thin black line), and corresponding (m, n) continuum spectrum (thick black line). A local maximum ω_{\max} appears at $t = t_g$ around $\rho = 0.6$. The profiles are normalised using centre values of the density, n_{e0} , and angular frequency, ω_{A0}	38
3.4	Schematic plot of the continuum spectrum in t -frame: coupling of modes (m_1, n_1) and (m_2, n_2) satisfying the condition $M = m_1 + m_2$, $N = n_1 + n_2$ (solid lines); and continuum spectrum for each single mode (dashes). The coupling zone is the vicinity of the rational surface $t_{is} = N/M$	39
3.5	TJ-II discharge #28275 during co-NBI heating. a) Spectrogram of a bolometry chord with impact parameter $\rho = 0.84$, and predicted frequencies (dashed lines) for shear-Alfvén (2,3) coupled to (5,8) for mode 1, and single (5,8) for mode 2. A vertical line is drawn where mode 2 appears just after mode 1 disappears. The $M = 5$ low frequency mode (≈ 20 kHz) is due to island rotation. b) Net toroidal current I_p , line-averaged density and H_α time traces. The firing of the Thomson Scattering laser is indicated.	41
3.6	Intensity of modes 1 and 2 (figure 3.5) detected by bolometer chords with different impact parameters: ABOL1 ($\rho = 0.84$), ABOL2 ($\rho = 0.66$) and ABOL3 ($\rho = 0.51$).	42
3.7	a) Low mode number ($m < 10$) shear-Alfvén continuum spectra in discharge #28275. Natural frequency gaps HAE and GAE are indicated by solid red circles and horizontal line respectively. A dashed circle indicates a possible MAIE. b) Detail of modes $(m_1 = 2, n_1 = 3)$ –blue– and $(m_2 = 5, n_2 = 8)$ –red– calculated using the cylindrical model (solid lines) and STELLGAP (dashed) at Thomson Scattering time, see figure. 3.5. Two short horizontal lines indicate the coupling zone around the magnetic island $M = 7, N = 11$	43
3.8	Poloidal mode number analysis of mode 1 ($f \approx 100$ kHz) within time 1240-1242 ms in figure 3.5 based on an array of Mirnov coils.	44
3.9	NBI heating phase in TJ-II discharge #30092. a) Coherent Alfvén waves with frequencies between 80 kHz and 200 kHz in the spectrogram of a Mirnov coil. Two less coherent modes below 30 kHz are related with the $t = 3/2$ rational surface and have respective mode numbers $M = 2$ and $M = 4$. b) Time evolution of net toroidal current I_p , line-averaged density and H_α light.	46

3.10	Continuum spectrum calculated from STELLGAP for TJ-II discharge #30092 at $t = 1170$ ms assuming that ι is modified with $I_p = -1.34$ kA, and $\sigma = 0.3$ in Eq. (3.5). Two natural HAE _{3,4} gaps are marked with solid red circles. Dashed circles indicate possible gaps where magnetic island may develop. The numbers suggest correspondence with the mode labels in figure 3.9. . . .	47
3.11	a) Spectrogram of a Mirnov coil for TJ-II discharge #19189. Coherent modes #1 and #2 with respective poloidal mode numbers -2 and -4 are related with the rational surface $\iota = 3/2$. Modes #3, #4 and #5 are Alfvén waves excited during NBI heating. b) Line-averaged density, toroidal current I_p , and H_α signal.	50
3.12	(a) Mirnov coil spectrogram for TJ-II discharge #21618 during the co+counter NBI phase. (b) H_α signal, line-averaged density, and toroidal current I_p . . .	51
3.13	Continuum spectrum calculated from STELLGAP for #21618 using density profile measured at $t = 1125$ ms. A HAE frequency gap opens at $\rho \approx 0.5$. . .	52
3.14	a) Spectrogram of a bolometry chord tangent to $\rho \approx 0.75$, b) H_α signal, c) line-averaged density and d) toroidal current for TJ-II discharge #30827. . .	54
3.15	a) Alfvén continuum spectrum for two branches (1,1) and (6,9) crossing at $\iota = 10/7$, where MIAE may resides; b) evolution of the density at the fixed location $\rho_{10/7} = \rho(\iota = 10/7)$ that is needed to explain the frequency evolution in figure 3.14a.	55
3.16	Spectrogram of a bolometer chord passing near the plasma edge detecting an Alfvén wave in TJ-II discharge #36790. The over plotted dots, labelled with radial positions, indicate the instants at which successive pins from a 12-pin electric probe stop detecting the mode. A star indicates the time at which a Mirnov coil stops detecting the same mode.	56
3.17	Evolution of GAE and MIAE frequencies with edge ι in an ideal magnetic configuration scans where $\iota(\rho)$, with a profile shape like the standard configuration 100_44_64, is shifted up at constant electron density profile (taken from TJ-II #28174 at $\bar{n}_e = \times 10^{19} \text{ m}^{-3}$). GAE modes are indicated with dashed lines and single mode numbers. MIAEs are indicated with solid colour lines and couples of mode numbers. a) 5/3 Sweeping, b) 3/2 sweeping (see text). The shaded areas are in correspondence with figure 3.18.	58
3.18	Spectrograms of bolometry chords in TJ-II magnetic configuration scans where ι_a increases in time covering the shading area in the respective figures 3.17. a) discharge #27792 sweeping the 5/3 resonance throughout the plasma, b) discharge #33716 sweeping the 3/2 resonance.	59

4.1	a) Scheme of a 16-channel photodiode array (A and D) on top of the Poincaré plot of one of the configurations used. A hypothetical $m = 2$ mode structure, characteristic of standing wave is overplotted (see text). The $\iota = 8/5$ region is indicated. b) toroidal layout of bolometer arrays in equivalent sectors D, A, and B, and stellarator symmetric C.	65
4.2	Mode excitation relying on magnetic configurations. Panels a)d)g) are power spectrograms of a bolometer viewing through $\rho \approx 0.5$; b)e)h) are time evolution of line averaged electron density and diamagnetic energy; c)f)i) the rotational transform profiles of each magnetic configuration in vacuum.	66
4.3	Mode frequency independence on density. a) c) power spectrograms of bolometer viewing at $\rho \approx 0.5$; b) d) line average density and diamagnetic energy time evolutions.	67
4.4	Discharge #30596 with lithium impurities entering the deuterium plasma repetitively during ECR heating. a) Power spectrogram of bolometer viewing in the center of plasma; b) plasma parameters time evolutions: electron temperature measured by ECE at $\rho = 0.53$, line averaged density, bolometer signal with impact parameter $\rho = 0.65$, and plasma current. Vertical lines indicate the moments when the second harmonic starts to drop the frequency.	68
4.5	ECR heated deuterium discharge #30588. a)-b) Time traces of ion temperature, diamagnetic energy, line-density, H_α intensity, hard X-ray flux and central ECE signal; c) radiation signal spectrogram from a bolometer with impact parameter $\rho = 0$; d)e) spectrogram of ECE and Mirnov coil signal respectively.	70
4.6	a) GAM and ISW frequencies at $\rho = 0.5$ estimated from equations (4.1) and (4.2) (lines), and experimental data (dots). b) Observed frequency versus \bar{n}_e and linear fit. c) Radial profiles $f_{\text{GAM}}(\rho)$ and $f_{\text{ISW}}(\rho)$ for discharge #30588 at Thomson scattering time, and spectra of bolometer chords versus impact parameter (see $\delta I/I$ percentage in colour bar). The approximate location of the $\iota = 8/5$ rational surface is indicated. $n = 1$ is used in Eq. (4.2).	72
4.7	Discharge # 40762. a) power of wavelet spectrogram of bolometer chord with $\rho = 0.5$; (b) time evolution of central ECE, HXR and the radiation oscillation due to the mode.	73

4.8	Discharge # 40762. Correlation of bolometer array signals (see diagnostic layout in figure 4.1) with the reference channel 8 ($\rho = 0$), in the frequency range of the acoustic mode shown in figure 4.7a. a) poloidal and b) toroidal correlation (see text). The time interval used is 1180–1185 ms. White line in b) indicates the toroidal propagation by following the maximum correlation. The fitted slope is $d\phi/dt = -145.6$ rad/ms.	74
4.9	Discharge #30598. a) Power spectrogram of bolometer in sector A; b) phase spectrogram of two bolometers viewing at the same poloidal angle but separated $\pi/2$ toroidally.	75
4.10	Discharge #35503. a) Time traces of \bar{n}_e , diamagnetic energy, H_α , hard X-rays and central ECE signal; b-c) cross-power and cross-phase spectrogram between two bolometer chords with the same impact parameter $\rho \approx 0.5$ but different viewing angle; d) cross-power spectrogram of two Mirnov coils.	78
4.11	Discharge #35503. Correlation of bolometer array signals (see diagnostic layout in figure 4.1) with the reference channel 4 ($\rho = 0.4$) for three modes appearing at different discharge conditions: a) before b) after c) back confinement transition.	79

Chapter 1

Introduction

Magnetic confinement fusion (MCF) devices rely on the establishment of toroidally nested magnetic field tubes to confine fusion relevant plasmas, where the main ions must have energies on the order of 10 keV. The first goal is reaching controlled nuclear fusion based on the deuterium-tritium (DT) reaction, which generates 3.5 MeV alpha particles that should be also sufficiently confined to provide plasma re-heating. During the last 60 years, mainly two MCF concepts have been built and studied in many laboratories around the world: tokamak and stellarator. Several reviews about MCF, covering theory, technology and diagnostic issues (see for example [1–3]) are available containing literature at all levels.

Broadly speaking, the confining magnetic flux-surfaces in tokamak devices are formed once the poloidal field produced by an intense toroidal current induced in the plasma is added to an externally imposed toroidal field (see schematic view of tokamak concept in figure 1.1). Consequently, there is a strong feedback between plasma confinement and confining magnetic field, which makes tokamak plasmas a complex physical system: rapidly growing instabilities can destroy the magnetic configuration and provoke a major disruption. Besides, as the inductive current drive has a limit, the tokamak must be a pulsed device unless non-inductive current production methods are applied in a safe way. For these reasons, two difficult requisites for a tokamak-based commercial reactor are steady-state and disruption-free operation. Despite this, the tokamak is a well-developed concept that has many significant advantages as a consequence of its axisymmetric-torus geometry, like acceptably good confinement and manufacturing properties. In the stellarator concept, the confining magnetic flux surfaces are generated by external coils. Since in these devices there is no demand of intense plasma currents, their operation is free from current-induced major disruptions and can be steady-state. However, their lack of axial-symmetry results in much worse confinement of thermal and energetic particles, and the engineering demands are stronger than for tokamaks. Nevertheless a big effort has been done to optimize stellarators in

order to make them approach some kind of geometrical symmetry to improve confinement properties.

Since the boom of stellarator research in the 1980s [4], substantial progress has been made in demonstrating stellarator as a promising option for fusion, where higher plasma parameters and currentless operation have been achieved by applying advanced heating methods. Two main types of devices have been actively studied, depending on the magnetic field generation coils: stellarators with continuous helical coils, called heliotron/torsatron (such as Heliotron E, ATF or CHS), and heliac/helias stellarators that use discrete sets of coils (such as TJ-II, W7-A or W7-AS).

The last two decades witness two big engineering achievements: the large helical device (LHD) operated since 1998, and the Wendelstein 7-X (W7-X) that recently (2015) produced its first plasma. The two devices have different configuration: LHD is a heliotron while W7-X is a helias. But both of them are characterized by their similar dimensions, being the major radii 3.6 m for LHD and 5.5 m for W7-X, and the minor radii more than half a metre. Their magnetic fields, whose strength at axis can reach $\approx 3\text{T}$, are generated by superconducting magnetic coils and have been highly optimized to increase the confinement capability and instability threshold. In LHD, advanced heating methods have significantly pushed the operation regime boundary; electron temperature can be as high as $\approx 10\text{ keV}$ using electron cyclotron resonant (ECR) Heating, and separately ion temperature can also reach $\approx 13\text{ keV}$ using neutral beam injection heating; volume averaged β (plasma pressure/magnetic pressure), which is a measure of economic use of magnetic field, can reach 5%. Wendelstein 7-X aims to demonstrate the potential of a stellarator for a steady state operation reactor. More specific goals are: achievement of adequate confinement of fusion relevant plasma, long-term and stationary operation, attaining high beta plasma, test of island divertor, and control of impurity transport [5].

Plasma parameters and operation space increase if: magnetic field is more optimized, plasma size is enlarged, and heating power is redoubled. However, there are MHD instabilities that limit steady-state, especially in high-confinement plasma operation. They are mostly in the form of low mode number electromagnetic fluctuations, causing thermal or/and fast particle transport. However experimental results suggest that plasma pressure is not the only ingredient; in fact, those collective activities are always related with low order rational in the plasma, and fast particles are partial or fully involved. In present devices, understanding of plasma instabilities and the related thermal/fast particle transport would be very beneficial to extend the operation regimes and propose reliable control tools to prevent catastrophic events.

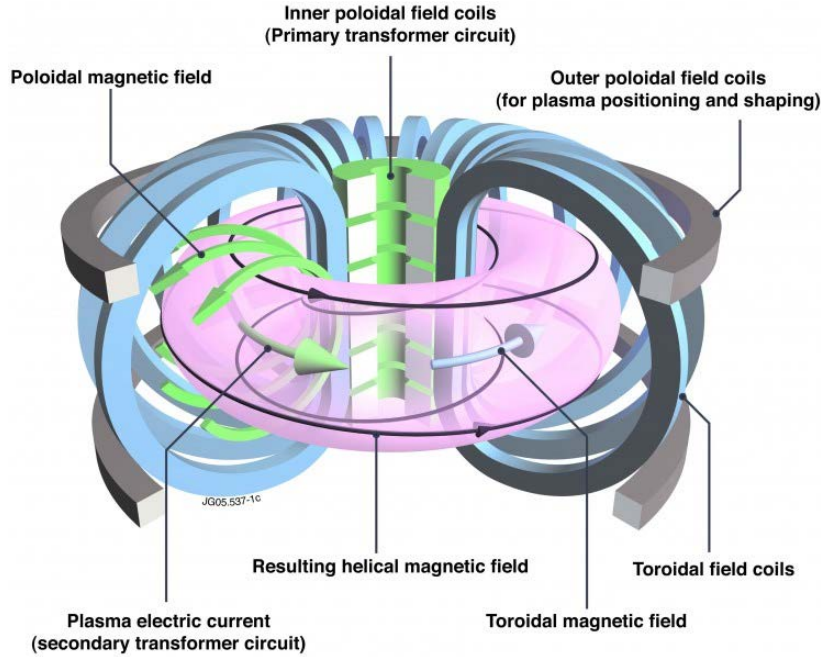


Figure 1.1 Schematic view of tokamak concept. Toroidal field is generated by toroidal field coils, and magnetic field is only formed when plasma current is driven along the toroidal direction. Poloidal field coils are used to control plasma shape and axis position. Picture is from URL www.euro-fusion.org

1.1 Rotational transform and magnetic island

The twist of field line is measured by the rotational transform $\iota \equiv d\psi_p/d\psi_t$, where ψ_p and ψ_t correspond to poloidal and toroidal magnetic flux respectively. A physical understanding of it is the average poloidal twist angle for a period of toroidal transit, where a rational rotational transform $\iota = N/M$ means the field line closes to itself after M toroidal and N poloidal circulations. An arbitrarily small perturbation can destroy the flux surface and form magnetic island. The half width of island can be estimated knowing that $\delta_{mn} \sim \sqrt{4(b_{mn}/m)/(d\iota/dr)}$ [6], where b_{mn} is radial magnetic perturbation with helicity (m, n) , and $d\iota/dr$ measures radial variation of rotation transform. Magnetic shear is a measure of the rate at which initially adjacent field lines on neighbouring flux surface separate with distance advanced along the field lines, and the typical figure of merit is calculated using $s = -(r/\iota)(d\iota/dr)$. In the low magnetic shear or even zero shear region, the island size can be significantly large even for small magnetic perturbations.

The formation of islands that break the flux surfaces and, consequently, the magnetic symmetry of toroidal nesting, is a singular process in toroidal plasmas. In the vicinity of a small island, the electron temperature gradient should be zero due to the high conductivity of

parallel streaming electrons. In MHD (magneto-hydrodynamic) simulations [7], the plasma responds initially by developing localized currents at the rational surfaces that shield out the resonant part of the perturbation there. In the limit of zero resistivity, such currents densities are delta functions. Nevertheless, the localized currents at the rational surface decay rapidly in the presence of even small resistivity, and the islands can grow leading to a resistive instability. The problem is complex and island dynamics in MCF plasmas is an active line of research. When the magnetic field, whose energy density usually dominates by far the plasma pressure, is externally imposed, there is a competition of balance between viscous and electromagnetic torques. The islands can be locked in the laboratory frame or rotate at different speeds. In addition, the plasma flow around rotating islands can become stabilizing and provoke island shrinking. In real plasma operation, where plasma flows, diamagnetic drifts, ambipolar electric fields, and kinetic effects take place, magnetic islands can show very rich dynamics. At the same time, however, their signatures in diagnostic measurements must convey important information about plasma processes.

1.1.1 Island impacts on toroidal fusion devices

In the plasma core, big sized and unstable growing tearing modes (islands) are responsible for degrading plasma transport and limiting achievable plasma parameters [8], which brings about many operation constraints, such as β limit, density limit, edge safety factor limit. The suppression/avoidance of such island is a main issue in all toroidal fusion devices. In conventional tokamak configuration, noninductive current driven by electron cyclotron current drive (ECCD) is applied to suppress pressure driven island instabilities (such as neoclassic tearing mode) [9]. In reverse magnetic shear configuration, NTMs can be stabilized in the negative magnetic shear region. However, double tearing mode reconnection would take place, and may cause off-axis sawteeth transport, which limits minimum q value to be larger than 2.

In stellarator, islands are intrinsic (i.e. islands exist in vacuum) in the configuration but more controllable. Big islands in the core region can be avoidable by carefully designing the rotational transform profile, which is the basic principle of low magnetic shear devices, such as TJ-II and W7-X. Big island effects in the core of high magnetic shear devices can also be diminished. For example, this has been done in LHD by shifting the magnetic axis to move the 1/1 island to the stochastic region. It was experimentally found that the size of the vacuum islands can be strongly modified, depending on the collisionality regime and the plasma β [10]. At sufficiently high β and low collisionality, islands can be even healed by the plasma flow [11] [12].

Islands are not necessarily fatal to confinement if they are thin and stable enough, or if they are located more in the periphery. Numerous experiments in tokamak and stellarator have suggested that islands could be beneficial if they are well controlled. It was concluded that low order rationals were found favorable in the development of internal transport barriers. During edge transport barrier formation in stellarators, the presence of rationals was identified as the triggering mechanism. In the tokamak plasma edge, resonant magnetic perturbations (RMPs) have been applied to control edge instabilities and transport [13] by pumping plasma out. Recently, it was verified that RMPs penetration in the pedestal region is the main mechanism to suppress edge localized modes [14].

1.2 The TJ-II Stellarator

A flexible heliac was proposed in 1980s and built in 1990s to test the MHD properties of this type of configuration [4][15], which is characterized by high transform $\iota \geq 1$ and low negative magnetic shear $|s| \leq 0.2$). The TJ-II [16] shown in figure 1.2 is a 4-period, medium-size helical-axis stellarator, with major radius $R = 1.5$ m, minor radius $a \leq 0.22$ m and magnetic field $B_0 < 1.2$ T. It has a wide range of accessible magnetic configurations, depending on the currents flowing by the external coils. There are four electric currents that can be fed independently on different coil sets: a) I_{cc} , the current of the central circular coil, b) I_{hx} , of the $l = 1$ helical coil wrapped around the circular coil, c) I_{tf} , of the 32 toroidal field coils, which are supplied in series, and d) I_{vf} , the current flowing through the vertical field coils. The ohmic coils (OH), which can generate a loop voltage of 0.1 V, were intended to cancel toroidal currents driven by plasma pressure and heating methods.

There were two experimental campaigns, performed in 1996 [17] and 2000 [18] see figure 1.3, to measure the vacuum magnetic surfaces. About 50 configurations were measured, with the magnetic field scaled to be a 10% of the nominal field for plasma operation, and an excellent overall agreement between measured and calculated surfaces was found. In some occasions, magnetic islands are found when calculations predict values $\iota = N/M$, with integer N and M. For lower order rationals, only $N = 4n$ islands, (natural islands), should appear in the configuration, when the transform $\iota = N/M$, if the fourfold symmetry is incorporated in the calculations (no field errors). Other N islands show up as result of field errors. Natural $N=4, M=3$, islands were observed at predicted coil currents in excellent agreement with calculations, as figure 1.3a demonstrates. If M is larger, broken surfaces with M single spots are obtained, as shown in figure 1.3b for the case $N=8, M=5$. Non-natural islands are clearly visible for the cases $3/2$ (see figure 1.3c), $5/3$ and $7/3$ (not shown here).

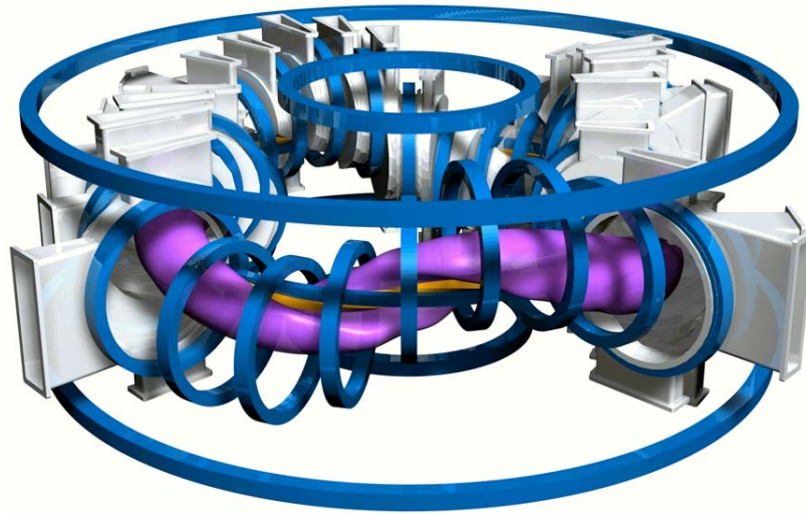


Figure 1.2 Schematic view of TJ-II with toroidal, vertical and central coils in blue, helical coil in orange, and plasma in purple. Picture source: <http://fusionwiki.ciemat.es/wiki/TJ-II>

1.3 Operation of TJ-II stellarator

TJ-II has been operated under several first wall conditions in order to achieve a good density control and reduce the impact of the strong plasma-wall interactions (PWI) on plasma performance. The change from full metallic to boronized walls led to a rise of the electron temperature at the limiter of a factor of 3, and a strong ($\leq 4\times$) increase in the required fuelling rate for the same density respect to the metallic case [19][20]. Since 2008, lithiumisation is periodically applied to the boronised first wall [21]. The change from boron to lithium walls yielded an increment of a factor of two in the energy confinement time τ_E , and 1.6 in maximum electron density [22] at low input power. A recycling coefficient as low as $R \sim 20\%$ was achieved for hydrogen, therefore plasma density is almost fully controlled by external fuelling. After the installation of one liquid lithium limiter (LLL), even better density control and plasma confinement has been achieved and a marked reduction of carbon impurities, especially in plasma configurations with strong interaction with the vessel walls. Further increments of about 1.5 in the energy content, W , and 1.7 in ne have been obtained [23].

In TJ-II there are two gyrotrons that can inject into the plasma microwave beams with a power of ≤ 300 kW each, at a frequency of 53.2 GHz (the second harmonic of the electron cyclotron resonance frequency for 0.95T) [24]. The microwave beams are polarized in the extraordinary mode (X-mode, i. e., wave with electric field elliptically polarized and injected perpendicularly to the magnetic field). The produced plasmas are characterized by rather peaked electron temperature and flat or even hollow electron density profiles (see figure 1.4a).

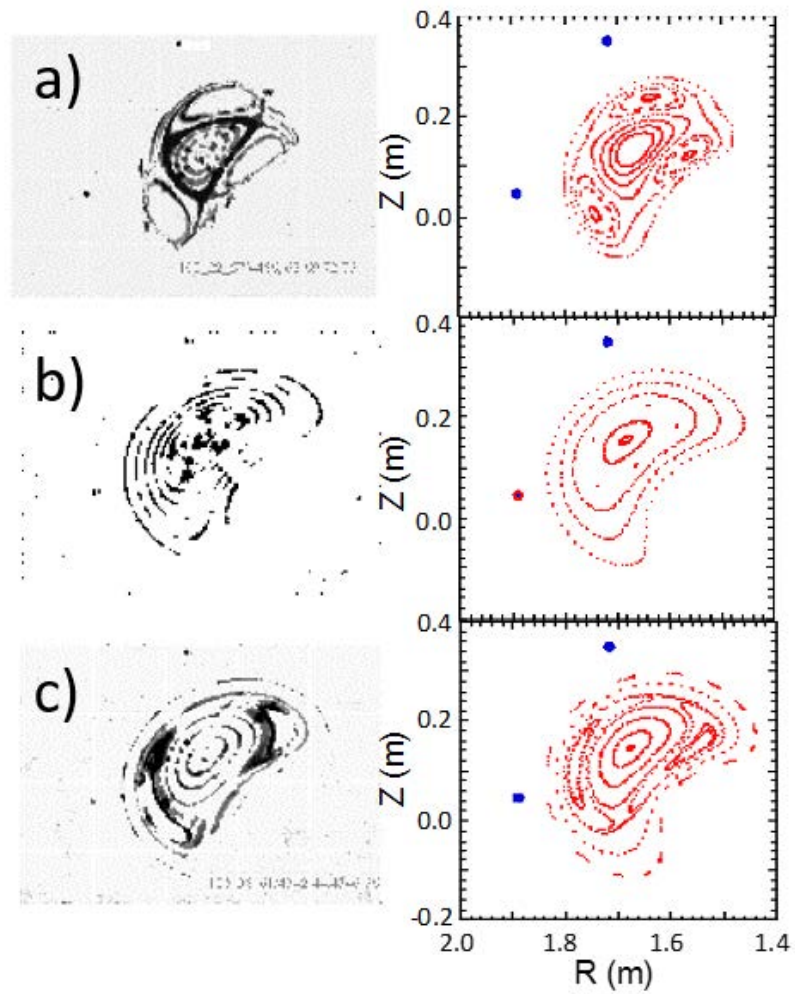


Figure 1.3 Measurement vs. Calculation. a) $N=4, M=3$; b) $N=8, M=5$; c) $N=3, M=2$.

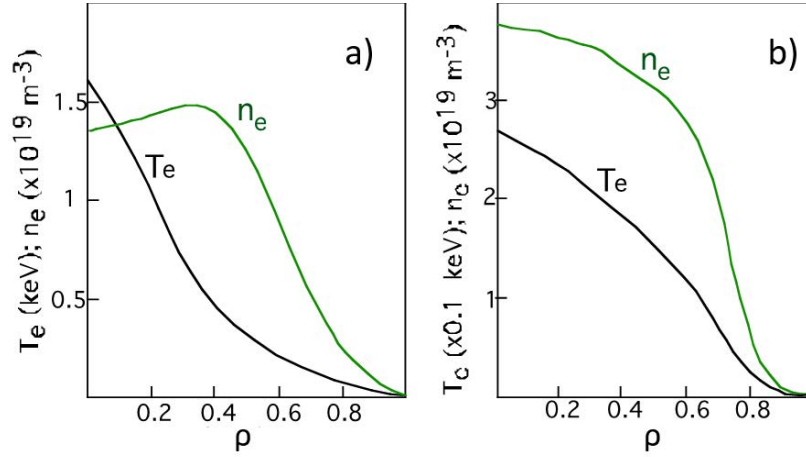


Figure 1.4 Examples of electron temperature and density profiles during ECR a) and NBI b) heating.

The maximum central value achieved for electron temperature is $Te_0 \approx 1.5 \text{ keV}$ and electron density is limited by the cut-off value for 53.2 GHz, $ne(r) \leq 1.7 \times 10^{19} \text{ m}^{-3}$. However, it is well known that in low-density stellarator plasmas heated with ECRH, the electron energy distribution function is strongly deformed (see, e.g., [25]). Depending on input power density, the characteristic energies of the generated suprathermal electron populations can be rather high. In particular in TJ-II, fast electron tails of $\sim 70 \text{ keV}$ were commonly detected [26][27].

The neutral beam injection (NBI) system of TJ-II has two tangential injectors of highly energetic neutral hydrogen beams, delivering $P_{in} \leq 700 \text{ kW}$ port through each along parallel directions to the magnetic field (co and counter) [28]. The typical beam energy mix is 55% of full energy ($E = 34 \text{ keV}$), 25% of $E/2$ and 20% of $E/3$ (corresponding to the three beam energy components that originate as molecular species in the ion source) [29]. The electron density profiles of the produced plasmas range from markedly peaked (bell-like, typical of low confinement mode) to rather broad (dome-like), like the electron and ion temperature profiles. The produced plasmas can reach central electron densities up to $9 \times 10^{19} \text{ m}^{-3}$ and electron temperatures around 0.35 keV. The combination of ECRH pulses of 350 ms duration and 120 ms of NBI heating, together with the configuration flexibility, yields a rather wide operation space for TJ-II (input power density 0.33 - 1.55 MW/m^{-3} ; average electron density 0.2 - $8.0 \times 10^{19} \text{ m}^{-3}$; effective minor radius 11 - 20 cm; edge rotation transform 1.3 - 2.3, and plasma volume 0.5 - 1.2 m^{-3}).

During plasma heating, plasma current is driven unavoidably, such as bootstrap current [30] due to plasma pressure, current induced by ECR heating, current due to NBI momentum injection, etc. The Ohmic current can be induced on purpose to compensate the plasma current, but sometimes it is deliberately driven to change the rotational transform profile. In

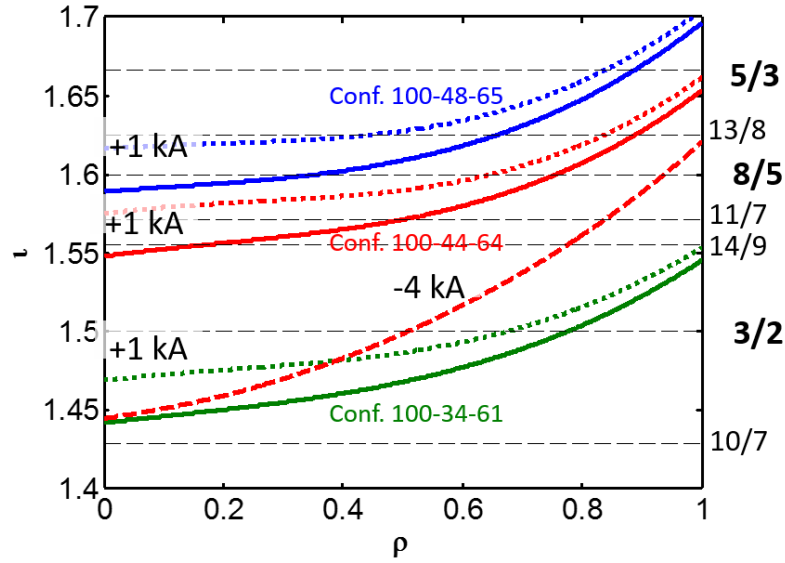


Figure 1.5 Solid lines: rotational transform profiles used in TJ-II discharges; dotted lines: t profiles modified by 1 kA current of a given shape; dashed curved line: t profile modified by assuming -4 kA current; dashed horizontal lines indicate the lowest rational numbers.

figure 1.5, we have represented the rotational transform profiles of three magnetic configurations that, in vacuum, have low-order rationals in the region $0.6 \leq \rho \leq 0.9$. It can be seen as well, how profiles are modified when net plasma current is non zero. Dotted lines have been calculated for a positive current of 1kA, a typical value for co-NBI heated plasmas. In this case, rotational transform profiles are shifted up, rational positions are moved inward, and the magnetic shear is significantly reduced in the core region $\rho \leq 0.6$. For an ohmic current of -4 kA, typical for NBI-started operation, core t profiles can be significantly changed, more low order rational values are crossed and, magnetic shear is largely increased.

1.3.1 Selective diagnostic layout

For the present work, active and passive diagnostics data have been taken into account, but the main analyses have been done using the information from Mirnov coils and bolometers. Occasionally Langmuir probe arrays and x-ray detectors have been determinant and the necessary profiles from Thomson scattering have been used when available. In figure 1.6a the toroidal location of several diagnostics of interest is indicated, together with the position of the heating systems. In normal operation, the toroidal field direction is counter clockwise (ccw). The bolometry system consist of 3 arrays of 20-channel silicon photodiodes (AXUV-20EL, Absolute eXtreme UltraViolet, from IRD) for tomography purposes located in top and lateral ports of sectors B7 ($\phi = 255.5^\circ$) (see figure 1.6b), and three 16-channel (AXUV-16EL)

arrays located in two identical top ports of sectors D7 ($\phi = 75.5^\circ$) and A7 ($\phi = 155.5^\circ$) and in the ‘stellarator symmetric’ bottom port of sector C2 ($\phi = 284.5^\circ$), to monitor up-down and toroidal asymmetries in global plasma radiation [31] (see poloidal view lines scheme in figure 5.1). In figure 1.6c, the scheme of the 25 poloidal Mirnov coils array located at $\phi = 45^\circ$ can be seen [32]. Other two linear (vertical) arrays monitor magnetic fluctuations in the equivalent cross sections of sectors B5 ($\phi = 232^\circ$) and C4 ($\phi = 308^\circ$), but their coil positions are non-equivalent, therefore they cannot be used for toroidal mode number determination. The digitising frequencies are: poloidal array D - 625 kHz; linear array B - 625 kHz, and linear array C - 1 MHz (two coils) and 100 kHz.

In the early campaigns of metal and Boron-coated walls, a rather complete x-ray detection system was in operation [33]. Different photon energy windows were probed (80-2000 keV, ‘Hard X Ray’; 20-200 keV, ‘intermediate X Ray’; 2-15 keV, ‘soft X Ray’) to determine the electron energy distribution function and then characterize supra/epi thermal populations, for discharges equivalent to the used in this work. In recent campaigns, no Pulse Height Analyses can be performed while the limiters are operated. Only flux measurements are fully available.

1.4 Overview of the work: Collective plasma oscillations and rational surfaces in TJ-II

Aside from the abovementioned differences between tokamaks and stellarators plasmas, MHD instabilities of similar basic nature are ubiquitous in the experiments and originate in the regions where i is a low order rational number, the commonly called “rational surfaces”. However, and although such regions are unavoidable in MCF devices, many properties of the rational surfaces remain unclear. Very often, MHD instabilities grow out of an existing mode that manifests as a plasma oscillation before entering a non-linear phase or may remain as small perturbations. In the particular case of the TJ-II stellarator here studied, low-to-intermediate frequency MHD modes are also present in practically all discharges but only in a few cases some explanation has been suggested for distinctive discharges (see, for example, [34–36, 32, 37–39]).

As MHD activity in the TJ-II is generally coupled to transport in some way, either through transport-barrier phenomenology or through interaction with high-energy particles, a broad classification of all this low-to-intermediate frequency MHD activity is necessary to deepen in related transport studies. It is the purpose of this thesis to offer a classification (and point to the implications) with a new perspective, which should be rather general due to the generality

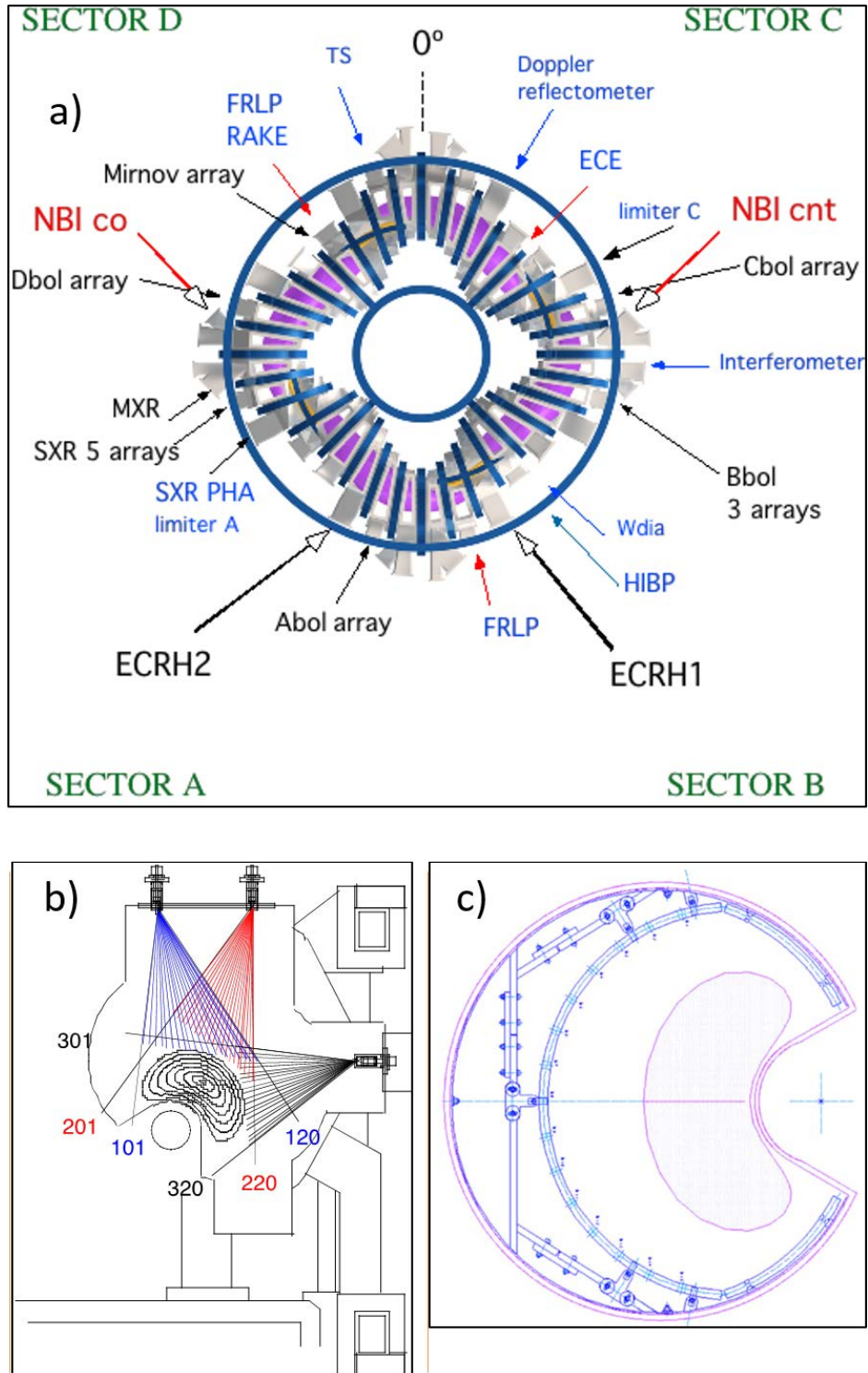


Figure 1.6 a) Top view of TJ-II showing the position of several diagnostics and its heating systems; b) bolometer arrays in sector B7; c) poloidal array of Mirnov coils sited between sector D4 and D5 ($\phi = 45^\circ$).

of these phenomena. Indeed, we can advance that all MHD activity of low-to-intermediate frequency here studied has ended up belonging to one of three very broad categories of general interest for the MCF community, and in all cases new findings, most likely not specific of the TJ-II stellarator, have emerged.

The confinement properties of co-injected NBI plasmas have been related with the rotation state of the magnetic islands. This will be deeply described in Chapter 2. In Chapter 3, we propose a new type of low-frequency helical Alfvén wave based on the assumption that magnetic islands induce new frequency gaps in the continuum spectrum. Chapter 4 describes for the first time one type of acoustic mode appearing in ECRH plasmas, which shows a mixed nature between that of energetic-electron induced Geodesic Acoustic Modes (eGAM) and Ion Sound Waves. A general discussion of the "application" of rational surfaces to regulate plasma transport through their interaction with thermal plasma, fast particle populations, and plasma waves is contained in Chapter 5.

Chapter 2

Magnetic island dynamics in NBI plasma

The plasma response to vacuum magnetic islands originated at low order rational values is studied during co-NBI heating. Thin magnetic islands are normally unlocked and rotate with the ExB flow, provoking quasi-coherent magnetic fluctuations that are intense during L-mode but significantly dim in H-mode, when both flow and flow shear increase. Local transport barriers are formed in the vicinity of the resonant locations, but at some threshold, the barrier can break down, triggering bursts of particles and heat across the plasma and leaving time traces in the diagnostics that resemble ELMs in the tokamak edge. The break-up of barrier coincides with island developing into an unstable bursting state. The frequency of the bursting mode is compatible with a drift of the islands at the electron diamagnetic speed in the plasma frame, but the frequency shifts down rapidly in a kind of relaxation process that ends in the re-establishment of the barrier. Therefore, the process, which happens on a millisecond timescale, starts again giving a cyclic behaviour and a dynamic state whose confinement quality depends on the repetition rates. The plasma can be trapped in this dynamic state unless forced externally to abandon it via heating, fueling or configuration change.

2.1 Introduction

Magnetic fusion devices have shown MHD activity that can be often associated with the existence of coherent modes. In turn, most of this dynamics happens in relation with distinguishable confinement states somehow associated with the formation of transport barriers of different qualities, like the “enhanced D_α H-mode” in the Alcator C-Mod device [40–42], where quasi-coherent (50-150 kHz) and higher frequency (200-300 kHz) weakly coherent electromagnetic modes are observed during the so called I-mode of confinement. In the quiescent double barrier regime of the DIII-D tokamak, ELMs are replaced by the

edge harmonic oscillation (EHO) in a state of larger edge particle transport. The modes are rather coherent, have low toroidal mode number and propagate near the electron diamagnetic frequency [43]. More recently, a bursty, chirping mode within the range 40–110 kHz has been associated to the enhanced H-mode pedestals obtained with Li-injection in the same device. The modes propagate in the electron diamagnetic drift direction, faster than the ExB drift [44]. Another electromagnetic quasi-coherent mode propagating in the electron diamagnetic drift direction is identified in JET related with ELMy activity [45]. All examples from this non-exhaustive list put MHD at the core of different confinement modes. Additionally, the plasma response to RMPs is a major concern in present-day tokamaks and the behaviour of rational surfaces is evidently important in this technology [46].

In stellarator/heliotron devices, where the current densities ($\sim 10^{-2}$ MA/m²) are much smaller than in tokamaks (~ 1 MA/m²), large scale classic tearing modes are not a big concern. However, error fields from magnetic coils may produce vacuum islands that, much like RMPs, will provoke a plasma response. These devices allow for external control of the τ -profiles, but still the rational surfaces have been related with transport events and the establishment of different confinement modes. The transition to H-mode in the CHS heliotron/torsatron was achieved after modification of the τ -profile by inducing a small ohmic heating current, often being initiated by a sawtooth crash caused by a coherent mode with the poloidal $m = 2$ and toroidal $n = 1$ mode numbers [47]. In the LHD, an improved confinement regime that shares H-mode features can be achieved when the resonant $\tau = n/m = 1$ is placed in the middle of the –vacuum– edge ergodic layer [48]. ELM-like bursts –conveying particle propagation– and edge coherent modes occur at or near the resonant position due to the formation of an edge transport barrier in the magnetic hill region [49]. MHD activity related with $\tau = 1/1$ and $3/2$ in the periphery are excited during high beta ($3/2$ also observed in low- β regimes), with identified modes rotating in the electron drift direction below 10 kHz. Island rotation is presented as a possible explanation for this mode [50]. In the low magnetic shear stellarator W7-AS, ELMs have been observed close to the H-mode condition. In well separated ELMy events around the H-mode barrier, a 200–500 kHz quasi-coherent mode lasting about 50 μ s preceded a particle and heat transport burst followed by 10-50 kHz relaxation oscillations. Resistive interchange or ballooning modes were proposed as most likely instabilities in relation with ELM phenomena in the W7-AS, in turn related with low order rational values of τ .

The experience concerning MHD activity and transport quality in the TJ-II is quite ample as well. ELMy and general MHD activity in relation with improved confinement are known from the initial experiments [51]. The flexibility in magnetic configuration of the TJ-II has permitted the study of detailed effects on confinement of well separated magnetic

resonances in the plasma column (see a summary and references in [52]). These works have confirmed that rational surfaces are at the origin of macroscopic transport events such as particle bursts, internal crashes and transport barriers [53]; and causality experiments have proven that a proper placement of magnetic resonances inside the plasma favours the formation of transport barriers [54]. The latter do not necessarily form right at the plasma edge, which is probably the reason why the quality of H-mode in the TJ-II depends sensitively on magnetic configuration [55]. Dynamical pre-transition states with pronounced oscillations in the plasma rotation resembling limit cycles require the presence of low order magnetic resonances inside the plasma [56].

Starting from all this knowledge, now we relate the dynamical state of islands with the formation of stable or unstable transport barriers. To this end, we start the chapter (Section 2.2) with an overall view of the phenomena to be described later. Such phenomena can be associated to two island rotation states, one approximately coincident with the electric drift rotation of the plasma (Section 2.3) and another one, generally unstable, with a faster rotation that we associate to the electron diamagnetic drift in the ExB frame (Section 2.4). We finish the chapter with a discussion (Section 2.5) and brief conclusions.

2.2 Overview of island dynamics phenomena

Most of the phenomena to be described happen in NBI plasmas, but not exclusively. When the wall conditioning allows for a sustained NBI plasma, it is common that confinement transitions are produced with the creation of transport barriers near the plasma edge [57]. The process of barrier formation is, in many cases, unstable in the sense that such barriers break and re-establish in a cyclic manner, resembling ELMy activity with typical ~ 1 ms repetition rates [53], smaller than global ~ 10 ms confinement times. In these discharges, low frequency ($f \leq 100$ kHz) coherent or quasi-coherent modes are commonly detected by many diagnostics, e.g. Mirnov coils, bolometers, Langmuir probes, electron cyclotron emission (ECE), reflectometers and heavy-ion beam probes (HIBP), which reveals the electromagnetic nature of the modes and their impact in many plasma parameters. The onset of the modes is irrespective of heating method, but rather depends on plasma confinement regime. Poloidal mode number analyses indicate the relation between these modes and magnetic resonances forming island structures in the region $0.5 \lesssim \rho \lesssim 0.9$.

Many of these aspects can be appreciated in figure 2.1, where almost twin discharges with the same magnetic configuration, plasma wall condition and plasma heating method (co-NBI) are compared. Aside from being illustrative, we have chosen these discharges because the readers can obtain much more detail about the same or similar discharges in [58, 36, 59]. The

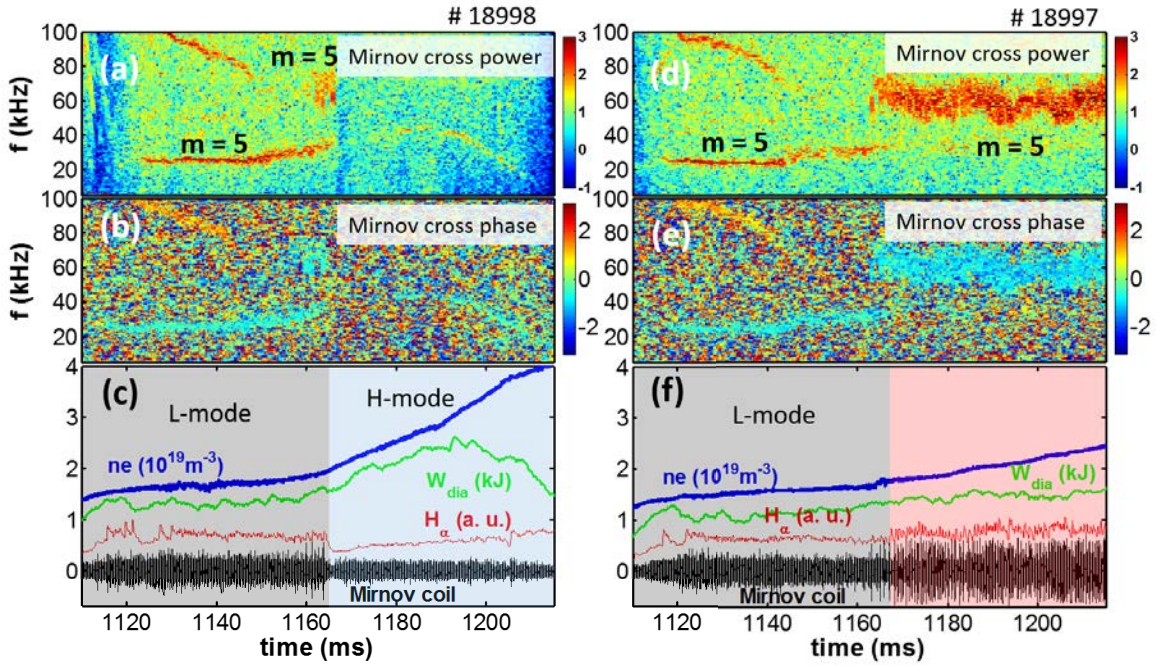


Figure 2.1 TJ-II discharges #18998 (a-c) and #18997 (d-f). (a)&(d) Cross-power and (b)&(e) cross-phase spectrograms of Mirnov coil signals; (c)&(f) line average density \bar{n}_e , diamagnetic energy W_{dia} , H_α signal, and magnetic fluctuations ($5 \text{ kHz} \leq f \leq 100 \text{ kHz}$). Grey shading indicates plasma in L-mode, blue for H-mode, pink for an intermediate state characterized by bursting modes (see also figure 2.2.)

one with larger \bar{n}_e in L-mode, #18998, enters the H-mode (blue-shaded region) at $t \approx 1165$ ms, which manifests in the significant drop of H_α emission and magnetic signal amplitude, and the more rapid increment of diamagnetic energy W_{dia} and line-averaged electron density \bar{n}_e . In contrast, discharge #18997 with slightly lower density during L-mode but quite similar H_α and Mirnov signals, enters a new phase different from H-mode (pink shading in figure 2.1(f)). After some threshold, the plasma shows enhanced average H_α level accompanied by bursty magnetic activity; the density ramps up at a slower pace and the diamagnetic energy just slightly increases and then saturates. It will be noted, however, that discharge #18998 in figures 2.1(a) and (d) also displays this unsteady phase during a very short time just prior to the transition ($t \approx 1160$ ms), which is suggestive of an intermediate state.

The spectrograms of Mirnov-coil data in figures 2.1(a,b) and (d,e) reveal two distinct states of $m = 5$ magnetic fluctuations: one is more coherent and steady (#18998), the other is bursty (#18997) covering larger frequencies (50–80 kHz). Both modes are related in this case with the $\iota = 8/5$ rational surface located in $\rho \approx 0.7$ (see figure 1.5). In figure 2.1(a), the coherent or quasi-coherent mode within the range 20 to 40 kHz shows up in L-mode and its frequency rises as the density does. Before reaching the L-H transition moment, see figure

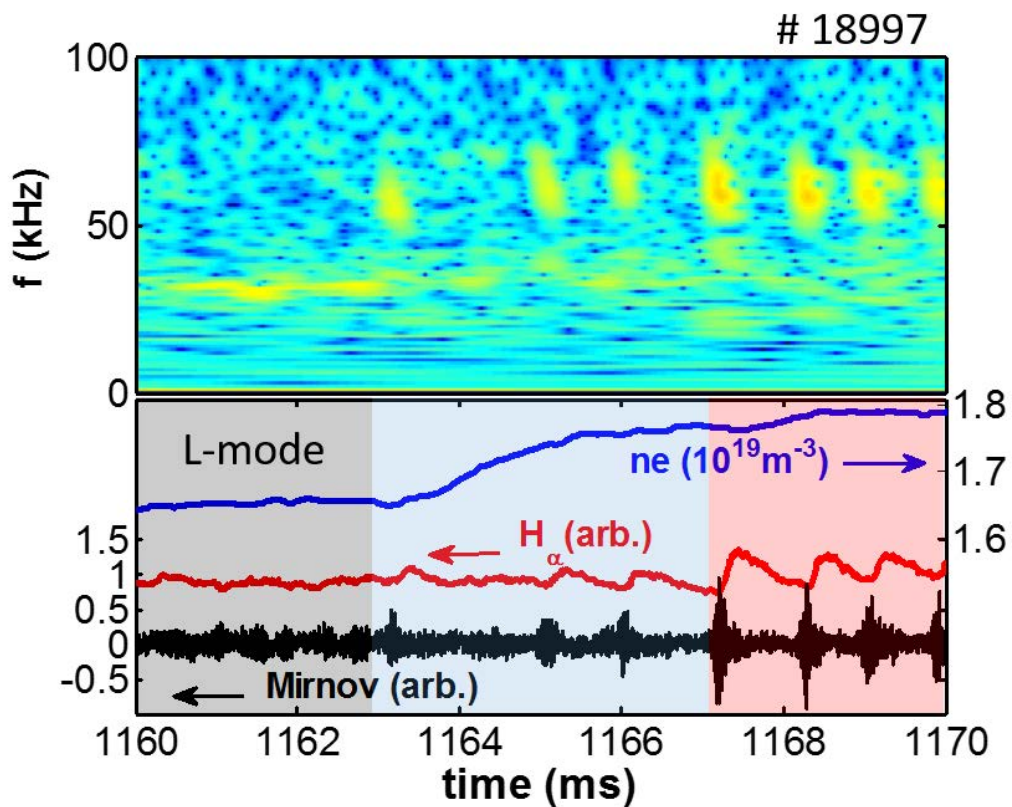


Figure 2.2 Detail of figure 2.1 for discharge #18997 around the establishment of the bursting mode, where its chirping nature can be appreciated in correlation with H_α pulses.

2.1(c), the steady mode loses coherency and momentarily shows the bursting mode with the same phase relation. The latter lasts only a few ms and is completely suppressed after the L-H transition, when the steady mode is recovered with smaller amplitude and variable frequency roughly following the diamagnetic energy. In figure 2.1(d), the steady rotation mode behaves similarly to that in figure 2.1(a) and also jumps to the bursting mode. The difference now is that, at the transition moment, the bursty mode becomes more active with faster cycles remaining so until the end of discharge. Its behaviour is better appreciated in figure 2.2, which is a zoom of figure 2.1(f) focusing on the transition from the steady to the bursty mode. Here we see its characteristic chirping-down nature and its relation with confinement: depending on the amplitude of magnetic bursts and the time interval between them, the H_α bursts also change amplitude and the average density follows accordingly. Next we provide more detail about these phenomena.

2.3 Steady rotation mode: Islands in plasma frame

Well pronounced, low frequency (a few tens of kHz) steady rotation modes, are normally seen during the NBI heating phase in typical L-mode confinement conditions, i.e., with profiles that are peaked in the center but quite flat near the edge [21]. Here we discuss their relation with magnetic island rotation and the evolution of local magnitudes.

2.3.1 Frequency scaling

Steady low-frequency modes with well defined m , as in figure 2.1, have been identified in different magnetic configurations using phase-analysis of signals from a poloidal array of magnetic coils [32]. In figure 2.3 we plot the measured frequencies as a function of poloidal mode number for several discharges. In each discharge, blue crosses and red circles represent respectively lower and upper frequencies due to variations in rational surface position and plasma profiles. The corresponding linear fits are shown separately. The shaded region covers the expected mode frequencies if they were due to the rotation of islands with the indicated m and locked in the frame moving with $E \times B$ velocity, often called “plasma frame”; i.e., in the shaded region $f = m \times u_E / 2\pi a \rho$ where u_E , or magnitude of the $\mathbf{E} \times \mathbf{B} / B^2$ velocity, is taken in the range 3–6 km/s as found in NBI heated plasma with line average densities near $2 \times 10^{19} \text{ m}^{-3}$ [55]. Additionally, the phase analysis shows that the magnetic perturbations propagate in the electron diamagnetic direction, as expected from the all-negative radial electric fields characteristic of these plasmas [60, 61]. Based upon figure 2.3 we interpret these low-frequency modes as islands rotating with the $E \times B$ plasma

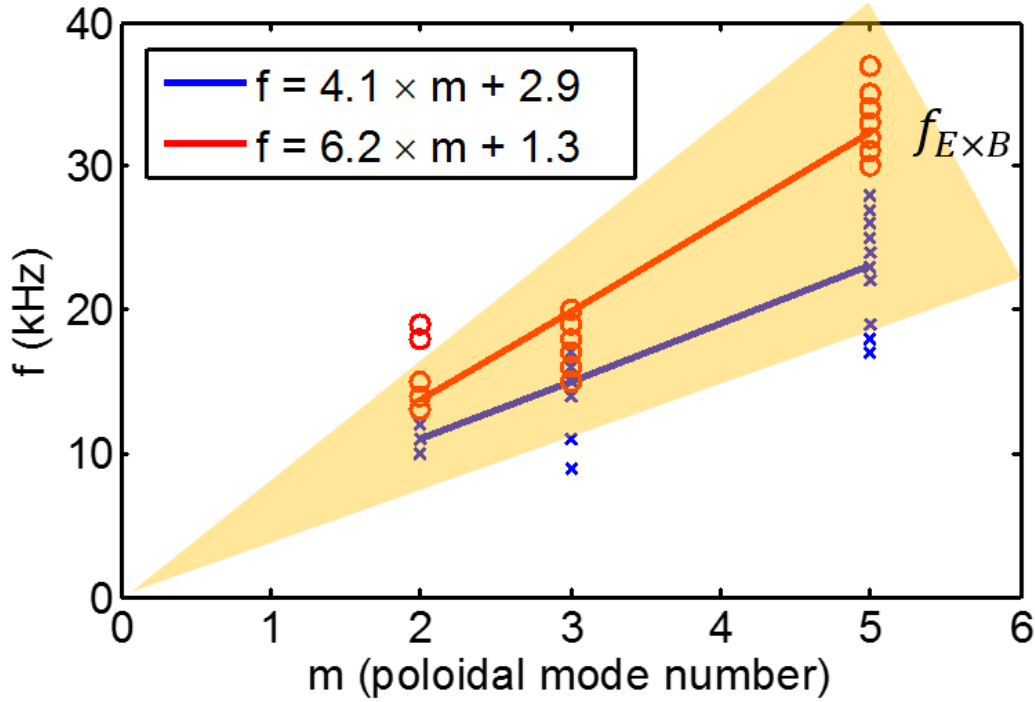


Figure 2.3 Frequency scaling with poloidal mode number in L-mode plasma during NBI heating. The shaded area covers values expected from ExB rotation.

flow. This is in agreement with previous TJ-II works where, based also on the proportionality between mode number and frequency of detected magnetic fluctuations, island rotation in ECRH [62] plasmas has been identified.

2.3.2 Local electron temperature evolution

Figure 2.4 shows data from discharge #37734, started and sustained only with co-NBI heating up to $t \approx 1020$ ms, when the density is kept around $\bar{n}_e = 0.7 \times 10^{19} \text{ m}^{-3}$. The vacuum magnetic configuration has $\iota(0) = 1.55$, but there is an initially strong negative current ($I_p \approx -4.0$ kA) induced as a consequence of the start-up method [63]. In these conditions, the $\iota = 3/2$ rational can reach mid-radius but still be detectable with Mirnov coils. Figure 2.4(a) shows the corresponding spectrogram from Mirnov-coil data, where three harmonics of quite narrow frequency width are detected, especially during $1010 < t < 1020$ ms. Then the frequencies increase slightly and lose coherence until $t \approx 1025$ ms when the modes are considerably weakened. The local electron temperature fluctuations are represented by two ECE signals whose cross-power spectrogram is shown in figure 2.4(b). The first harmonic of the cross spectrum is neatly detected and its change in coherence

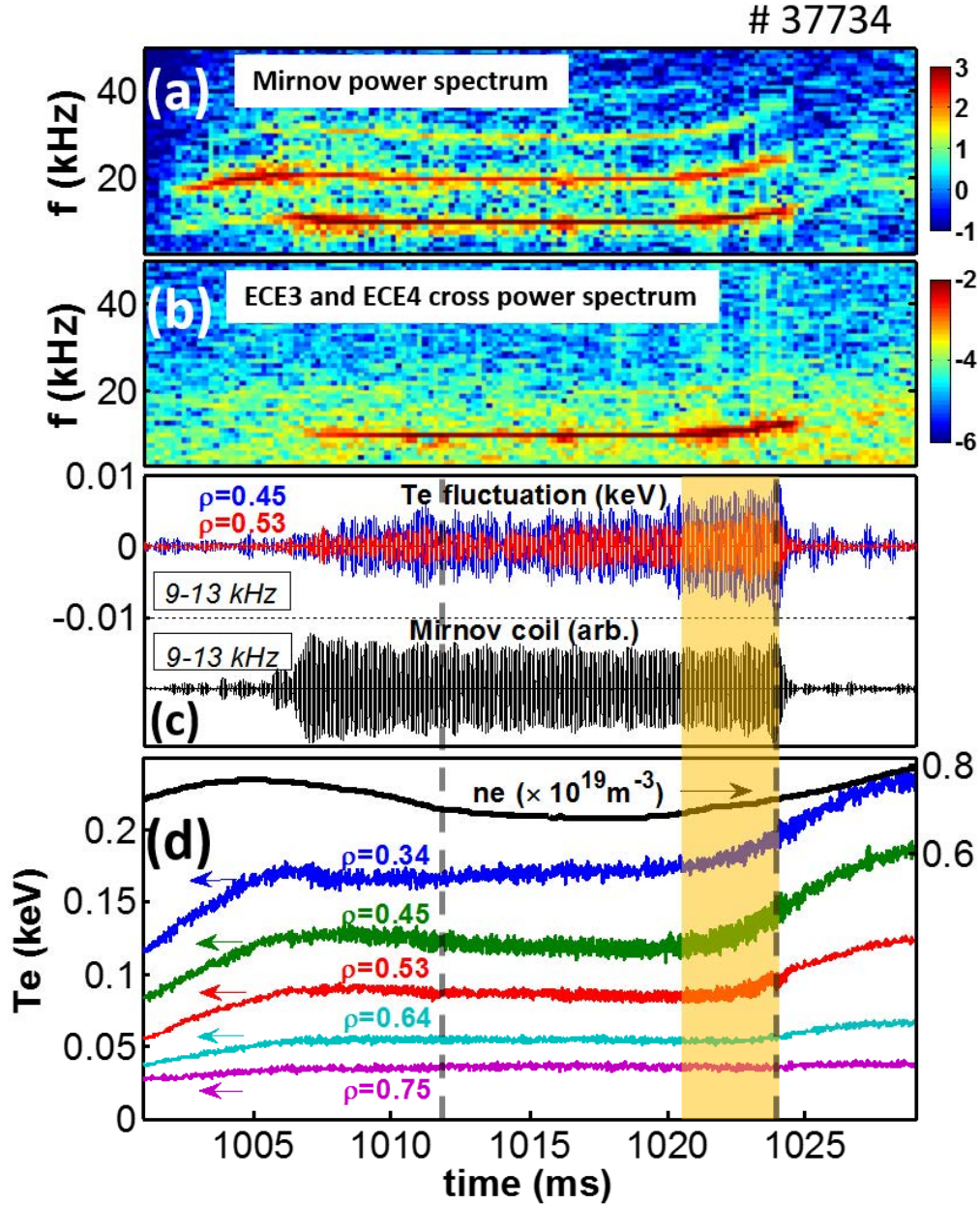


Figure 2.4 NBI heated discharge # 37734 during a low density phase ($\bar{n}_e \approx 0.7 \times 10^{19} \text{ m}^{-3}$) and net plasma current $I_p \sim -4 \text{ kA}$. (a) Power spectrogram of magnetic fluctuations; (b) cross power spectrogram of two ECE channel signal, ECE3 ($\rho = 0.53$) and ECE4 ($\rho = 0.45$); (c) Fluctuations of these same ECE traces and magnetic fluctuations in the frequency band 9–13 kHz; and (d) line density and electron temperature at the indicated radii.

coincides with the one in figure 2.4(a), while the second harmonic is barely detected and the third one is absent.

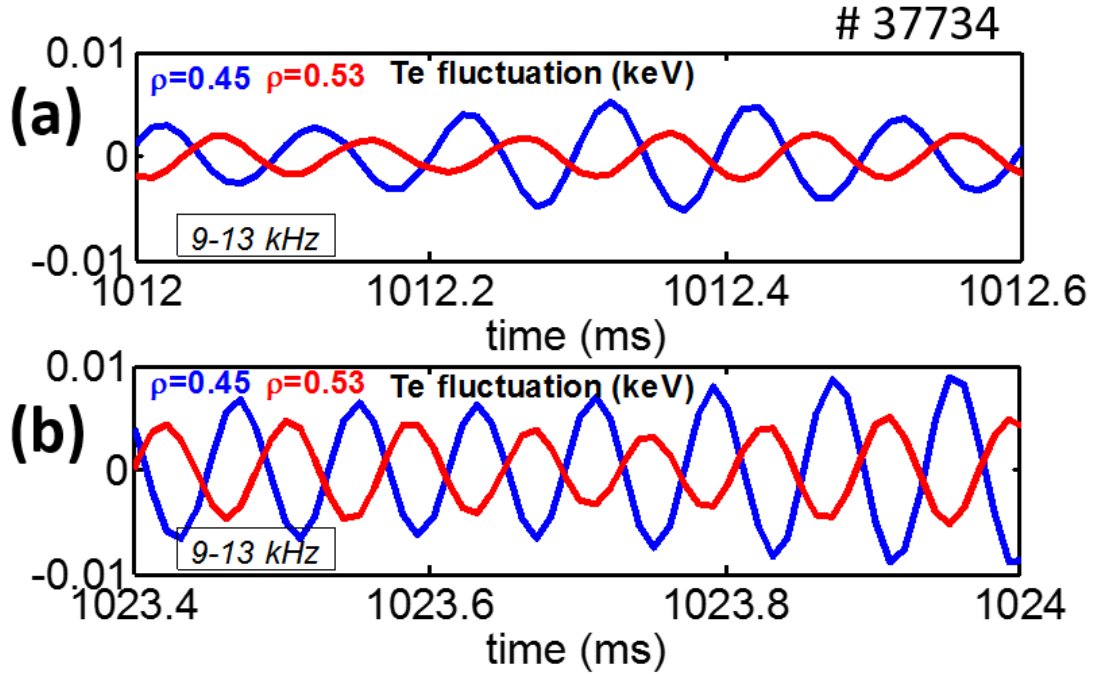


Figure 2.5 Zoom in of temperature fluctuations at $\rho = 0.53$ and $\rho = 0.45$ in figure 2.4c around $t = 1012$ ms (a) and $t = 1023$ ms (b).

The time traces of the two ECE channels and Mirnov coil signal shown in figure 2.4(c) have been band-pass filtered within 9–13 kHz to highlight the first harmonic in figure 2.4(a). The evolution of the average density and the temperatures at different radii are shown in figure 2.4(d), where the average T_e -gradient is seen to increase between $\rho = 0.45$ and $\rho = 0.53$. The corresponding channels ECE3 and ECE4 have been selected because they bound the region where the $m = 2$ magnetic resonance is expected. A detail of figure 2.4(c) is given in figure 2.5, where time windows around $t = 1012$ ms and $t = 1023$ ms are chosen to represent the moments of having constant and increasing frequency, respectively. Here we note the phase inversion of T_e fluctuations in the fundamental harmonic between the two ECE channels, which tells us again that a rotating island structure is involved in provoking the steady coherent mode. The harmonic fluctuations in T_e can be associated to the periodic modification of flux surfaces caused by the proximity of the $\iota = 3/2$ magnetic island.

2.4 Bursting-chirping mode: Drifting islands in plasma frame

When the bursting chirping mode sets in, like in figures 2.1(d) and 2.2, the island rotation speed seems to change abruptly to higher values. We also observe that the establishment of a H-mode does not provoke a jump in frequency, see figures 2.1(a) and (b), although the frequency does evolve during the H-mode phase. This makes it very unlikely that the jump in frequency that corresponds to the bursting chirping mode be the consequence of a local change in radial electric field.

Low frequency island rotation modes that jump to higher chirping frequencies can be found both in ECRH and NBI plasmas, very often preceding H-mode for the latter or just after the H-mode is abandoned (see more examples in [36]). Here we investigate these modes in more detail given their relation with the threshold between confinement modes.

2.4.1 Frequency scaling in chirping mode

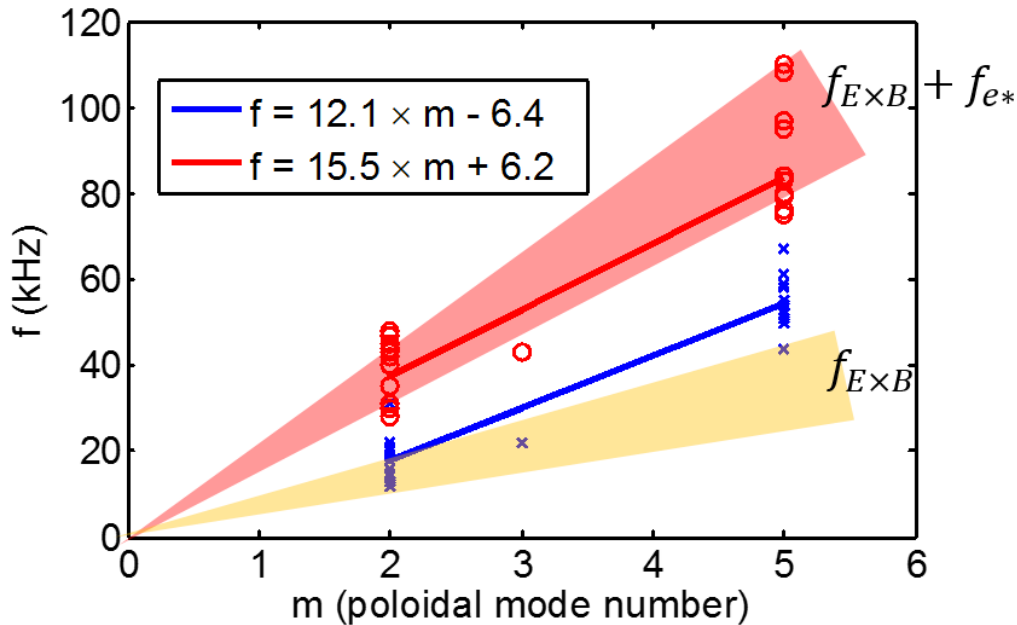


Figure 2.6 Frequency scaling with poloidal mode number of the bursting chirping mode in NBI plasmas. Two fits are shown for the highest (red circles) and lowest (blue crosses) frequencies covered by the chirping. Coloured triangles indicate the frequency ranges expected for rotation with the u_E or $u_E + u_{*e}$ velocities.

Three magnetic resonances have been identified as able to provoke bursty chirping-modes: $3/2$, $5/3$ and $8/5$, which are lowest order rationals in typical TJ-II magnetic configurations.

They are expected to lead to finite sized magnetic island structures during the plasma discharge, as already noted for the slow rotation mode (Sec. 2.3), and must be likewise associated with the rotation of the same magnetic islands. This has been checked in many cases by the constancy of phase between signals from Mirnov coils poloidally distributed, in passing from the steady rotation mode to the bursting chirping mode.

In figure 2.6, the bursty-mode frequency is plotted against poloidal mode number. Since the modes frequency is chirping down or quite changeable, we split again the data in upper (circles) and lower (crosses) frequencies and perform separate linear fits. The two shaded regions cover frequencies calculated as $f = m \times u / 2\pi a \rho$ assuming that an $\iota = n/m$ island rotates due to some drift velocity u at position $\rho = 0.7$. In the lower shaded region, we assume island movement within u_E velocity range, which is estimated between 5 to 8 km/s. The upper shaded region assumes u_E plus electron diamagnetic frequency taking a fixed $u_E = 7$ km/s and the electron diamagnetic velocity u_{*e} in the range 7–11 km/s, which corresponds to $0.7 < \rho < 0.9$ in these plasmas depending on local density gradient length. The interest of doing so is to show that, recalling the plasma frame as that locally moving with the electric drift u_E , upper frequencies match the electron drift frequency while the lower ones still have some speed (i.e., they lie above the frequencies expected from $E \times B$ drift in the laboratory frame). The chirping-down frequency indicates that, in the plasma frame, the islands start drifting with practically the diamagnetic speed but tend to stop as the plasma evolves during the short duration of each chirp.

2.4.2 Relation between bursts and transport barrier breaking

The identification of the bursting chirping mode as a threshold state for the establishment of a robust transport barrier (e.g., H-mode) calls for an investigation of the chirping process in relation with transport barrier phenomenology. TJ-II discharges in which H-mode phases are interleaved with L-mode phases are rather common in co-injection NBI plasmas like those here studied, see e.g. [59]. Here we choose a magnetic configuration with $\iota = 8/5$ near the edge because, aside from being quite common during TJ-II operation, this condition gives easy access to the H-mode.

Figure 2.7 shows Mirnov-coil spectrograms and time traces of a low density plasma heated and fuelled with co-NBI, where the dominant magnetic resonance $\iota = 8/5$ is initially (vacuum) at $\rho = 0.76$. With moderate $I_p \approx 1.2$ kA, the 8/5 resonance shifts to $\rho \approx 0.5$. In the lower density phase, $\bar{n}_e \approx 0.8 \times 10^{19} \text{ m}^{-3}$, the bursting chirping mode shows up in the frequency range 40 kHz to 70 kHz. At times $t = 1088, 1100$ and 1109 ms (indicated by three vertical stripes), we can distinguish short quiescent periods lasting one or two milliseconds, when magnetic fluctuations are strongly reduced and the H_α level drops, as in short-lived

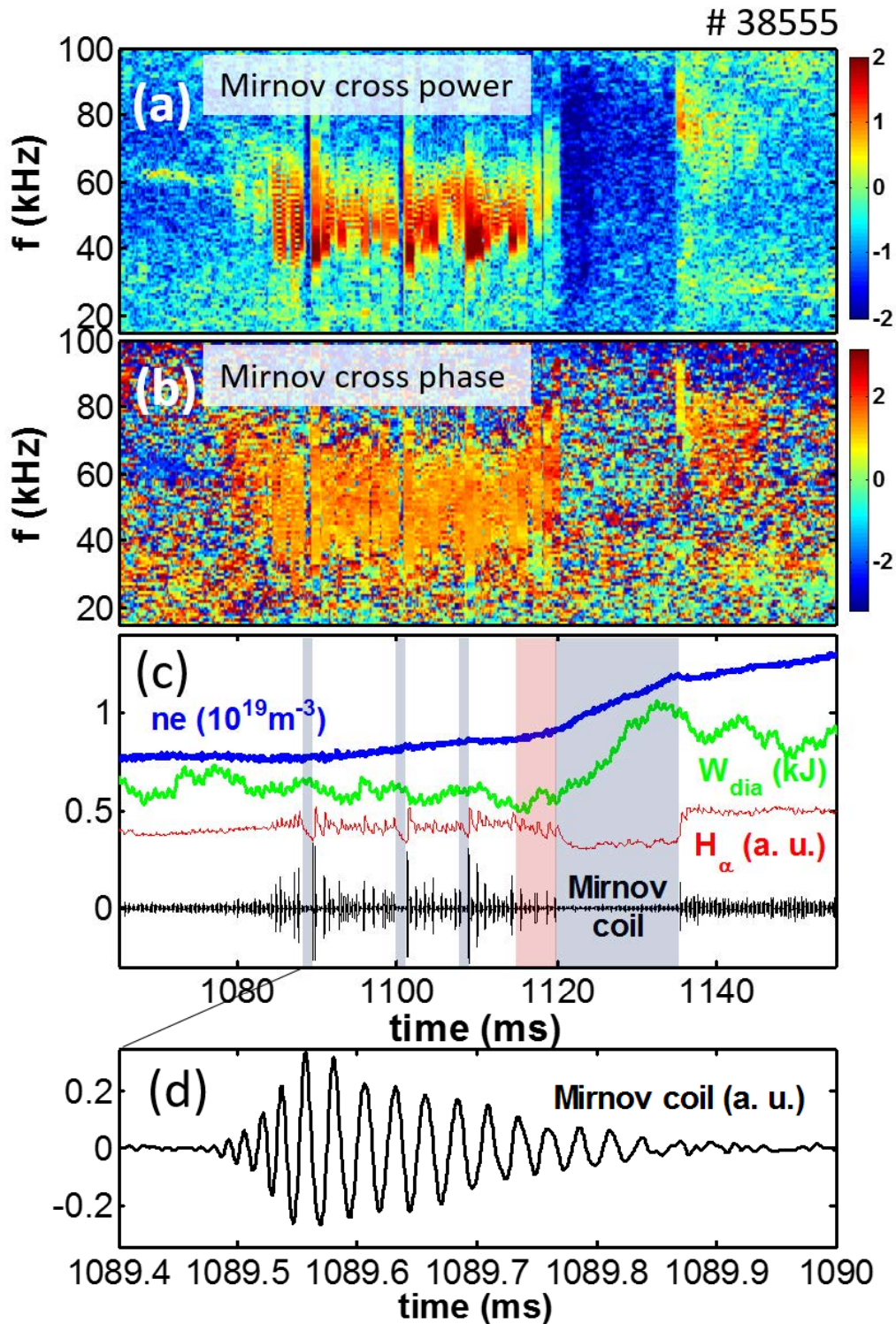


Figure 2.7 TJ-II discharge #38555. (a) Cross-power and cross-phase (b) spectrograms of Mirnov coil data; (c) plasma parameters: \bar{n}_e , diamagnetic energy, H_{α} and Mirnov coil signals. The grey-shaded region indicates H-mode. (d) Detail of an MHD burst at the indicated times.

H-mode phases (see later). These periods are interrupted when the bursty mode is excited back, and normally at a higher magnetic disturbance level: Note that the frequency chirping range is also stretched, ranging from 80 kHz down to 35 kHz, just after each of these signaled quiescent phases. Figure 2.7(d) enlarges the short time during which a burst in MHD activity appears, so terminating the quiescent period. The chirping frequency can be appreciated by the eye, as well as the different time scales that correspond to mode growth (~ 0.1 ms) and decay (~ 0.3 ms).

In the pink-shaded region $1116 < t < 1120$ ms, prior to H-mode in figure 2.7, bursts in magnetic signals are gradually weaker and the H_α trace tends to drop. This discharge illustrates also the intermediate state during the back transition to L-mode: at $t = 1135$ ms, the H-mode ends with a new emergence of the bursty mode. The H_α signal undergoes a steep increment, and the density slightly drops before ramping up slowly. Broad-band magnetic fluctuations are also recovered with the same cross-phase as due to the same magnetic structure (figure 2.7(b)). However, despite the weaker amplitude, the chirping happens at a higher frequency level, from 100 kHz down to 60 kHz, as expected from the larger diamagnetic and electric drifts after some 15 ms of plasma build-up.

The evolution of the local electron temperature during the bursty mode activity is shown in figure 2.8, where we zoom in a short (10 ms) constant density period $\bar{n}_e = 0.8 \times 10^{19} \text{ m}^{-3}$ of discharge #38555 (figure 2.7). The chirping consists of a repetition of individual MHD events, starting at each vertical line, that are best appreciated when their amplitude is large (e.g. just before 1090 ms, see also figure 2.7(c-d)). A pivot radial point, ρ_p , is clearly deduced from both signals, temperature and radiation. Preceding the burst there is a quiescent phase during which T_e increases for $\rho < \rho_p < 0.5$ but tends to decrease for $\rho > \rho_p$, an obvious expectation for a transport barrier at ρ_p with most of the heat source inside. The barrier is broken in a very fast time-scale, not resolved in the figure, in view of the sudden change of tendency starting at each vertical line: $T_e(\rho < \rho_p)$ drops sharply while it increases for $\rho > \rho_p$. Then the chirping starts from a high frequency (≈ 60 kHz in figure 2.7(a)) growing in amplitude for some 100 μs and then decaying in around 300 μs (see figure 2.7(d)). Observe the important fact that when this decay starts, the barrier gets re-established: $T_e(\rho < \rho_p)$ increase again while they decrease outside ρ_p . Reconstructed radiation emissivities from different radii are shown also in figure 2.8 to confirm the existence of a pivot point $\rho_p \lesssim 0.5$. Bolometry data are shown to connect this work with the results of Ref. [53], namely, that the bursts are MHD failures of an already established transport barrier around the resonant location, which justifies our previous statement about “short-lived” H-modes during the quiescent phases in figure 2.7. We must underline that the examples here shown are illustrative of very common phenomena in TJ-II plasmas.

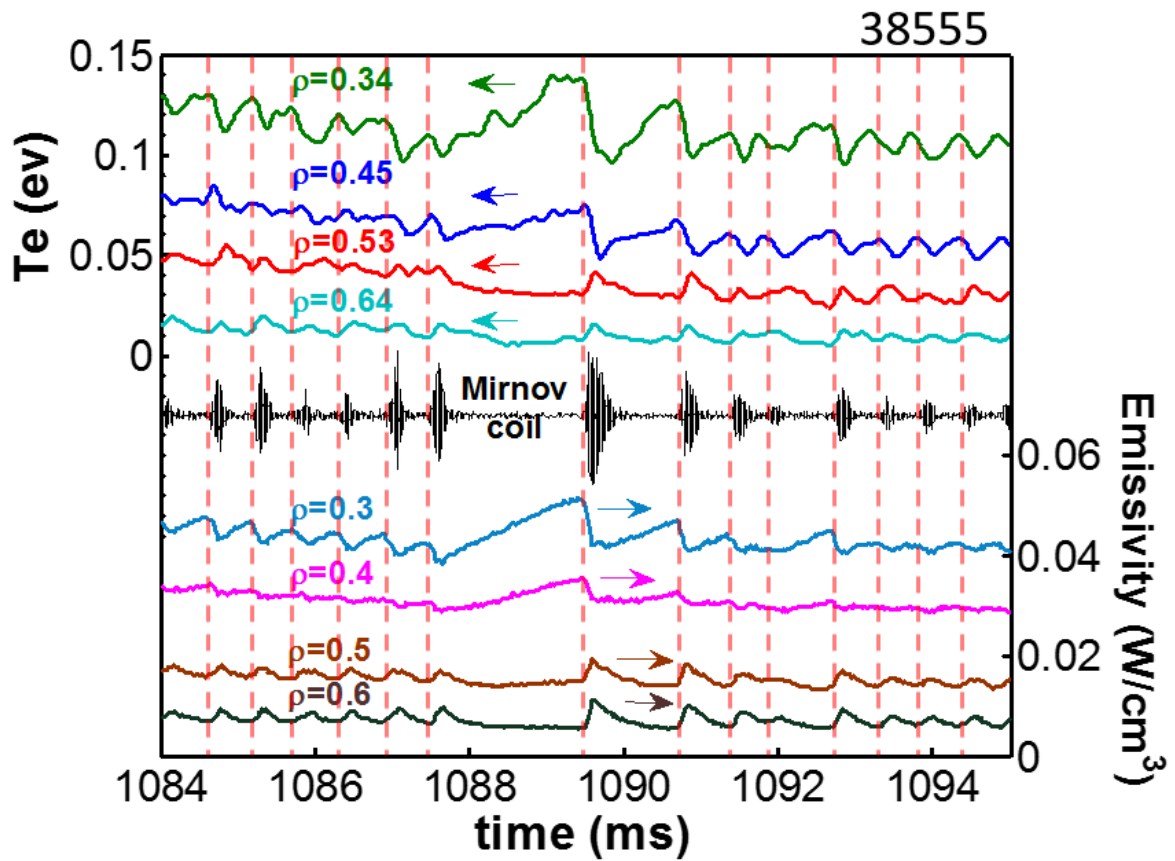


Figure 2.8 TJ-II discharge #38555. Time evolution of the electron temperature and radiation emissivities from different radii (labelled) showing the existence of a pivot point around mid minor radius; and Mirnov-coil signal ($5 \text{ kHz} \leq f \leq 100 \text{ kHz}$).

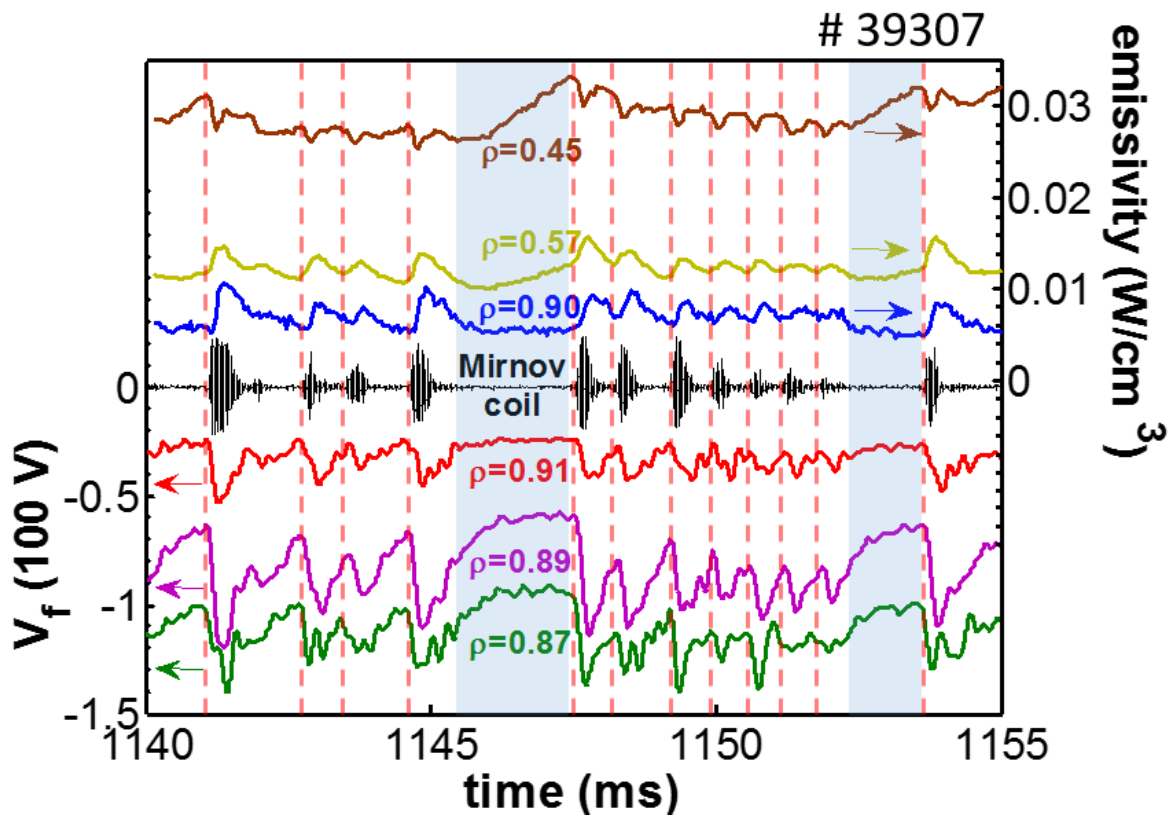


Figure 2.9 Discharge #39307 with $\iota = 3/2$ around $\rho = 0.5$. Time traces of: radiation emissivities from the indicated radii, Mirnov-coil signal ($5 \text{ kHz} \leq f \leq 100 \text{ kHz}$ frequency band) and V_{fl} from Langmuir probes at $\rho = 0.91$, $\rho = 0.89$ and $\rho = 0.87$. Shaded regions mark the longest time windows of H-mode.

Regarding the edge, where ECE measurements are not possible in the TJ-II, we have turned to a discharge where floating potential, V_{fl} , measurements are available from electric probes. V_{fl} can illustrate with good time-resolution the arrival of transport pulses to the edge because it is sensitive to plasma potential and electron temperature. In figure 2.9 we show data from discharge #39307, operated in a magnetic configuration where $\iota = 3/2$ is located around mid-radius. Low-pass filtered (10 kHz) V_{fl} signals from a multi-pin electric probe [64] are shown for pins inserted at three nearby radial locations, along with magnetic signals. During the short quiescent MHD periods of H-mode (we highlight the longest ones with shading) the edge plasma shows an increment of V_{fl} up to eventual saturation. V_{fl} undergoes a sudden drop in coincidence with the onset of the next bursting chirping mode. Vertical dashed lines indicate the instants when the innermost probe ($\rho = 0.87$) starts dropping, so we can appreciate that outer probes are slightly delayed as expected from outwards propagation. The emissivities from several radii are also plotted in figure 2.9 to establish a clear link between the MHD events originated around the resonant location (here $0.45 < \rho_p < 0.57$) and the probe measurements. In particular, note how $V_{\text{fl}}(\rho = 0.91)$ mirrors the emissivity from $\rho = 0.90$ (the same happens with other radial locations), a clear indication that V_{fl} is contributed by T_e .

2.5 Discussion

The phenomenology here described is found mainly in TJ-II plasmas with good wall conditioning and, even in this case, with either co-injection or balanced injection. It is in these plasmas, characterized by peaked density profiles and higher edge temperatures [65], where an L-mode confinement can be well established and L to H transition phenomenology can manifest [66]. We have evidenced that MHD events related with transport barrier breaking, stemming from resonant locations inside the plasma, have a rapid effect near the edge. Consequently, measurements anywhere downstream from the resonance might be affected by such events. This must be always checked before interpreting phenomena detected at the edge as local. Note also that, while resonant layers are characterized by a helicity associated to the corresponding low order rational of ι , they can provoke flux-surface wide transport pulses (i.e., with apparent $n = 0 = m$ structure) [38]. A strongly sheared electric drift by the resonant layer might be the cause for lowered transport in its vicinity, and then the sudden breaking of the barrier associated to MHD instability would release particles and heat with the observed spatial structure.

It has been also shown that the intermediate confinement state, characterized by an altered rotation of the magnetic islands (bursting chirping mode), is intimately linked to the

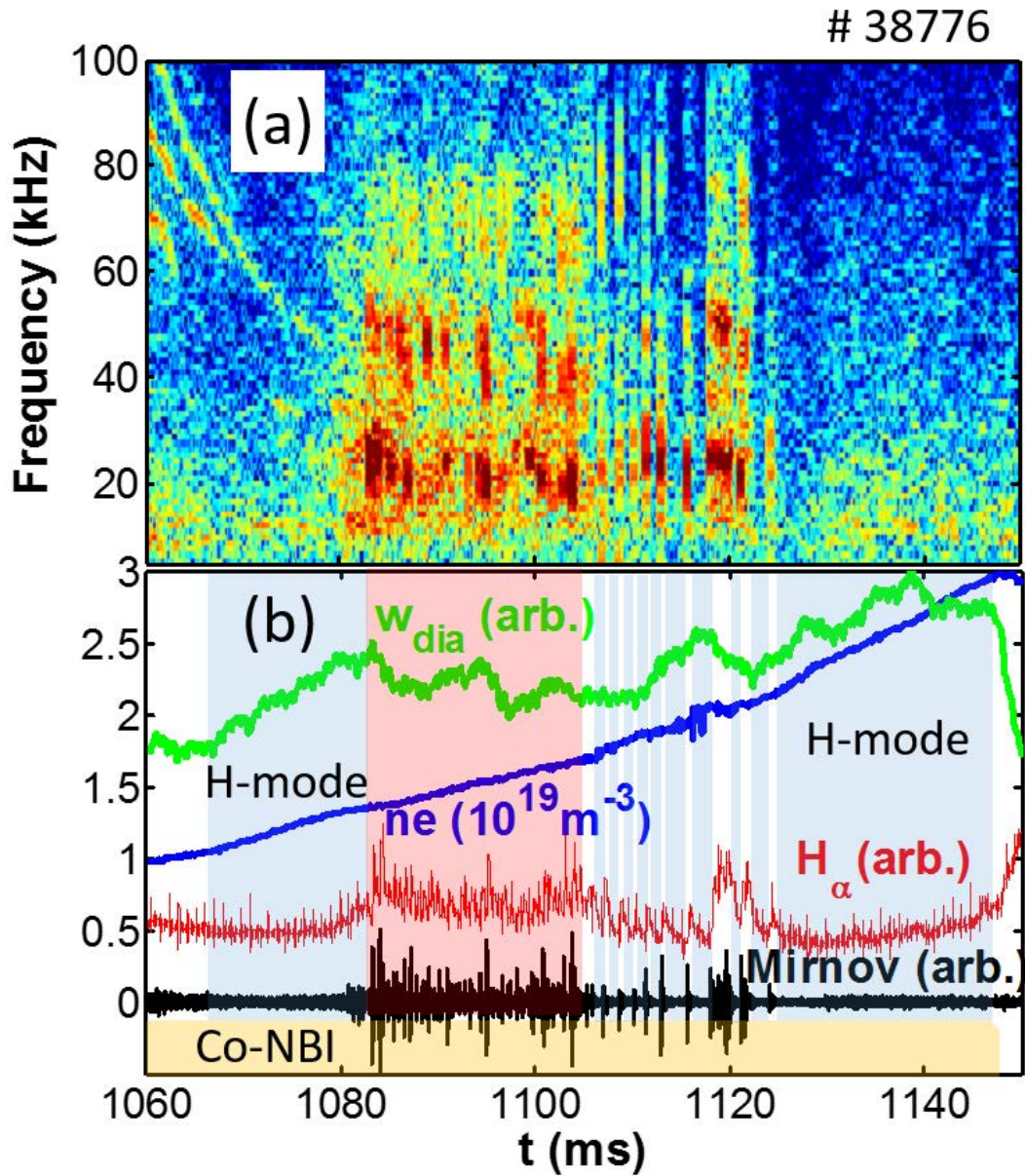


Figure 2.10 TJ-II discharge #38776. (a) Spectrogram of Mirnov coil data; (b) line average density, H_{α} , diamagnetic energy and Mirnov-coil ($5 \text{ kHz} \leq f \leq 100 \text{ kHz}$) signals.

repetitive breaking of confinement properties near the resonant layers. Therefore, the amount of transport regulation must depend on the repetition rates of these cycles of barrier build-up and failure. We illustrate this in figure 2.10 with a Mirnov coil spectrogram (a) and time traces for diamagnetic energy, line density, H_α and magnetic fluctuations (b) for TJ-II discharge #38776, very similar to discharge #39307 (figure 2.9) in terms of heating and magnetic configuration. Initial NBI phase has been labelled as H-mode in figure 2.10b because all H-mode signatures are present, although during this initial stage, the plasma profiles are evolving rapidly. The important observation is the evident worsening of confinement when the bursting mode starts. The magnetic activity during the bursty threshold mode shows, in addition to the fundamental ~ 25 kHz bursts associated to $\tau = 3/2$, two harmonics that should be related with the 6/4 and 9/6 helicities. For $1085 < t < 1105$ ms (pink shading), magnetic bursts have a relatively high repetition frequency, around 1.5 kHz, while the H_α signal is enhanced to a higher level and the diamagnetic energy is even decreasing despite the continuously increasing line average density. During the stage starting at $t = 1105$ ms (striped shading), H_α tends to decrease still in presence of pulsed transport towards the wall because the MHD bursts become less frequent, around 0.6 kHz, and the plasma confinement tends to improve. For $t > 1125$ ms, the bursty mode is suppressed, the H_α light falls to its lower level and the diamagnetic energy increases. Independently of whether we label this as H-mode, these observations dwell on the concept stated in [53] that the improved confinement is reached just because the capability of retaining transport at (or by) the resonant location resists the local plasma conditions. In consequence, confinement quality in TJ-II plasmas near the L-H transition threshold is related to the presence of magnetically resonant locations and their dynamics. This occurs naturally in our stellarator plasmas, but similar modulation of transport is tried using RMP control techniques in tokamaks.

Chapter 3

Alfvén wave including magnetic island effect

Coherent modes in NBI-heated plasmas of the TJ-II stellarator at frequencies generally below those of helicity induced Alfvén eigenmodes ($f < f_{HAE}$) but above tearing mode frequency range are explained as global Alfvén eigenmodes (GAE) and discrete shear-Alfvén eigenmodes induced by a non-rotating magnetic island (MIAE). Rotating islands are also found to interact with Alfvén eigenmodes: if they share the same helicity, they disturb each other; otherwise, new Alfvén modes can be excited via wave-wave coupling.

3.1 Introduction

Hannes Alfvén discovered that an electromagnetic wave could exist in a conducting fluid (plasma) in the presence of magnetic field. The transverse wave propagates along magnetic field line non-dispersively at a speed called Alfvén speed, $V_A = B/\sqrt{\sum n_i m_i}$, where $\sum n_i m_i$ is total plasma ion mass density, and the wave is called Alfvén wave. For shear Alfvén wave, where magnetic field lines are purely bended (no compression), the Alfvén wave frequency can be simply calculated by $\omega = k_{\parallel} V_A$, where k_{\parallel} is the wave number along the magnetic field line. In a slab model, where the plasma density is nonuniform across the magnetic field, the Alfvén speed varies in the density gradient region depending on local plasma parameters, thus constituting a continuous spectrum in frequency. Collisionless dissipation due to “phase mixing” provokes strong damping of Alfvén waves. In linear theory, the damping rate of this so called “continuum damping” is proportional to the radial variation $d\omega/dr$.

Since Alfvén waves propagate mainly along the magnetic field line [67], in magnetic fusion devices they form a flux-surface oscillation. However, the magnetic field strength is not

uniform on the flux surface and the Alfvén speed is periodically modulated as it propagates. This opens frequency gaps for two counter crossing Alfvén waves. In combination with plasma and magnetic field inhomogeneities and kinetic effects, discrete Alfvén eigenmodes [68] exist within the frequency gap that avoid the continuum damping. For tokamaks, where the magnetic inhomogeneity mainly comes from toroidicity, the induced eigenmode is called toroidal induced Alfvén eigenmode, commonly known as TAEs [69]. In stellarators, in addition to toroidicity, the magnetic strength is also modulated by helical coils and the helicity induced Alfvén eigenmode (HAE) is also predicted [70]. The variation of rotational transform also contributes to the Alfvén continuum frequency because $k_{\parallel} = (m - nq)/qR$. In some conditions, there are maximum and minimum values of Alfvén frequencies, and a single Alfvén eigenmode can exist residing at those extreme points: it is called global Alfvén eigenmode if it is a minimum, and reverse shear Alfvén eigenmode (RSAE) if maximum.

Since fast propagating Alfvén waves provoke both electric and magnetic perturbations, they can exchange energy and momentum with charged particles when they share a comparable velocity. Such resonant process, where particles see Alfvén wave in a static frame, can happen for particles whose speed is well above thermal. For example fast ions generated during NBI and ICR heating. The characteristic frequencies of those fast ions, such as passing or trapped, are rather comparable with TAE, RSAE, HAE, etc. These Alfvén eigenmodes undergo weak continuum damping and can be easily driven unstable by tapping free energy of the fast ion population in both velocity and spatial space. The poloidal electric field component will convect resonant particles radially, thus flattening the fast ion gradient and even scatter them into the loss cone. In present fusion devices such as W7-X and the forthcoming ITER, which are going to demonstrate the potential to be a reactor, fast particle confinement is of great issue. On one hand, it is crucial to understand Alfvén wave destabilization and fast particle confinement. On the other hand, it is very necessary to explore effective tools to control Alfvén wave in order to achieve self-heating in ITER and future reactors.

Conventional Alfvén eigen-values and functions are solved by using ideal MHD equilibria, which assume perfect flux surfaces and constant parameters on them. However, flux surfaces in magnetic fusion plasmas may be perturbed and destroyed locally by the development of magnetic islands. Consequent spatially periodic modulations of the metric coefficients and magnetic field strength can have an impact on Alfvén eigenmodes (AEs) located within the island influence range, or even ease the appearance of new types of Alfvén eigenmode. Only recently, works have been devoted to understand how perturbed flux surfaces, using external non-resonant and resonant magnetic perturbations, affect AE stability. Since magnetic islands can also appear naturally in toroidal fusion plasmas, it is in order searching for relationships between them and AEs. Some examples are the theoretical works on magnetic island induced

Alfvén eigenmode within island [71] and the effect of islands on the Alfvén continuum [72], the studies of shear Alfvén wave coupling with tearing modes found in HL-2A [73] or the beta-induced Alfvén wave in presence of a magnetic island in FTU [74].

Given that low order rational surfaces can be well controlled in TJ-II plasmas, this device provides an opportunity to study rational surfaces and island effects on Alfvén waves. In this work we propose an explanation for intermediate frequency (below typical HAE gaps) electromagnetic activity observed in TJ-II plasmas in terms of GAEs and new Alfvénic modes induced by coupling with magnetic islands; that is, we identify global Alfvén eigenmodes near an extremum of the continuum spectrum, as also found in the W7-AS, LHD and Heliotron-J devices, but also consider possible weakly damped modes in the gap due to the interaction between shear Alfvén waves and magnetic islands. Note that this magnetic-island induced Alfvén eigenmode (MIAE) should inherit all properties of the HAE family without assumptions beyond the existence of gaps opened by the magnetic islands; and yet, however, the MIAE seems to be the missing ingredient to explain TJ-II phenomenology. In addition, a clear interaction is detected also between Alfvén waves and rotating islands.

In this chapter, we give a quick overview of the phenomenology based on an illustrative discharge in Sec. 3.2. A brief description of the AE models (GAE and MIAE) is provided in Sec. 3.3, and their convenience to describe the experiments is shown in Sec. 3.4 with conventional examples. Next, in section 3.5, we identify the coupling of Alfvén waves and rotating islands. In section 3.6, after testing the predictions of the model in less conventional discharges (e.g. dynamic magnetic configuration scans) we discuss some general implications.

3.2 Phenomenological aspects

The interest on the modes here studied originated from salient features first presented in [75], like (i) the tight correlation between some intermediate frequency ($f_{TM} < f < f_{HAE}$) coherent modes and the net plasma current, (ii) their independence of the line-averaged electron density and (iii) their radial displacement. These modes are driven by fast ions and localize mostly in the region $\rho \geq 0.5$. They can be easily detected by most diagnostics with enough time resolution probing that zone, like bolometers, reflectometers or heavy-ion beam probes (HIBP); and sometimes, but not always, they are also detected by Mirnov coils and Langmuir probes. For co-NBI heated plasmas and moderate electron densities ($\bar{n}_e = 1.0 - 2.5 \times 10^{19} \text{ m}^{-3}$), their frequency mimics almost exactly the opposite evolution of I_p and seems not being affected by the evolution of the line-averaged electron density. However, small transport events, like a low amplitude off-axis sawtooth, can interrupt some modes and give rise to the birth/intensification of a higher frequency mode/branch that keeps

the same relation with plasma current. Also, the injection of small amounts of impurity species or launching short 28 GHz microwave pulses that do not alter the line-averaged electron density or the plasma current, can notably shift the mode frequency.

A fundamental aspect of the coherent modes here studied is that they have resisted a satisfactory interpretation after systematic survey. The example that follows illustrates quite clearly many of the features of the coherent modes under study, together with the difficulty commonly found to explain their nature. Discharge #28158 in figure 3.1 is produced in a habitual magnetic configuration for the operation of TJ-II, 100_44_64 as shown in figure 1.5. Low order rational values $\iota = 8/5$ and $\iota = 13/8$ are located around $\rho = 0.75$ and $\rho = 0.875$ respectively. Figures 3.1a and b compare two power spectra from Mirnov coil and bolometer signals. Modes labelled 1 and 3 are well discriminated by both diagnostics. Mode 2 is only partially seen by the Mirnov coil until time $t = 1160$ ms, while the bolometer can trace it until the end of the discharge. In Chapter 2 we have already identified Mode 1 as a rotation of a magnetic island associated to $\iota = 8/5$ in the near edge region. It rotates in the electron diamagnetic drift direction with speeds close to the $E \times B$ drift. The wavy behavior of the frequencies of modes 2 and 3 is seen to oppose the waveform of the net plasma current in figure 3.1c. We note that the frequencies generally go down even though \bar{n}_e , also shown in figure 3.1c, decreases from 1.4 to 1.0 (in 10^{19} m^{-3} units) from $t = 1120$ ms to $t = 1180$ ms. Modes 2 and 3 show electromagnetic properties and stop when NBI heating does. Very importantly, there is an apparent anti-correlation of intensities between the rotation mode (mode 1) and mode 3: Before the appearance of mode 3 at $t \approx 1162$ ms, the $M = 5$ island rotation mode is strong and coherent. Between $t = 1162$ ms and $t = 1174$ ms, when mode 3 becomes strong, the rotation mode reduces considerably its amplitude and becomes less coherent; after $t = 1174$ ms until $t = 1188$ ms, the behavior reverses so that the rotation mode regains intensity while mode 3 is relatively weaker and less coherent than before. At later times, the rotation mode dims to near suppression and mode 3 intensifies again.

In search for a possible explanation about the nature of modes 2 and 3, we have run the STELLGAP code [76] based on the VMEC [77] equilibrium for the corresponding magnetic configuration and the density profile obtained from combined Thomson Scattering, interferometry and He-beam diagnostics (see [78] and references therein) at $t = 1201$ ms, indicated with a vertical line in figure 3.1. All possible low mode number ($m < 9$) and low frequency ($f < 400$ kHz) shear-Alfvén continuum lines are shown in figure 3.2. Note that the calculations are presented for mixed mode families, not for a fixed mode family as it is customary [76]. In this, like in many similar cases, no gap modes are found at the relevant frequencies below 200 kHz. This is particularly disturbing given the fact that these modes are very common in TJ-II operation [75]. It could be argued that there are GAEs associated

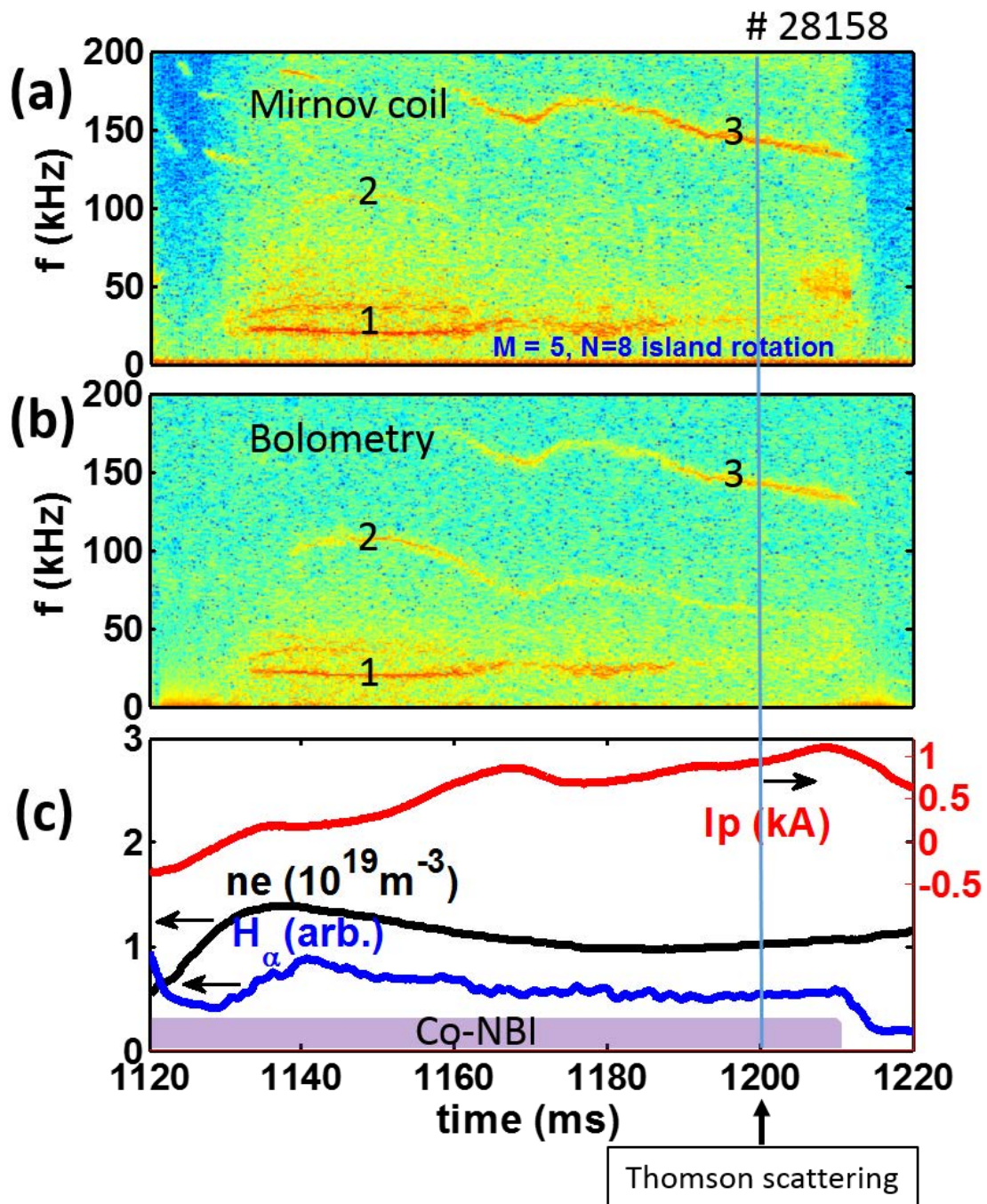


Figure 3.1 NBI heating phase in TJ-II discharge #28158. Spectrograms of Mirnov coil a) and bolometer b) signals. Mode labelled 1 has poloidal number $m = 5$ and is related with the rotation of $\iota = 8/5$ islands in the near edge region. Modes 2 and 3 are Alfvénic. c) Net toroidal current I_p , line-averaged density \bar{n}_e and H_α . A vertical line indicates the firing of the Thomson Scattering laser.

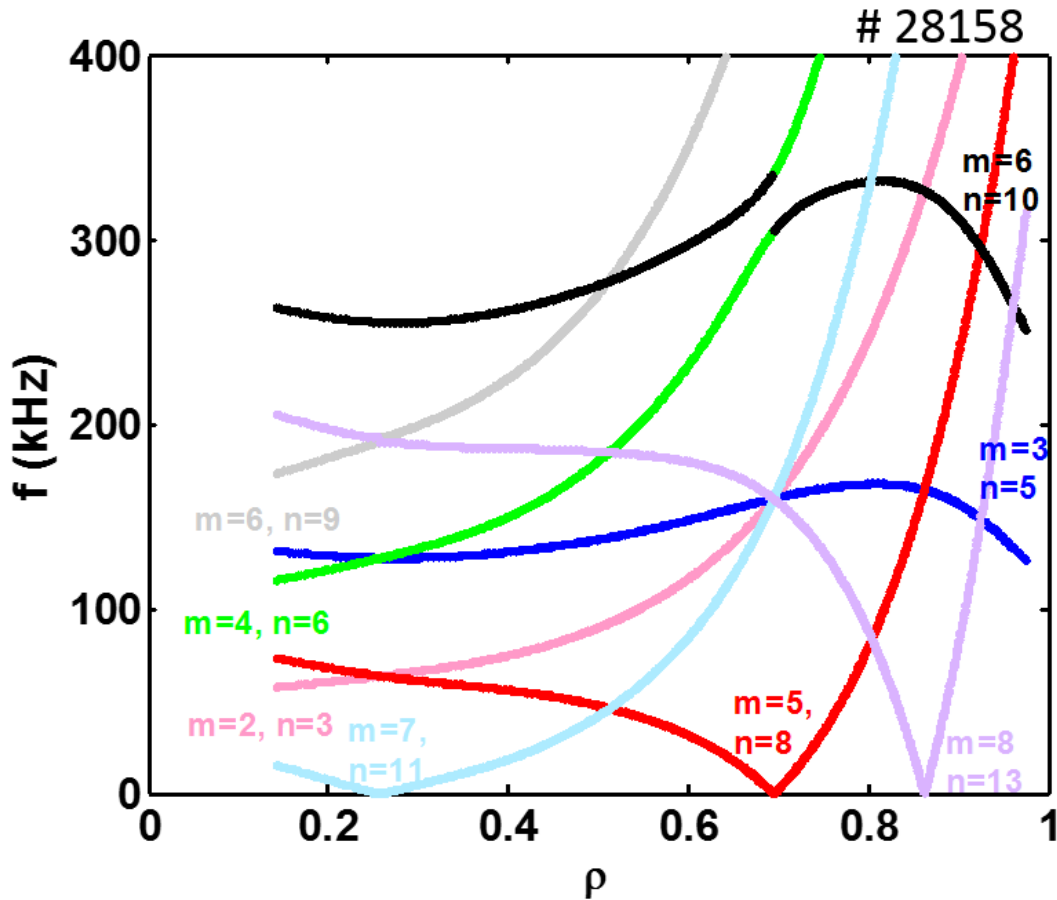


Figure 3.2 Shear Alfvén continuum spectrum for low mode number modes ($m < 9$) that below 400 kHz in #28158 at time $t=1200$ ms

to the maximum/minimum found for the ($m = 3, n = 5$) mode. The frequency associated with the maximum might explain the ≈ 150 kHz mode, but then the minimum at $\rho \approx 0.3$ with $f \approx 130$ kHz would be a bad candidate for the $f \approx 60$ kHz experimentally detected.

3.3 Models for low-frequency AEs in TJ-II plasmas

As we have seen in the previous representative example, and in agreement with previous literature for TJ-II, global AEs can be excited in NBI plasmas. Therefore we must consider this possibility. In addition, these modes presumed to be AEs are found better defined and highly coherent in configurations with the presence of lowest order rational surfaces, like $\iota = N/M = 8/5$, in the interval $0.6 \leq \rho \leq 0.9$ [75] (figure 3.1 provides indeed one such example). It is easy to identify the rotation of such lowest order magnetic resonances with mode analysis at the corresponding frequencies, due precisely to the low poloidal

mode number [79–81]. Higher frequencies with a similar behaviour, i.e., with proportional frequencies, are not detected –within diagnostic capabilities— with higher order values $M \geq 7$ often found in nearby locations. If these poloidal numbers are still low enough, e.g. $M = 9$, magnetic islands with a modulating effect in the magnetic configuration and metric coefficients might still develop. Therefore, and seeking for the simplest possible explanation, we propose that the existence of low order rational values in the rotational transform profile can open gaps not considered in the mode spectra of calculations like the one in figure 3.2.

3.3.1 Global Alfvén eigenmode above maximum of continuum spectrum

For shear Alfvén waves, the continuum spectrum obeys $\omega = (-m\iota + n)\omega_A = m(-\iota + n/m)\omega_A$ with ω_A defined as v_A/R , where v_A is the Alfvén velocity and R represents the major radius of the torus. For the peaked density profiles commonly found in the analysed discharges, ω_A is monotonically increasing towards the edge while $(-\iota + n/m)$ is monotonically decreasing if $n/m > \iota$ and $s > 0$. This is illustrated schematically in figure 3.3. Therefore, in discharges with some low order rational value of ι in the outer half of the plasma we expect that, from centre to edge, the spectrum first increases due to the ω_A contribution if $s \approx 0$, then decreases as $(-\iota + n/m)$ approaches zero at the resonant location. Thus, we can expect a maximum in $\omega(\rho)$ as shown in figure 3.3. Global Alfvén waves could exist with both frequency and position near this maximum thus avoiding strong continuum damping. This Alfvén wave is just like reverse shear Alfvén eigenmode (RSAE) in tokamaks, the non-conventional global Alfvén eigenmode (NGAE) found in W7-AS, and the GAE mode in LHD. Since the maximum value of the continuum spectrum corresponds to a specific value $\iota = \iota_g$, the GAE mode frequency can be rewritten as

$$\omega = m(-\iota_g + n/m)\omega_A, \quad (3.1)$$

so the mode frequency depends on mode number m , mode location distance with rational surface through $n/m - \iota_g$ (assuming a monotonic ι -profile), and local characteristic Alfvén frequency ω_A . In TJ-II, the vacuum rotational transform varies $\Delta\iota \approx 0.1$ from centre to edge as represented schematically in figure 3.3, and the most common lowest order rational surfaces are $\iota = 3/2, 5/3, 7/4, 8/5$. To obtain a rough estimate about the expected frequencies of these modes, we choose GAE mode numbers ($m = 5, n = 8$), expected differences $-\iota_g + n/m \approx 0.05$ for typical ι -profiles, and mode location where the local electron density is approximately the line average of typical low density NBI plasmas, $\bar{n}_e = 1.5 \times 10^{19} \text{ m}^{-3}$. With these numbers, GAE mode frequencies are expected around 130 kHz.

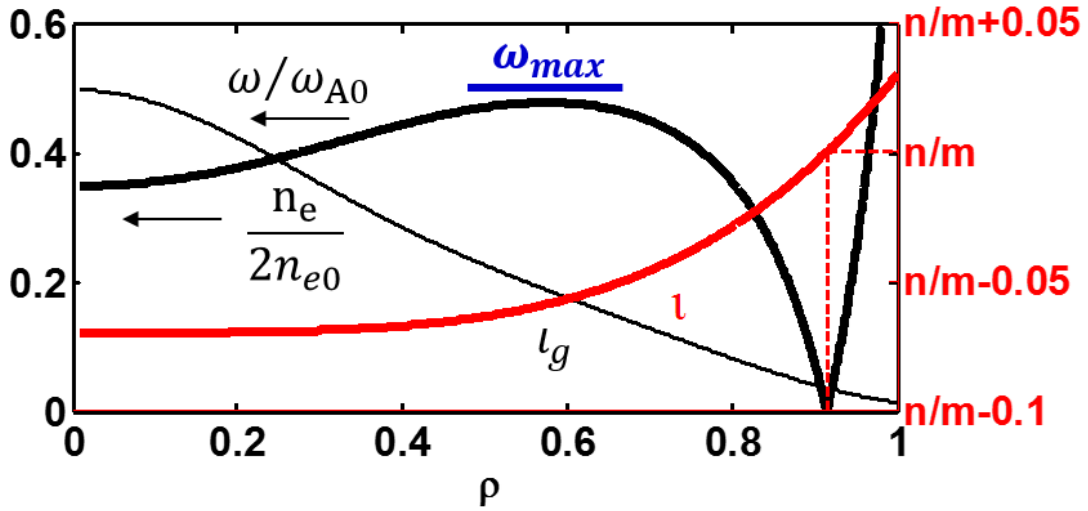


Figure 3.3 Schematic plot of TJ-II rotational transform profile, typical peaked density profile (thin black line), and corresponding (m, n) continuum spectrum (thick black line). A local maximum ω_{\max} appears at $\iota = \iota_g$ around $\rho = 0.6$. The profiles are normalised using centre values of the density, n_{e0} , and angular frequency, ω_{A0} .

In some configurations, HAEs can fall in those frequency range. Some examples will be shown in the next sections. However, we make explicit mention of the GAE because its appropriate frequency range and behaviour fits satisfactorily most of the cases surveyed.

3.3.2 Alfvén eigenmode induced by stationary magnetic islands (MIAE)

Since any periodic modulation of the Alfvén speed can in principle produce a frequency gap, here we assume that two counter propagating Alfvén waves are coupled due to the periodic wave speed modulation caused by a $\iota_{is} = N/M$ magnetic island, thus creating a gap size of order $b_{M,N}/B_0$, where $b_{M,N}$ is the amplitude of the radial component of the magnetic field originating the island and B_0 is the main magnetic field. We illustrate this concept in figure 3.4 with a schematic mode coupling at the island position $\iota_c = \iota_{is}$ with coupling strength distributed as a Gaussian with amplitude $0.3 = \max\{b_{M,N}/B_0\}$. Note that, assuming a monotonically increasing $\iota(\rho)$, the abscissa in figure 3.4 can be identified with the radial coordinate.

Based on this concept and using three-wave coupling conditions, the respective poloidal, m_j , and toroidal, n_j , mode numbers and frequencies of two shear Alfvén modes must satisfy:

$$m_1 = M - m_2; n_1 = N - n_2; \omega_1 + \omega_2 = 0 \quad (3.2)$$

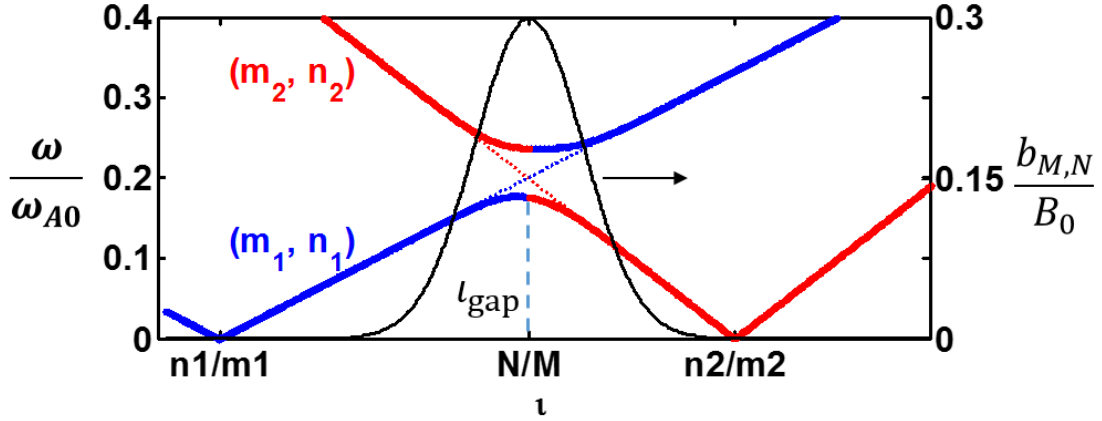


Figure 3.4 Schematic plot of the continuum spectrum in t -frame: coupling of modes (m_1, n_1) and (m_2, n_2) satisfying the condition $M = m_1 + m_2$, $N = n_1 + n_2$ (solid lines); and continuum spectrum for each single mode (dashes). The coupling zone is the vicinity of the rational surface $t_{is} = N/M$.

where $\omega_j = (-m_j t + n_j)\omega_A$. The island (M, N) does not rotate in magnetic field frame. The relation between mode frequencies holds for counter-propagating waves, while the relation between mode numbers requires that two shear Alfvén waves couple at the $t_c = t_{is} = N/M$ rational surface where the magnetic island (M, N) is assumed to exist. The gap mode frequency is

$$\omega = m_1(t_{is} - n_1/m_1)\omega_A, \quad (3.3)$$

very similar to the GAE mode frequency formula Eq. (3.1). Again, here assuming mode numbers $(m = 5, n = 8)$ and $|t_{is} - n/m| \sim 0.04$, we have $\omega \sim 0.2\omega_A$ and if the density at the mode location is $\bar{n}_e = 1.5 \times 10^{19} \text{ m}^{-3}$ as before, the mode frequency should be around 100 kHz.

The modes above, GAE and MIAE, are excited by the existence of NBI ions. The wave-particle resonance condition for passing fast ions is:

$$v \geq \left| \frac{m - nq}{m - nq \pm l} \right| v_A = \left| \frac{\omega/\omega_A}{\omega/\omega_A \pm l} \right| v_A, \quad (3.4)$$

where we take $l = 1$ considering toroidicity as the main contribution to particle drift. Since $\omega/\omega_A \ll 1$, then $v \approx 2\pi q R f$ and the resonance particle energy is simplified to $E = \frac{1}{2}m(2\pi q_c R f)^2$. Assuming hydrogen NBI-heated plasmas with mode frequencies $100 \text{ kHz} \leq f \leq 200 \text{ kHz}$, and configurations where $q_c = 1/1.5$ and $R = 1.75 \text{ m}$ (the equivalent major radius for TJ-II), the resonance condition needs $2.6 \leq E \leq 10 \text{ keV}$. These energies can easily

come after slowing down of fast ion birth energies of $E_b/3$, $E_b/2$, and E_b , where the full particle energy is less than 35 keV.

3.4 Experimental identification of GAE and MIAE

Figure 3.5 shows data from discharge #28275 produced in the magnetic configuration labelled 101_42_64 where ι value is slightly lower than 100_44_64, then $8/5$ rational surface is shifted a little outward. The plasma is started by ECRH and further heated by co-NBI (port-through power 0.58 MW, acceleration voltage 30 keV). During the time interval $1230 \leq t \leq 1290$ ms, the spectrogram obtained from a bolometry chord (a) shows two wavy coherent modes between 80 kHz and 150 kHz (mode 1 and mode 2) that almost mirror vertically the evolution of the plasma current (b); that is, when the current increases the frequency decreases and conversely. However, the line-averaged density traced in figure 3.5b is rather constant, or monotonically increasing, and the total current I_p changes less than 1.5 kA. The low frequency coherent mode ≈ 20 kHz also appearing in figure 3.5a, has poloidal mode number $M = 5$ and is related with the main $\iota = 8/5$ magnetic resonance rotating in the electron diamagnetic drift direction [81]. In general, the modes associated to plasma rotation in these co-NBI plasmas remain quite steady unless there is a significant confinement change, like in the L-H transition.

Mode 1 and mode 2 can coexist in time, but it is a common observation that when mode 1 is intense, mode 2 is very weak or not detected; and when mode 1 ceases then mode 2 becomes suddenly intense but normally less coherent than mode 1. It is interesting to note, as it is also a common observation, that the island rotation is non-coherent and weak when mode 1 appears. However, mode 2 seems to have no interaction with the island rotation.

Despite the larger frequency, mode 2 is more inside the plasma –where the density is larger– than mode 1. In figure 3.6 we compare the intensities of bolometer chords named ABOL1 (impact parameter $\rho = 0.84$), ABOL2 ($\rho = 0.66$) and ABOL3 ($\rho = 0.51$). It is evident that the two outermost chords, ABOL1 and ABOL2, have a relative higher signal during mode 1, while ABOL2 and the innermost ABOL3 ($\rho = 0.51$) are more intense during mode 2. In particular, the intensity of extreme bolometers, ABOL1 and ABOL3, practically exchange roles at $t \approx 1260$ ms as it is expected if the perturbation associated to mode 2 is more inside the plasma.

Figure. 3.7a shows all possible low mode number ($m < 10$) and low frequency ($f < 400$ kHz) shear-Alfvén continuum spectra calculated from STELLGAP at the Thomson Scattering time in figure 3.5. Two HAE gaps named HAE_{2,4} and HAE_{3,4} are due to magnetic helical components ($m = 2, n = 4$) and ($m = 3, n = 4$), which naturally exist in the corresponding

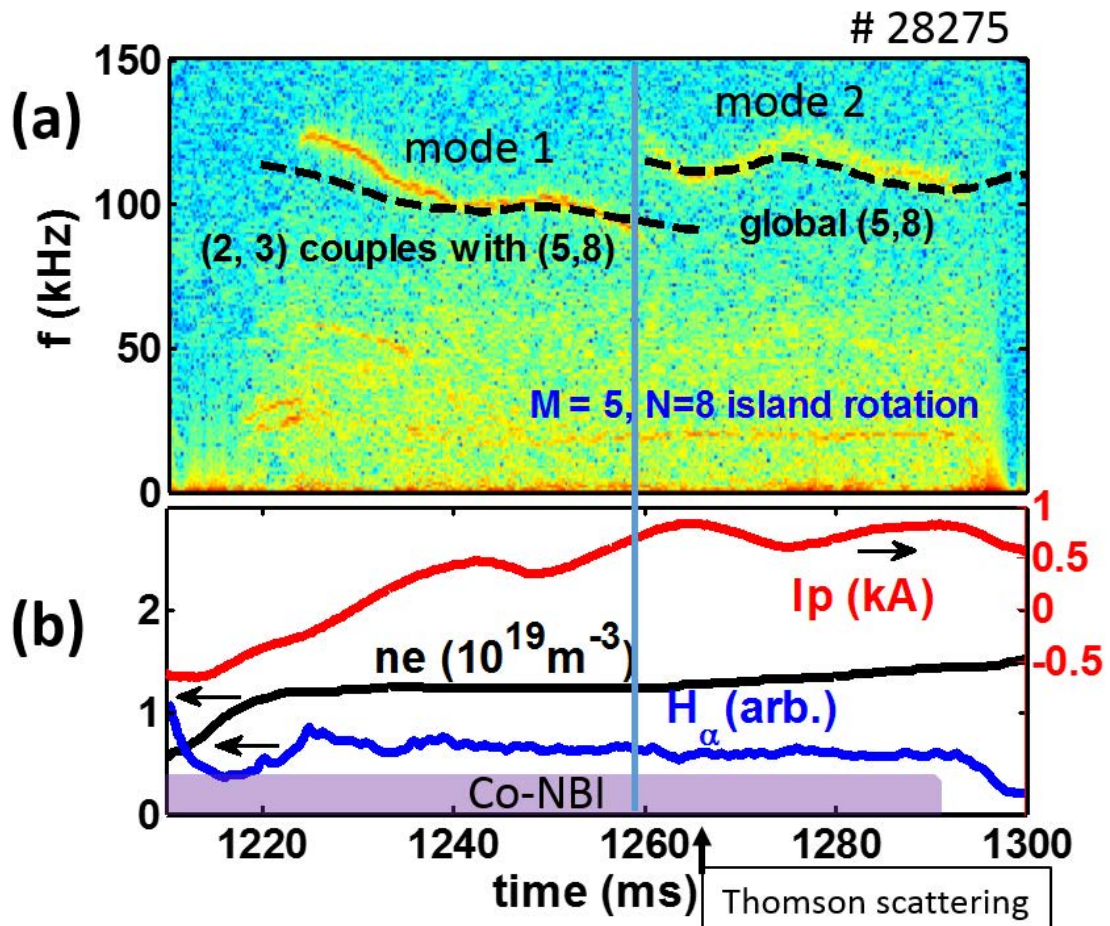


Figure 3.5 TJ-II discharge #28275 during co-NBI heating. a) Spectrogram of a bolometry chord with impact parameter $\rho = 0.84$, and predicted frequencies (dashed lines) for shear-Alfvén (2,3) coupled to (5,8) for mode 1, and single (5,8) for mode 2. A vertical line is drawn where mode 2 appears just after mode 1 disappears. The $M = 5$ low frequency mode (≈ 20 kHz) is due to island rotation. b) Net toroidal current I_p , line-averaged density and H_α time traces. The firing of the Thomson Scattering laser is indicated.

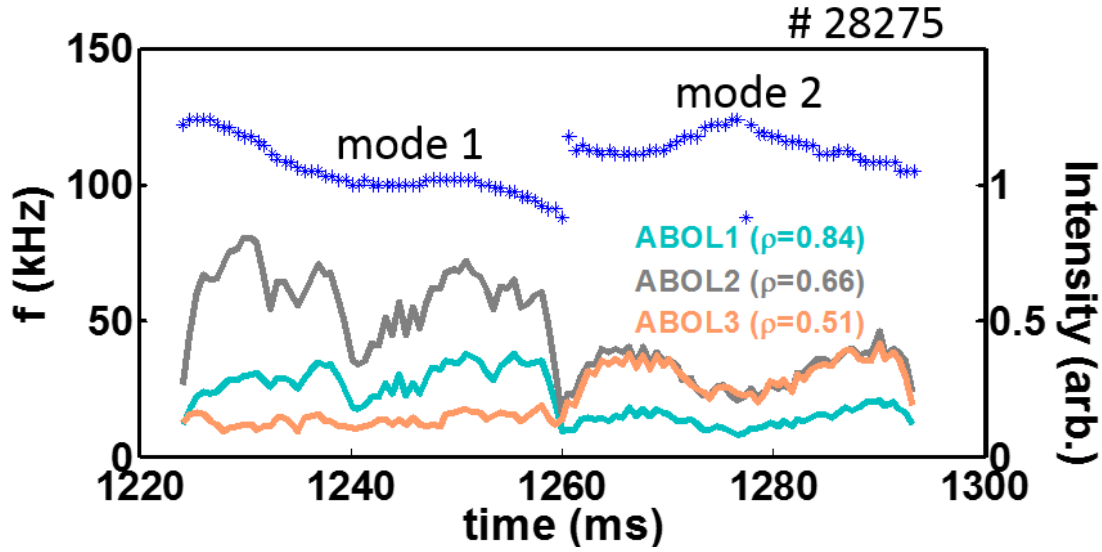


Figure 3.6 Intensity of modes 1 and 2 (figure 3.5) detected by bolometer chords with different impact parameters: ABOL1 ($\rho = 0.84$), ABOL2 ($\rho = 0.66$) and ABOL3 ($\rho = 0.51$).

TJ-II vacuum configuration. A GAE above the maximum frequency for the $m = 5, n = 8$ branch is due to the low magnetic shear near the magnetic axis, similarly to the prototype case of figure 3.3. The calculation in figure 3.7a does not show HAE gaps at the relatively low frequency range displayed in figure 3.5, and only the HAE mode at $f \sim 150$ kHz might be identified. Below 150 kHz, however, there are several spectrum crossing points at rational surfaces. For example ($m = 2, n = 3$) and ($m = 5, n = 8$) cross at the radial location ($\rho \approx 0.65$) of the resonant $\iota = 11/7$ (dashed circle). Let us assume that there is a locked island at the resonance. The continuum spectrum of two shear-Alfvén waves ($m_1 = 2, n_1 = 3$) and ($m_2 = 5, n_2 = 8$) is shown in figure 3.7b using the simplified cylindrical geometry. These two modes cross at $\iota_c = 11/7$, where the magnetic island may cause the appearance of a frequency gap. Aside from extracting the relevant modes, the main purpose of comparing the STELLGAP and cylindrical calculations is to prove that the latter is, once the model is fixed, quite well suited to search for consistency in a wide variety of discharges despite the complicated magnetic geometry of the TJ-II device.

The two calculations in figure 3.7a and b, STELLGAP and cylindrical respectively, show also a local maximum frequency in the ($m_2 = 5, n_2 = 8$) branch of the continuum spectrum where a global Alfvén wave may exist with both, frequency and position, near the maximum. Therefore, based on the calculations we expect two different modes, a GAE and a MIAE. Their respective locations are consistent with the observations from bolometry (figure 3.6). Mode 1 locates in the outer half of the plasma ($\rho > 0.51$) and is quite likely close to the impact radius of the ABOL2 line of sight ($\rho = 0.66$), which has a large comparative intensity.

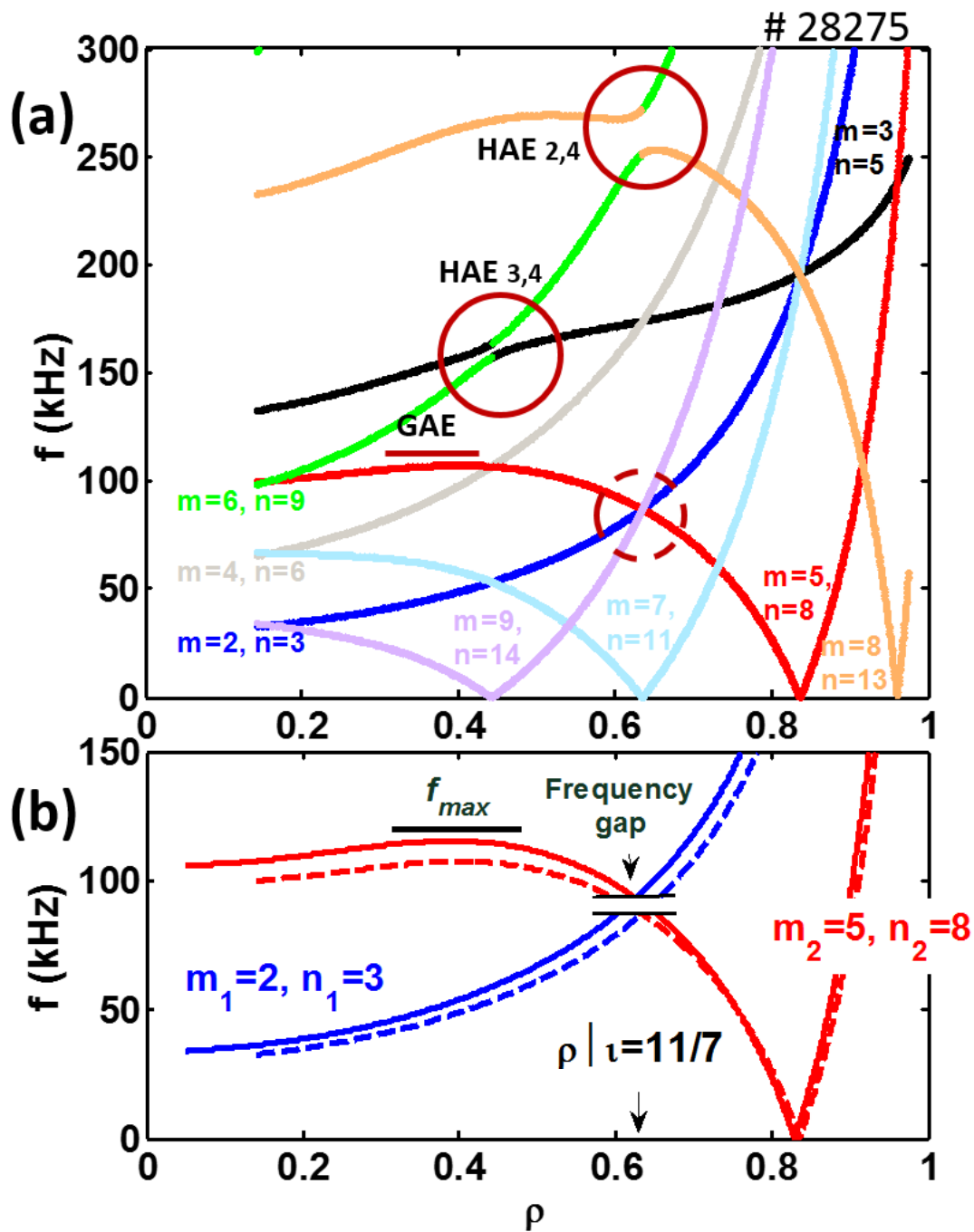


Figure 3.7 a) Low mode number ($m < 10$) shear-Alfvén continuum spectra in discharge #28275. Natural frequency gaps HAE and GAE are indicated by solid red circles and horizontal line respectively. A dashed circle indicates a possible MIAE. b) Detail of modes $(m_1 = 2, n_1 = 3)$ –blue– and $(m_2 = 5, n_2 = 8)$ –red– calculated using the cylindrical model (solid lines) and STELLGAP (dashed) at Thomson Scattering time, see figure. 3.5. Two short horizontal lines indicate the coupling zone around the magnetic island $M = 7, N = 11$.

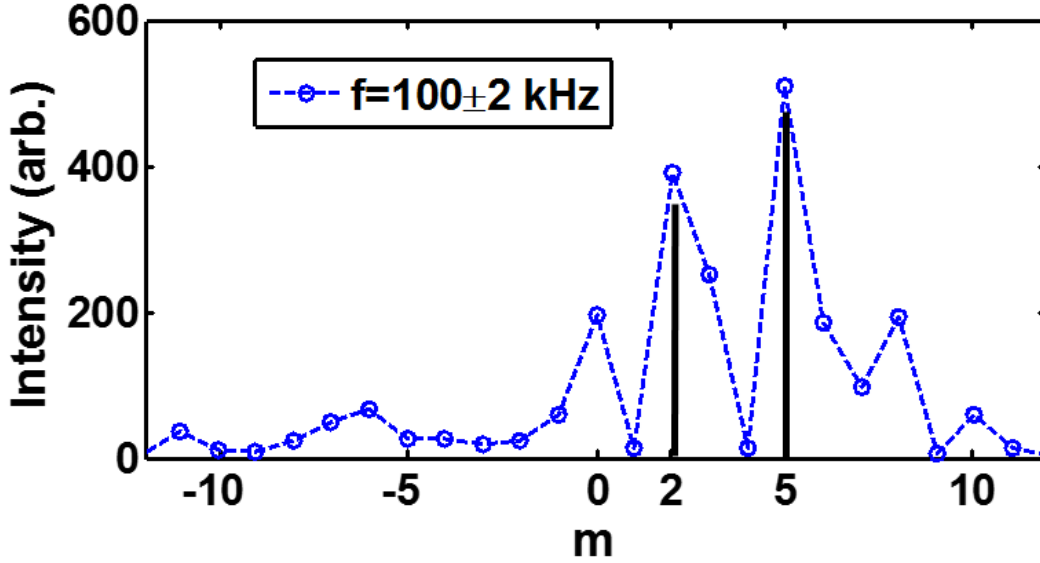


Figure 3.8 Poloidal mode number analysis of mode 1 ($f \approx 100$ kHz) within time 1240-1242 ms in figure 3.5 based on an array of Mirnov coils.

On the other hand, ABOL2 and ABOL3 ($\rho = 0.51$) have equal high intensities for mode 2 while the outermost chord ABOL1 barely detects it. According to mode location and frequency dispersion width, mode 1 behaves like the gap mode due to the island, while mode 2 is a GAE above the maximum frequency shown in figure 3.7. The poloidal mode number analysis based on an array of 25 poloidally distributed Mirnov coils indicates that the frequency of mode 1 is contributed by two mode numbers, $m_1 = 2$ and $m_2 = 5$, as noted in their higher intensities when mode 1 is active (figure 3.8). This is also consistent with the mode coupling model and, moreover, the presence of such mode numbers at this frequency would be difficult to justify otherwise. Since mode 2 locates deeper in the plasma, Mirnov coils can only weakly detect it and the mode number analysis is not possible.

Note in figure 3.7 that the gap (mode 1) and global (mode 2) modes share the same mode numbers ($m = 5, n = 8$) at different frequencies, but their locations are close enough, $\delta\rho \approx 0.2 \sim 3$ cm, that they can easily overlap. This may explain why they cannot coexist easily, as observed in many similar cases. In addition, mode 1 and island rotation share also the same mode numbers ($m = 5, n = 8$) and their locations are also close, $\delta\rho \approx 0.2$, so there might be an interaction that disturbs coexistence as well.

Assuming that the modes are the GAE and MIAE just described, we predict the frequency evolution shown with dashed-lines in figure 3.5a. Here the density-profile form is assumed fixed although the profile is normalised with the evolving line-averaged density. To simplify

the calculations, a current density with Gaussian profile peaked on axis is used:

$$\Delta\iota(\rho) = \frac{\mu R I_p}{2\pi a^2 B_T \rho^2} \frac{1 - \exp(-\frac{\rho^2}{2\sigma^2})}{1 - \exp(-\frac{1}{2\sigma^2})}, \quad (3.5)$$

where σ parameterizes the width of the current density profile. Note that, near the plasma edge, the exponentials practically cancel so the variation in ι is almost proportional to the net plasma current in this region. We choose $\sigma = 0.6$ in Eq. (3.5) and the cylindrical model (figure 3.7b) to estimate the time evolution of the mode frequencies. For mode 1 in figure 3.5a, the frequency gap position corresponds to a determined $\iota_c = 11/7$ that moves radially as the current modifies the ι profile. Following the local value of the density, the mode frequency decreases (increases) as the gap position moves inwards (outwards) due to the increasing (decreasing) plasma current, which causes the wavy changes in frequency opposing $I_p(t)$. Note that up to $t \approx 1240$ ms the H_α signal indicates that the plasma-wall interaction is not constant and the density profile shape, mainly at the periphery, should be evolving. Therefore the prediction based on a fixed form for $n_e(\rho)$ is not expected to be accurate.

For the frequency of the global mode (#2 in figure 3.5a), the small change in plasma current about $\delta I_p = 0.2$ kA leaves the location of the maximum almost unaltered, but the ι value at the location of such maximum, i.e., ι_g , increases as the positive current shifts up the ι -profile. Since $\iota_g < n/m$, an increasing current gets ι_g closer to n/m and, according to Eq. (3.1), $k_{||} \sim (-\iota_g + n/m)$ gets smaller and forces the frequency to decrease; and vice versa.

As a second example we have chosen a plasma built in a quite different magnetic configuration and heated with counter-NBI. Figure 3.9 corresponds to data from discharge #30092, produced in a configuration (100_36_62 in TJ-II terminology, see figure 1.5) in vacuum. The $\iota = 3/2$ resonance is located around $\rho = 0.64$. Counter-NBI is used for further heating after ECRH, which drives a negative current, see figure 3.9b. The average density \bar{n}_e , also drawn in figure 3.9b, is monotonically increasing from 1.1 to $3 \times 10^{19} \text{ m}^{-3}$. The spectrogram of a Mirnov coil in figure 3.9a shows several coherent modes between 50 and 200 kHz. During the interval $1140 \leq t \leq 1180$ ms, the mode frequency are slightly wavy against current despite the continuously increasing \bar{n}_e , a fact consistent with the MIAE or GAE modes discussed earlier. After $t = 1180$ ms I_p is rather constant, but the increasing \bar{n}_e makes all frequencies drop. Coherent mode 1 must be near the plasma centre because only bolometry chords passing around the centre can detect it intensely (**not shown**). Coherent mode 2 is strongly excited and is well detected by Mirnov coils and bolometers. Mode 5 is exactly twice the frequency of mode 2 and we ascribe it to a harmonic. Mode 3, which is little coherent before 1200 ms, seems to be a different type of mode in comparison with modes

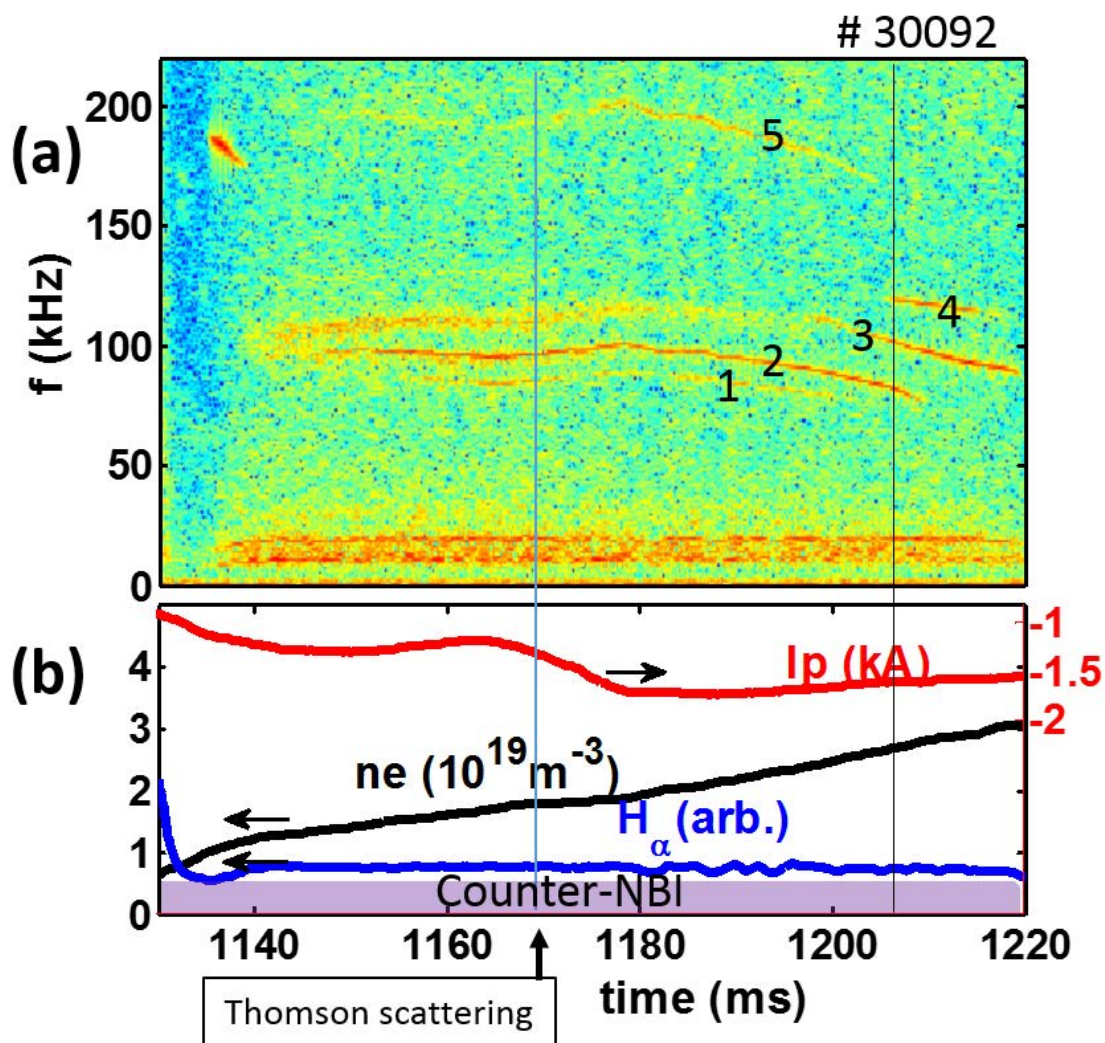


Figure 3.9 NBI heating phase in TJ-II discharge #30092. a) Coherent Alfvén waves with frequencies between 80 kHz and 200 kHz in the spectrogram of a Mirnov coil. Two less coherent modes below 30 kHz are related with the $\iota = 3/2$ rational surface and have respective mode numbers $M = 2$ and $M = 4$. b) Time evolution of net toroidal current I_p , line-averaged density and H_α light.

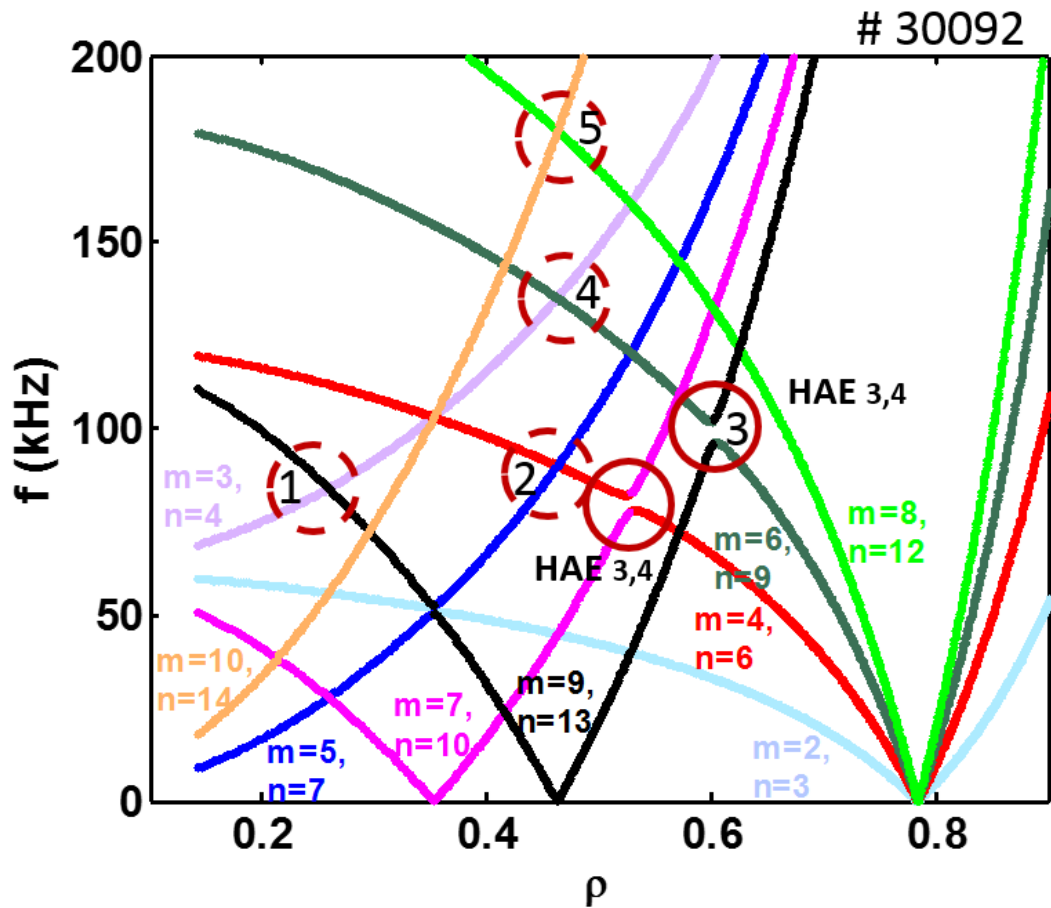


Figure 3.10 Continuum spectrum calculated from STELLGAP for TJ-II discharge #30092 at $t = 1170$ ms assuming that t is modified with $I_p = -1.34$ kA, and $\sigma = 0.3$ in Eq. (3.5). Two natural HAE_{3,4} gaps are marked with solid red circles. Dashed circles indicate possible gaps where magnetic island may develop. The numbers suggest correspondence with the mode labels in figure 3.9.

1, 2 and 5. Finally, coherent mode 4 appears approximately after mode 2 is suppressed, suggesting some relationship among them.

Figure 3.10 is a plot of all possible low mode number ($m \leq 10$) continuum spectra for frequencies below ≈ 200 kHz based on a STELLGAP calculation. The magnetic equilibrium is obtained using parameters at Thomson Scattering time, $t = 1170$ ms in figure 3.9, namely the density profile and $I_p = -1.34$ kA (with $\sigma = 0.3$ in Eq. (3.5)). The sole two natural gaps (encircled with continuous lines) cannot explain all the modes that show up in figure 3.9a. These natural gaps are of type $\text{HAE}_{3,4}$ and have respective frequencies around 100 kHz and 80 kHz. By comparing with the spectrum at $t = 1170$ ms (vertical blue line in figure 3.9a), mode 3 seems to match the 110 kHz $\text{HAE}_{3,4}$ resulting from the coupling of modes (9, 13) and (6, 9). At the position of the $\iota = 13/9$ rational, where a magnetic island may develop, two modes (5, 7) and (4, 6) cross at 90 kHz. This can explain mode 2 in figure 3.9a; and there is a second harmonic at the same location coupling modes (10, 14) and (8, 12) at frequency 180 kHz, which is quite possibly the case for mode 5.

Another possibility for coupling in figure 3.10 is (3, 4) and (6, 9) with frequency 135 kHz assuming a gap opened by the island ($M = 9, N = 13$), which is the same island as for the coupling of modes (5, 7) and (4, 6). We observe that the composition of wave-numbers matches the island helicity in both cases (four-wave coupling) but the couplings happen at different frequencies. Therefore these two couplings may disturb each other. Now we recall that mode 4 in figure 3.9a does not show up until mode 2 is close to disappear (notice vertical black line). If we assume that the frequency ratio between modes 4 and 2 (approximately 1.45 at $t = 1206$ ms) keeps constant during the discharge and we trace it back to $t = 1170$ ms, then the frequency of mode 4 should be around 140 kHz. All these facts combined make the coupling of modes (3, 4) and (6, 9) due to the ($M = 9, N = 13$) island a plausible explanation for mode 4 in figure 3.9.

Finally, there are two difficulties in the interpretation of figure 3.9 in view of figure 3.10. First, modes (3, 4) and (9, 13) cross in the core region ($\rho < 0.4$) at frequency 90 kHz. We have seen in figure 3.9 that mode 1 is a core mode with similar frequency, which is why we encircle a mode 1 also in figure 3.10 although we cannot propose an identification because the uncertainty about the ι -profile in the core region is large. Second, we have not mentioned anything about the $\text{HAE}_{3,4}$ at ≈ 90 kHz in figure 3.10 (encircled but not labeled). A possibility, assuming that the rest of the modes are correctly interpreted, is that its proximity both in frequency and space with mode #2 together with the shared (4, 6) branch make it difficult to excite it; or maybe the $\text{HAE}_{3,4}$ gap is not significant.

3.5 Coupling between rotating islands and shear-Alfvén waves

Once assumed the ability of *locked* islands to open gaps in the shear-Alfvén continuum of TJ-II plasmas, it is natural to search for the existence of couplings between *rotating* magnetic islands and alfvénic waves. Next we show that such couplings exist indeed, but the plasma conditions are different as it proves the fact that they have not been detected in the previous cases (figures 3.1, 3.5 and 3.9).

Discharge #19189 (figure 3.11) was operated in a magnetic configuration as in #30092 (3.9). Approximately balanced co- and counter- NBIs are used to heat the plasma with combined port-through power around 0.83 MW. Figure. 3.11a is the spectrogram of a Mirnov coil where several coherent modes below 300 kHz are clearly discriminated. Below 100 kHz, modes #1 and #2 with respective poloidal numbers $M_{3/2} = 2$ and $M_{6/4} = 4$ are strongly excited and can be identified as rotating magnetic islands related with $\iota = 3/2$. Between 100 kHz and 300 kHz, several branches of Alfvén modes are excited: the coherent mode #3 is excited independently of #1 and #2, as can be inferred from the fact that it remains after modes #1 and #2 are suppressed; while the existence of modes #4 and #5 is related with that of modes #1 and #2. After carefully checking simultaneous frequencies, it is clear that mode #2 is coupled with #3 producing mode #5; and #1 is coupled with #3 giving rise to mode #4.

We note that the mode that seems to behave independently (#3) shows characteristics that are similar to the cases presented earlier: its frequency is generally decreasing as the line-averaged density increases and there is a gentle modulation due to the plasma current effect, see figure 3.11b. This might be an HAE_{2,4} based on STELLGAP calculations (**not shown**). The main observation, however, is that an existing Alfvén mode (#3) can interact with a rotating island, which in essence provides a wave for the magnetic components, giving rise to new coherent modes.

Figure. 3.12 presents the case of a discharge (#21618) in the same magnetic configuration of discharge #28158 (see figure 3.1) but now 0.95 MW of simultaneous co- and counter-NBI are used to heat and fuel the plasma. According to the spectrogram in figure 3.12a, modes in a broad range of frequencies are excited: mode #1 is rotating quite steadily at 30 kHz with detected poloidal mode number $M = 5$, and is again related with the rational surface $\iota = 8/5$. The repeated frequency interval clearly visible between #2 to #6 is just the frequency of mode #1, while mode #2 appears quite independently of mode #1 and continues for a while when the discharge enters H-mode at $t \approx 1140$ ms (note H $_{\alpha}$ signal and \bar{n}_e in figure 3.12b) with a more pronounced decreasing frequency due to the growth and widening of the density profile. Mode #2 is identified as HAE_{2,4} due to the helical modulation coil M=2, N=4 (see circle in

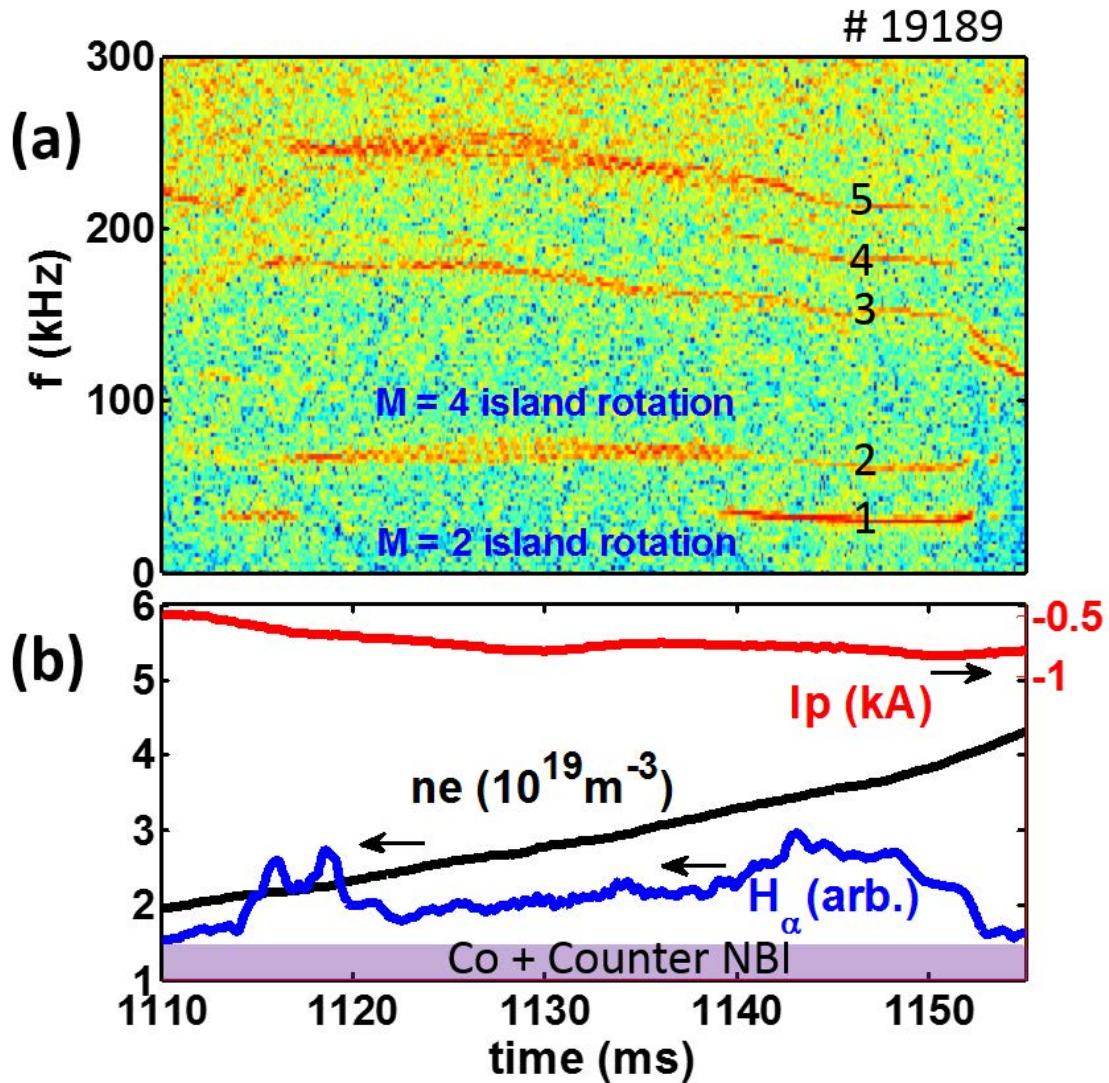


Figure 3.11 a) Spectrogram of a Mirnov coil for TJ-II discharge #19189. Coherent modes #1 and #2 with respective poloidal mode numbers -2 and -4 are related with the rational surface $\iota = 3/2$. Modes #3, #4 and #5 are Alfvén waves excited during NBI heating. b) Line-averaged density, toroidal current I_p , and H_α signal.

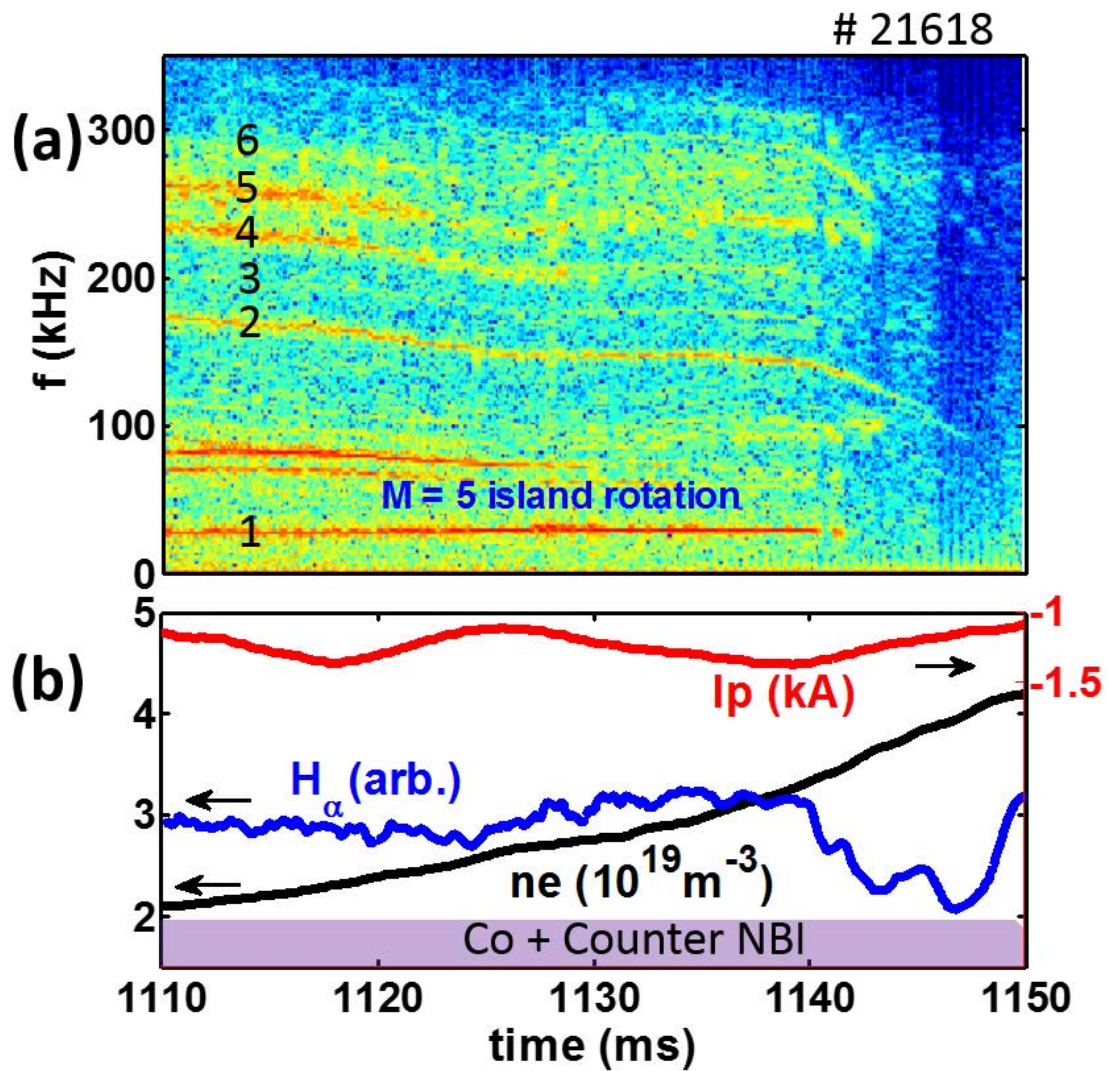


Figure 3.12 (a) Mirnov coil spectrogram for TJ-II discharge #21618 during the co+counter NBI phase. (b) H_α signal, line-averaged density, and toroidal current I_p .

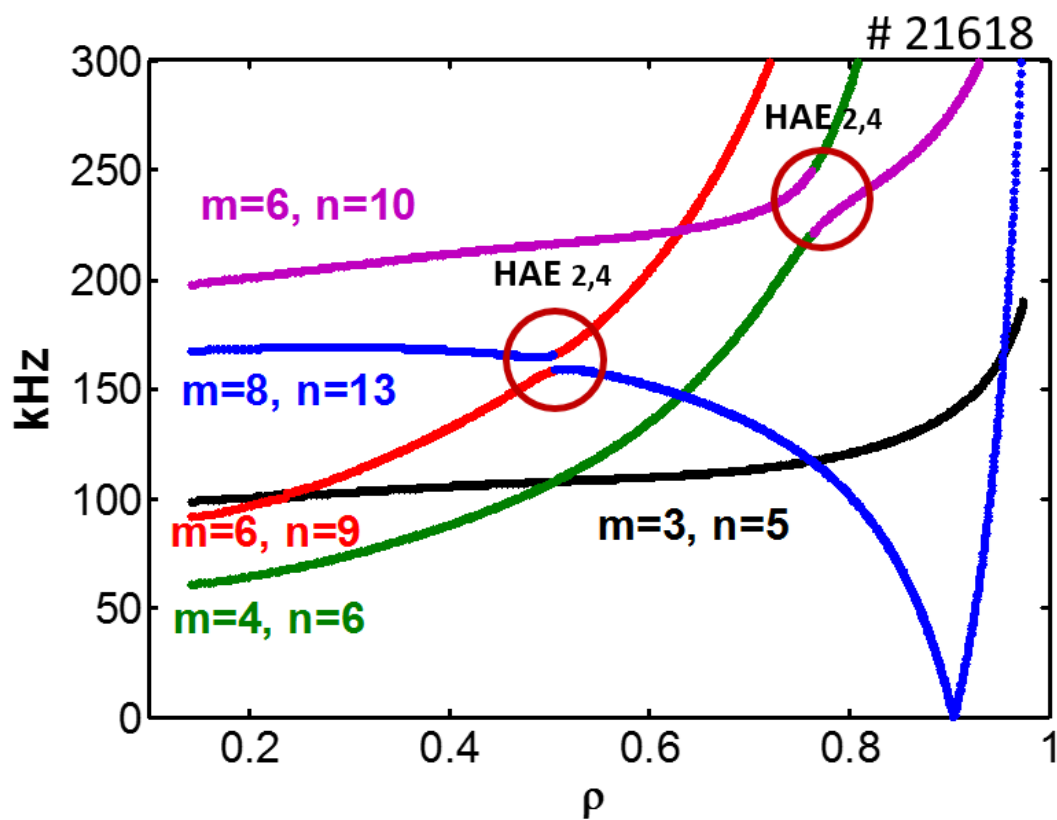


Figure 3.13 Continuum spectrum calculated from STELLGAP for #21618 using density profile measured at $t = 1125$ ms. A HAE frequency gap opens at $\rho \approx 0.5$.

figure 3.13). The predicted gap opens at $\rho = 0.5$ at frequency 160 kHz which is consistent with observed frequency at 150 kHz at $t=1125$ ms. The Alfvén eigenmode due two crossings (6,9) and (8,13) doesn't share the same helicity with the island rotation mode ($M=5, N=8$), thus the coupling with it generates new waves, and in this case, it cascades upward.

3.6 Discussion

We have seen that, especially considering uncertainties associated to the determination of the density profile, the effective atomic mass or the rotational transform profile, a cylindrical approximation is satisfactory to perform a first search for possible gaps or extrema in the spectrum (figure 3.7). Once established the possibility of the magnetic island induced Alfvén eigenmodes (MIAE), we have practiced studies like those shown above in many other discharges with different magnetic configurations and plasma parameters. Cases are abundant because Alfvén waves are ubiquitous in NBI plasmas of the TJ-II device. It is assumed that magnetic resonances can give rise to magnetic island structures, i.e., a well defined helicity –and possible harmonics– in the perturbation to the magnetic field. Not knowing beforehand what gaps are possible, we have followed some criteria to choose the gap-inducing island and the coupling modes. For the island, we always choose the lowest order rational that does not correspond to a rotating island, i.e., such that a coherent mode with the expected frequency is not detected. For the coupling modes there are normally several choices for a given island. We again use the criterion of combining lowest mode numbers at the island location. For TJ-II magnetic configurations, these couplings always have a contribution from the main magnetic resonances like $8/5$, $7/4$, $5/3$ and $3/2$. This can explain why, as observed originally [75], such low frequency coherent modes appear normally in configurations with low order rational values of ι around the outer half of the plasma.

The often wavy evolution of these modes is generally the consequence of changes in ω_A via the local mass density, which can in turn come from the movement of the gap location throughout the plasma or from a local change in density. We illustrate the latter case in figure 3.14, where a sudden change in recycling neutrals, possibly due to a small impurity entrance, affects the local densities and thus the frequency. It is TJ-II discharge #30827 in magnetic configuration 101_031_60 with vacuum edge $\iota_a = 1.5$, heated with counter-NBI with a port-through power of 0.56 MW. The spectrogram figure 3.14a shows a pronounced wavy evolution of the mode frequency in an opposite way to the edge H_α but rather unrelated with the evolution of the line-averaged density \bar{n}_e or the net plasma current I_p , see figure 3.14b, which are monotonically increasing. In this discharge the evolution of H_α light can be related with corresponding changes in the electron density near the plasma edge, which can

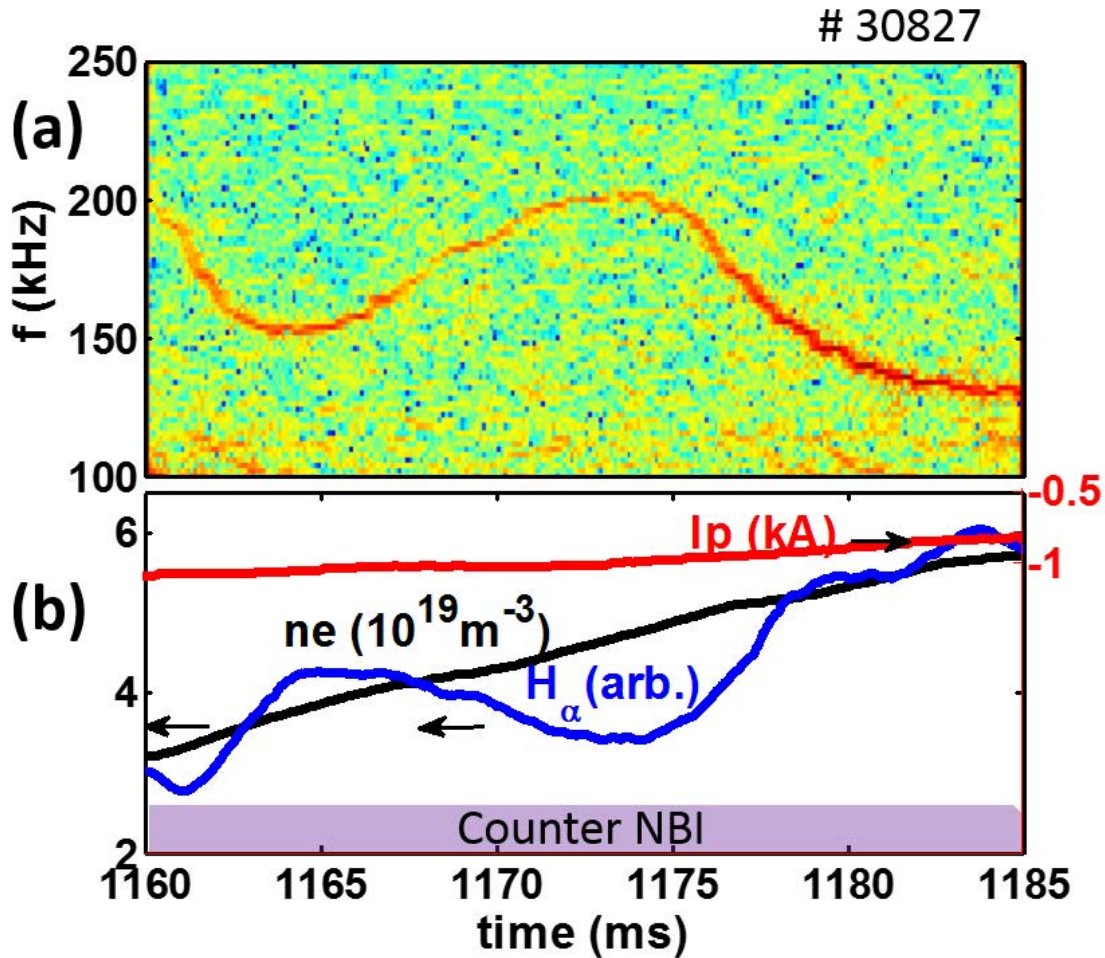


Figure 3.14 a) Spectrogram of a bolometry chord tangent to $\rho \approx 0.75$, b) H_α signal, c) line-averaged density and d) toroidal current for TJ-II discharge #30827.

cause the variation of Alfvén frequency. In this discharge, a MIAE is deduced base on the assumption that $\iota = 10/7$ island open a frequency gap for (1,1) coupling with (6,9) as shown figure 3.15a, approximately at $\rho = 0.65$ in spatial space, where locally the density undergo dramatical change due to impurity entering. Here we solve the inverse problem: assuming $\omega \propto 1/\sqrt{n_e}$ dependence for the mode frequency and constant atomic mass, the given time evolution of the frequency would be explained with the change in local density shown in figure 3.15b. It has been calculated choosing the radial location that corresponds to $\iota = 10/7$ (practically fixed because of the constant plasma current). While taking impurity contribution effect to the total mass density, the necessary condition for electron density variation should be reduced.

Conversely, in steady plasmas where the modification of the density profile is not dominant, the time evolution of the frequency of low-frequency AEs in TJ-II is basically due to

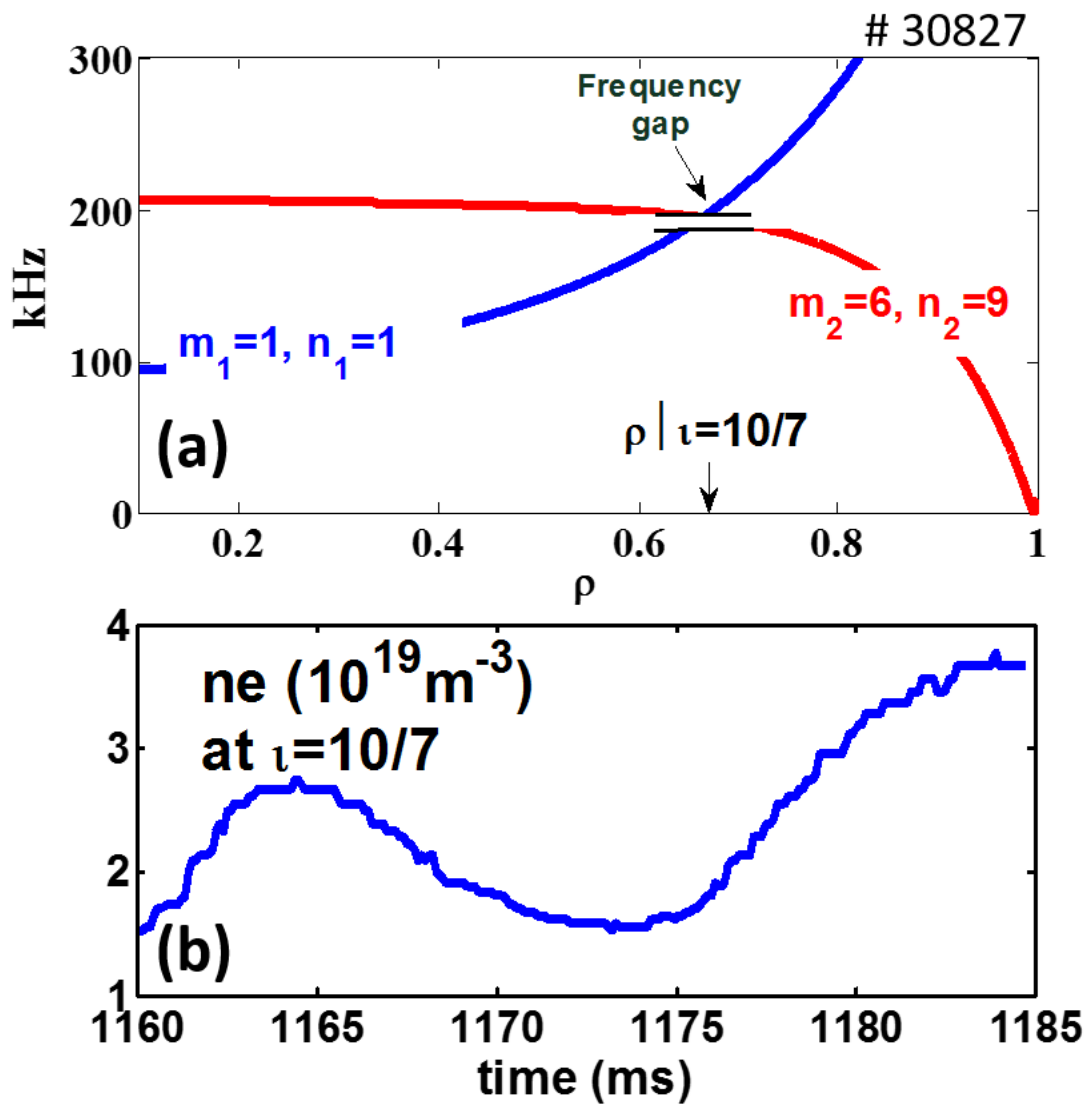


Figure 3.15 a) Alfvén continuum spectrum for two branches (1,1) and (6,9) crossing at $\tau = 10/7$, where MIAE may reside; b) evolution of the density at the fixed location $\rho_{10/7} = \rho(\tau = 10/7)$ that is needed to explain the frequency evolution in figure 3.14a.

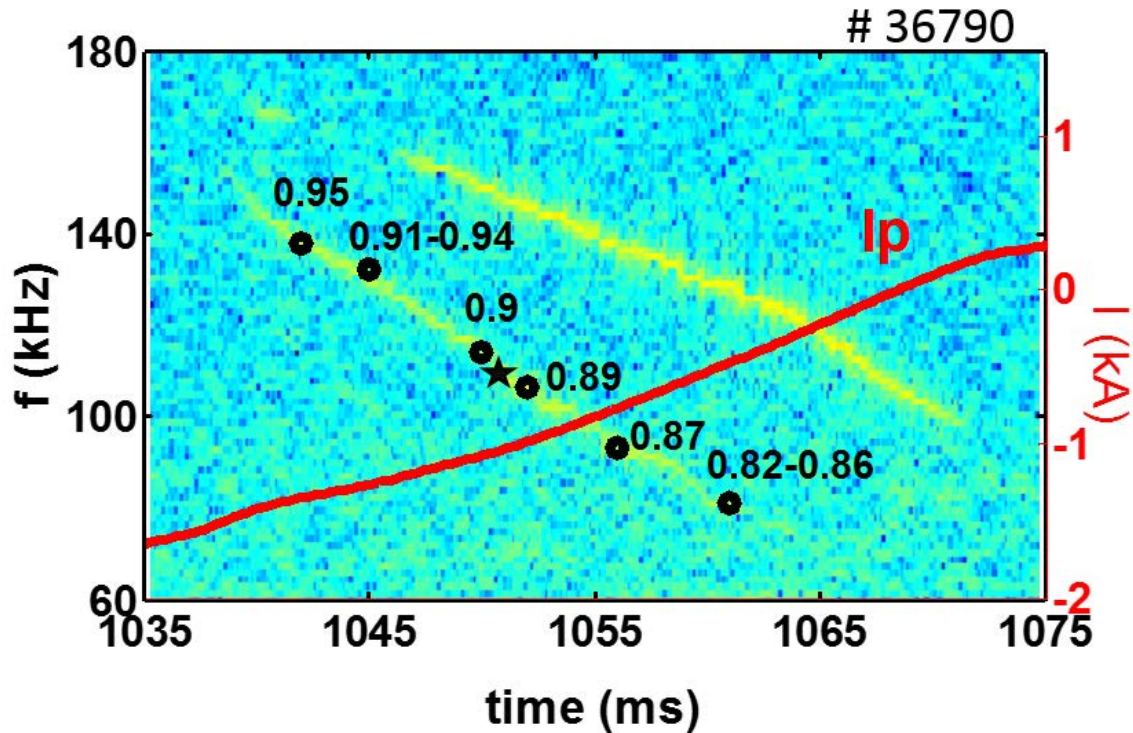


Figure 3.16 Spectrogram of a bolometer chord passing near the plasma edge detecting an Alfvén wave in TJ-II discharge #36790. The over plotted dots, labelled with radial positions, indicate the instants at which successive pins from a 12-pin electric probe stop detecting the mode. A star indicates the time at which a Mirnov coil stops detecting the same mode.

the movement of the resonant layers, via changes in $\iota(\rho)$, throughout the plasma. In low magnetic shear conditions, a small variation in net plasma current can shift ι_c to regions of quite different local density and the fits generally agree with the proposed models, GAE and MIAE. We can infer such movement from the intensity of bolometer arrays, as done in figure 3.6 for two different modes, or other diagnostics like in the following example.

In figure 3.16 we see the spectrogram of the signal coming from a bolometry chord passing near the plasma edge from NBI discharge #36790 during a time interval of continuously increasing I_p . This detector is sensitive to a large part of the plasma edge region ($\rho \geq 0.7$), thus being able to detect the mode from $t \approx 1035$ ms to $t \approx 1075$. In contrast, each of the 12 radially separated pins of an electric probe is sensitive to local perturbations only. The dots over-plotted on the mode represent the time instants at which the successive pins, whose positions in terms of effective radius of the nominal configuration are written, stop detecting it. Likewise, a Mirnov coil also stops detecting this mode at the time indicated by a star at $t \approx 1050$ ms although the bolometer still confirms its existence. The observations agree

with the evolution of the net plasma current, which must increase the near-edge rotational transform thus moving inwards in radius (towards larger densities) all resonant ι values in the zone.

The induction of ohmic currents changes the rotational transform profile at the expense of changing also the magnetic shear [82]. However, the TJ-II Helicac can also perform dynamic configuration scans where the rotational transform evolves during the discharge with little change in magnetic shear with respect to the vacuum values [79, 83]. Such scans brought up striking signatures of Alfvén waves due precisely to the movement of the gaps throughout the plasma. Part of that phenomenology was put together in a recent work [84] under the formulation for reverse-shear Alfvén eigenmodes, although the frequencies were fit based on fixed mode locations and line-averaged densities assuming single-mode contributions. In order to make a consistent interpretation of the data, we find that the mode gaps move, the densities should be local and, finally, single modes (as GAEs) cannot explain many other modes. However, and given the singularity of dynamic configuration discharges, it is in order making a rough prediction of the evolution of coherent mode frequencies we would expect to find in one such scans. To simplify matters, we have taken a fixed density profile (from TJ-II discharge #28174 at $t = 1160$ ms, similar to the case in figure 3.1) and the evolution of the vacuum ι -profiles as they would correspond to an ideal configuration scan, even though in the real scans both, electron and plasma current densities, evolve. Such prediction is made in figure 3.17 corresponding to dynamic scans where, respectively, magnetic resonances $M = 3, N = 5$ and $M = 2, N = 3$ are moved inwards, i.e., they enter the plasma through the edge and disappear in the centre after completely sweeping the plasma. Black lines are GAE frequencies falling with increasing edge ι , and colour lines are MIAE frequencies that are also decreasing. We can observe that GAEs change frequency quite linearly, almost in proportion to the edge rotational transform. On the other hand, MIAE frequencies go down in parallel with nearby GAE modes until, at some point, they approach the GAE branch and stop once they touch it. The crossing point depends on the mode, but it is generally found around 100 kHz. In the first scan, figure 3.17a, the main resonance $\iota = 5/3$ traverses the plasma and four main rational values play the dominate role, $\iota = 8/5, 5/3, 10/6$, and $7/4$. In figure 3.17b, the configuration scan makes $\iota = 3/2$ cross the plasma. Since this is a very low order rational value, there are less few low-order rational numbers nearby and we expect less populated spectrograms as the figure suggests. In this case, the main contributions are due to the rationals $11/7$ and $8/5$.

The evolution of mode frequencies in real plasmas is affected by –at least– variations in the density and rotational transform profiles. It is still interesting to make a qualitative comparison with the model case. The two spectrograms in figure 3.18 correspond respectively

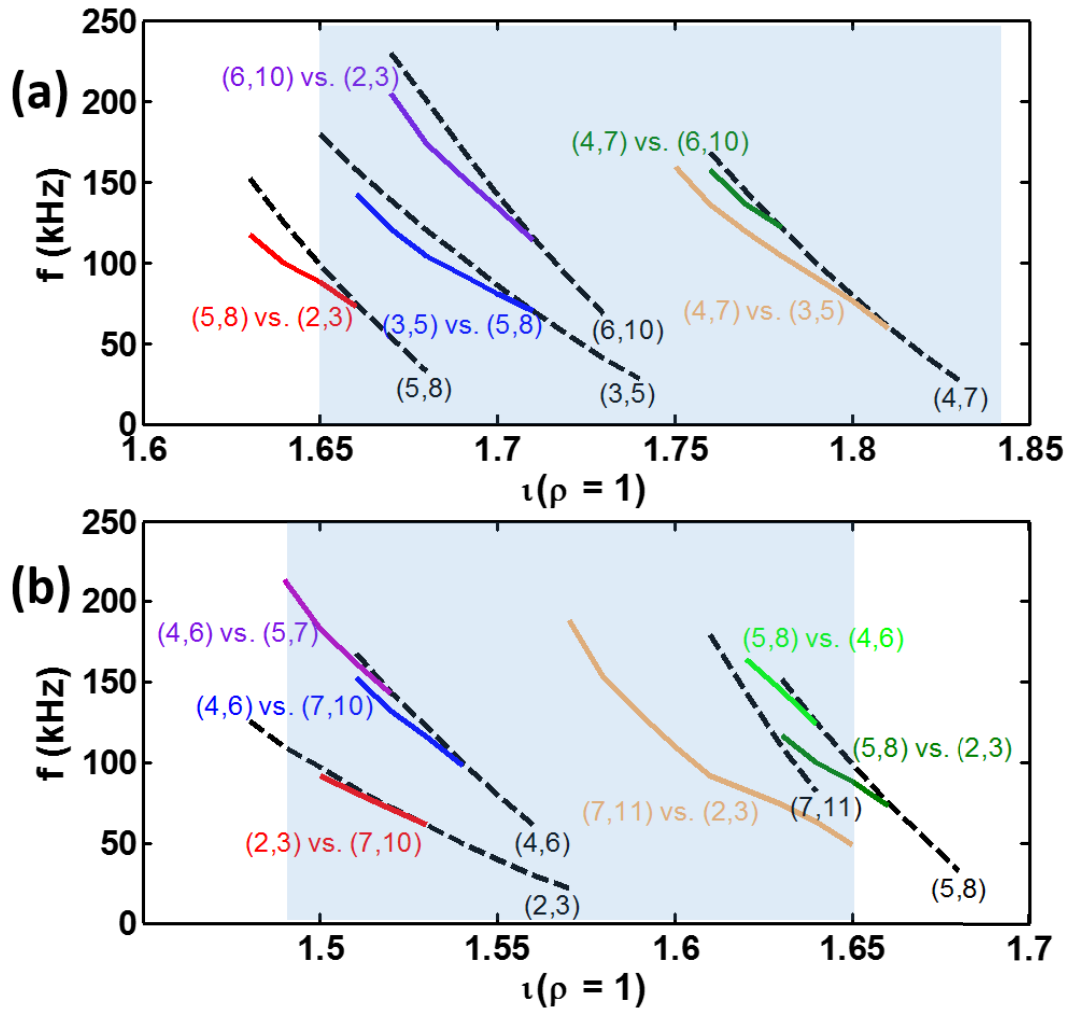


Figure 3.17 Evolution of GAE and MIAE frequencies with edge ι in an ideal magnetic configuration scans where $\iota(\rho)$, with a profile shape like the standard configuration 100_44_64, is shifted up at constant electron density profile (taken from TJ-II #28174 at $\bar{n}_e = \times 10^{19} \text{ m}^{-3}$). GAE modes are indicated with dashed lines and single mode numbers. MIAEs are indicated with solid colour lines and couples of mode numbers. a) 5/3 Sweeping, b) 3/2 sweeping (see text). The shaded areas are in correspondence with figure 3.18.

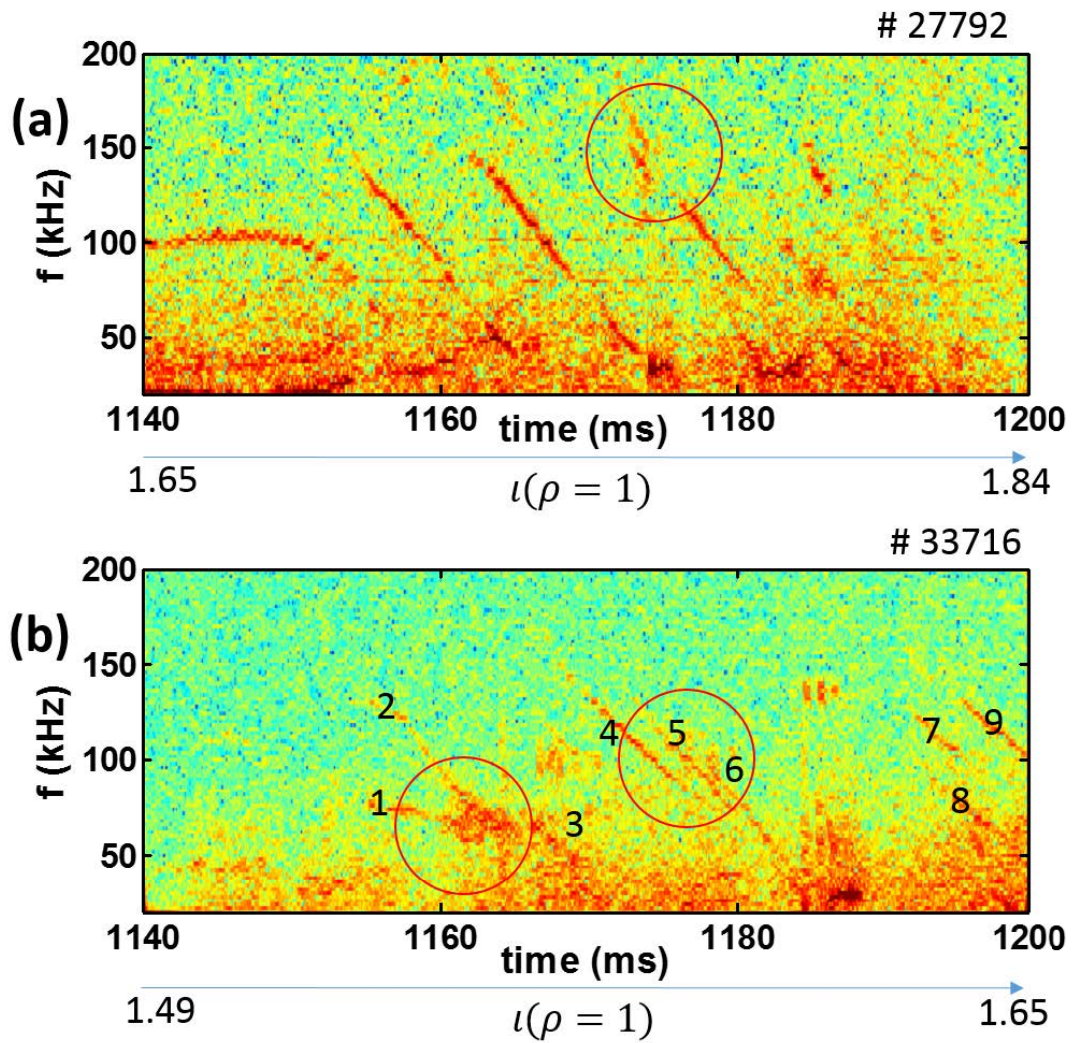


Figure 3.18 Spectrograms of bolometry chords in TJ-II magnetic configuration scans where ι_a increases in time covering the shading area in the respective figures 3.17. a) discharge #27792 sweeping the 5/3 resonance throughout the plasma, b) discharge #33716 sweeping the 3/2 resonance.

to the model spectrograms in figure 3.17: both are dynamic configuration scans in co-injected NBI plasmas at average densities around $\bar{n}_e = 1.5 \times 10^{19} \text{ m}^{-3}$ where either the $\iota = 5/3$ (a) or the $\iota = 3/2$ (b) resonance is swept all over the plasma from edge to core. The edge rotational transform covers approximately the shaded areas in figures 3.17a and 3.17b. We find that the $5/3$ sweeping is more populated than the $3/2$ one in terms of coherent modes and, in both cases, nearby modes seem to appear, as indicated by circles, especially in the $3/2$ sweeping case. Qualitatively speaking, the behaviour and range of the mode frequencies are as expected from the model. Note that, as it happened with previous examples, some of the modes could be explained as GAEs, but dynamic configuration scans show more modes that would be difficult to explain without considering MIAEs.

In order to finish the discussion of TJ-II phenomenology we turn back to figure 3.1 considering it again as a representative in TJ-II plasmas. Now all features that resisted a consistent interpretation seem logical just with the addition of the MIAE frequency gaps: the changes of frequency often respond to the changes in plasma current mainly due to the localisation of the gaps not far from the edge. In some cases there may be a doubt about the nature of some of the Alfvén modes because they could be related with different types, like in the particular discharge #28158 used for figure 3.1, where either a maximum of the $(n = 5, m = 3)$ branch or the MIAE above $\iota = 13/8$ in figure 3.2 might explain mode #3. But, generally speaking, many modes are as hard to justify as mode #2 unless the MIAE phenomenon is allowed. Some aspects of the phenomenology, like the exchange of intensities with rotation modes and the behaviour in magnetic configuration scans have been very useful to probe the hypothesis of the MIAE. Other aspects require further work, like the relation between off-axis sawteeth and the jump between branches (similarly to figure 3.5) or, in general, all aspects related with the coupling between island rotation and Alfvén modes.

In forthcoming AE studies, the consideration of helicities added to the magnetic field from magnetic islands should help to confirm or reject the results here reported. Cases have been documented where edge Alfvén waves are separated by low frequencies as they may come from tearing mode activity, like in ASDEX-U plasmas [85]. Such coupling between low-mode numbers and Alfvén waves of different nature has been documented in FTU [74] (beta-induced Alfvén eigenmodes) and HL-2A (TAE modes) [73], and an explicit case of three-wave coupling involving low mode number energetic particle modes and TAEs has been reported in NSTX [86]. Reversed magnetic shear experiments in the LHD have shown the non-linear interaction between reverse shear AEs and geodesic acoustic modes [87]. Generally speaking, mode-coupling phenomena should not be rare either in stellarator/heliotron devices, and magnetic islands may provide another way of coupling, especially in devices with low magnetic shear configurations. After a revision of the literature

it seems that many detected modes have not been classified in such devices as the W7-AS (see, for instance, [88] and figure 103 in [89]) and the Heliotron-J [90, 91]. Not claiming that unidentified modes must be of MIAE type, we encourage investigations that consider this possibility. MIAEs and couplings with rotating islands should eventually appear during the operation of the high- ι (~ 1) and low magnetic shear Wendelstein 7-X stellarator, where bootstrap currents and the operation with an island divertor can force the appearance of islands with poloidal mode numbers 5–12 inside the plasma [92]. In addition, if the mechanisms of wave-wave coupling here proposed are confirmed, they might provide a way to act on fast ion losses and, in particular, the MIAE might be used with diagnostic purposes much in the way it is done with reverse shear AEs in tokamaks. MIAEs should locate where magnetic islands do and, additionally, they should disappear if the island chain starts rotating.

Chapter 4

Acoustic mode driven by fast electrons in ECR plasma

Intense harmonic oscillations in radiation signals ($\delta I/I \sim 5\%$) are commonly observed during ECR heating in TJ-II stellarator plasmas at low line-averaged electron density, $0.15 < \bar{n}_e < 0.6 \times 10^{19} \text{ m}^{-3}$. Their nature is mostly electrostatic since they are rarely detected with Mirnov coils, ECE or soft X-ray detectors. The fundamental mode frequency agrees with acoustic modes and scales with acoustic speed. Their fundamental mode number is ($m=2$, $n=1$). They exhibit standing-wave like behaviour in the poloidal plane, as geodesic acoustic modes (GAM), but propagate at approximately the ion sound speed in the toroidal direction, as ion sound waves (ISW). The modes are found in the proximity of low order rational values of the rotational transform ($t = 1/q = 8/5$ and $5/3$) and are excited by fast electron populations. At line-averaged densities above the known critical $\bar{n}_e \approx 0.65 \times 10^{19} \text{ m}^{-3}$ for the confinement transition in ECR plasmas, the mode disappears in coincidence with the onset of island unlocking in the periphery.

4.1 Introduction

The Geodesic Acoustic Mode (GAM) [93], which is a high frequency zonal flow, cannot be directly driven by pressure gradient because $n = 0$. Nonlinear theory has predicted it to be driven by turbulence and is expected to be edge localized [94], which is consistent with many experimental observations in tokamak plasmas [95–97]. However, GAMs can also be driven by EPs through velocity space, like the global GAM observed during ICR heating in JET [98]; or the EP-induced GAM (EGAM) found during NBI heating in DIII-D [99, 100], where the GAM extends to the core. Moreover, core localized GAMs also exist in Ohmic heated

plasma in T-10 [101] and HL-2A [102] at the onset of strong tearing modes. In fact, the modes were found in the vicinity of rational surfaces (mainly $q = 2$), which also coincides with earlier observations of GAMs near $q = 3$ in the edge of TEXT [103]. A fast-electron excitation mechanism is proposed in HL-2A [102], while the necessary condition of having islands is unclear. In the LHD [104], EGAMs due to fast NBI ions were identified, based on the agreement with theoretical expectations, like $n = 0$ and $m = 0$ modes for plasma potential fluctuations, and $m = 1$ for plasma density fluctuations at EGAM frequencies. On the whole, non-axisymmetric devices are rich in configurational parameters and can become a good benchmark for studies on general acoustic modes, e.g. [105].

As mentioned in previous chapters, the TJ-II Helic is a device well suited for magnetic configuration studies including the effects of low-order rational surfaces. In this device, a mostly electrostatic mode that causes intense radiation fluctuations has been observed during ECR heating. It is located in the plasma column but never beyond the location of a low order rational surface. In this chapter, we present a first characterization of some low frequency modes as acoustic and fast-electron driven. In what follows we give a quick overview of the phenomenon, then show frequency scalings and modal structure compatible with acoustic modes, and illustrate the relation with fast electrons.

4.2 Experimental setup and general features

Plasmas of interest here are started and maintained with ECR ($P_{in} \leq 600$ kW, 2 gyrotrons). Thousands of discharges produced under different magnetic configurations of the TJ-II operational space (i. e., $2.2 \geq \iota(0) \geq 1.2$), different wall conditions (all metal, metal/C, B and Li coating) and different gases have been examined, although the two magnetic configurations more used in this study are 100-42-63 and 100-44-64. These have only slightly different rotational transform limits in vacuum $1.53 \leq \iota(0) \leq 1.63$ and $1.55 \leq \iota(0) \leq 1.65$, therefore both contain the rational value $8/5$ near the periphery, at $\rho \approx 0.88$ and $\rho \approx 0.76$ respectively. In low density ($n_e \leq 0.55 \times 10^{19} \text{m}^{-3}$) ECR heated plasmas, the electron temperature is much higher than that of ions, typically 400 eV and 80 eV at $\rho \approx 0.5$.

In this kind of plasmas fast electrons are normally generated and found well confined close to low order rational ($\iota = N/M$) surfaces, at least near the plasma edge [106, 27]. It is also rather common to observe coherent or quasi-coherent modes detectable with heavy ion beam probes, Mirnov coils, ECE detectors, and bolometers [37]. However, it is often the case that neither Mirnov coils nor ECE diagnostics can detect them.

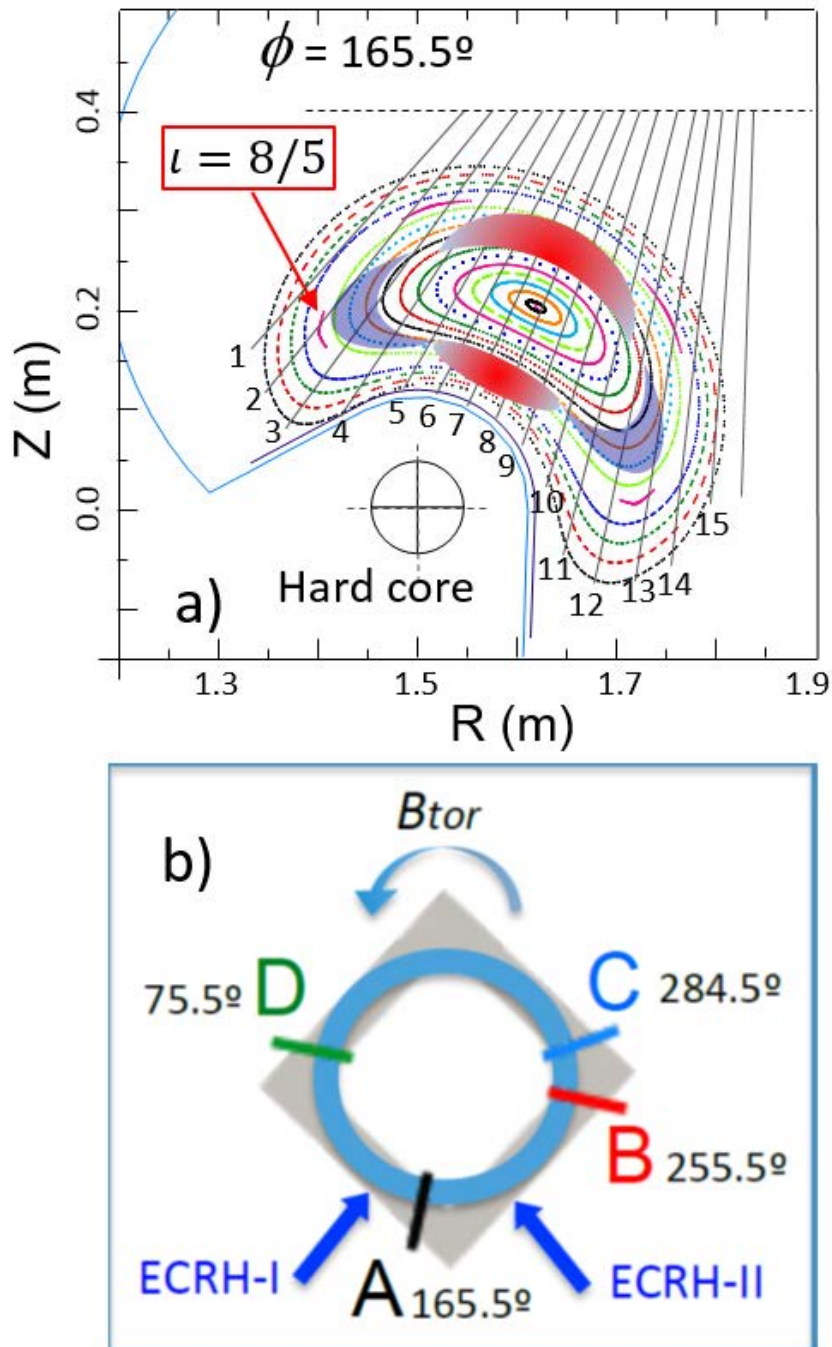


Figure 4.1 a) Scheme of a 16-channel photodiode array (A and D) on top of the Poincaré plot of one of the configurations used. A hypothetical $m = 2$ mode structure, characteristic of standing wave is overplotted (see text). The $\iota = 8/5$ region is indicated. b) toroidal layout of bolometer arrays in equivalent sectors D, A, and B, and stellarator symmetric C.

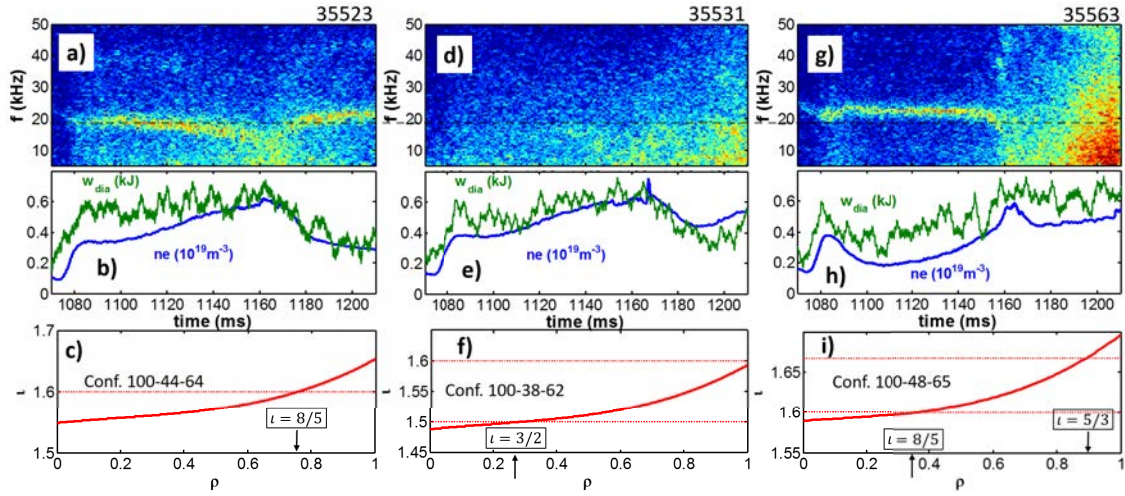


Figure 4.2 Mode excitation relying on magnetic configurations. Panels a)d)g) are power spectrograms of a bolometer viewing through $\rho \approx 0.5$; b)e)h) are time evolution of line averaged electron density and diamagnetic energy; c)f)i) the rotational transform profiles of each magnetic configuration in vacuum.

4.2.1 Configuration dependence: island in the periphery

We have compared discharges with different magnetic configurations and similar plasma parameters in order to clarify the relationship between mode appearance and the rational surfaces location in the plasma column. It is worthy to note that comparisons were made using configurations with very similar shape and volume in order to have an equivalent viewing geometry of the bolometer arrays. Comparing discharges #35523 and 35531 (left and center columns in figure 4.2), it can be appreciated that the mode around 20 kHz (figure 4.2a) shows up when $\iota = 8/5$ island is located around $\rho \approx 0.75$ (figure 4.2c), however no clear mode can be seen (in figure 4.2d) once $\iota = 8/5$ island is just moved out the plasma as seen from ι profile in figure 4.2f. In another discharge #35563 in which a new island $\iota = 5/3$ is placed in the periphery around $\rho = 0.90$, the mode appears around 22 kHz. The necessary condition of having an island in the periphery to excite the mode is rather robust; the mode frequency is generally independent of rational value, and the island position can be flexible (within $0.7 \leq \rho \leq 0.9$). Once it appears, the mode frequency is independent of island rational numbers, which rules out tearing mode or interchange mode where the frequencies should scale with the mode number. In addition, neither magnetic nor electron temperature fluctuation at that mode frequency is detected, thus indicating that the nature of the modes is different from those previous studied; i.e., it is neither tearing mode (Chapter 2), nor Alfvén wave (Chapter 3).

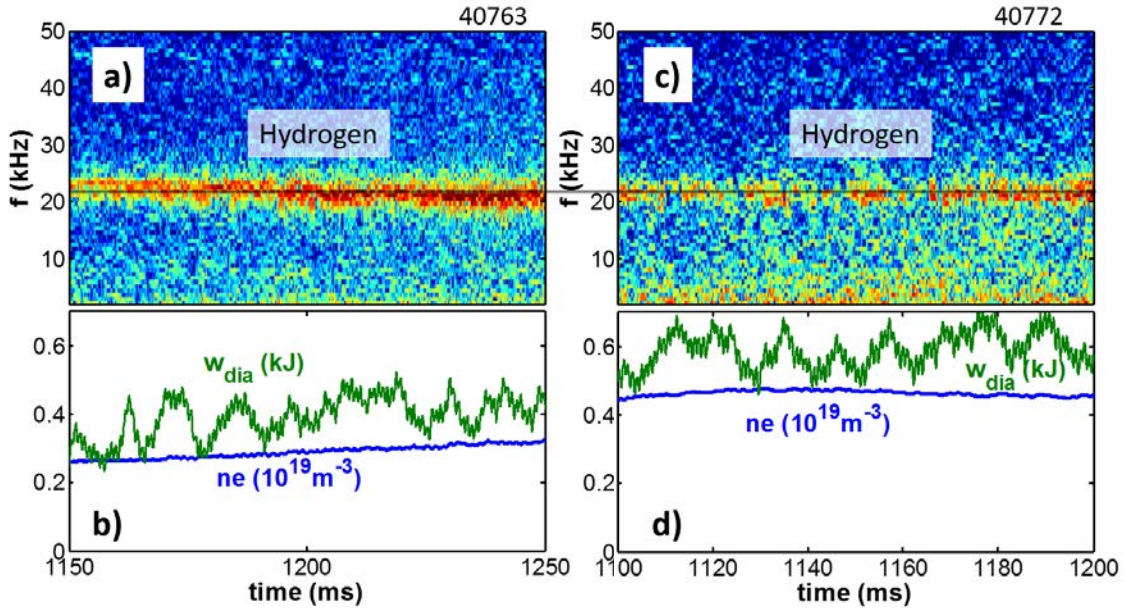


Figure 4.3 Mode frequency independence on density. a) c) power spectrograms of bolometer viewing at $\rho \approx 0.5$; b) d) line average density and diamagnetic energy time evolutions.

4.2.2 Density independence

Now, keeping fixed the magnetic configuration (100-44-64), we have compared discharges with different plasma parameters. Figure 4.3 shows the power spectra of radiation signals detected with a bolometer with impact parameter $\rho \approx 0.5$ and the line averaged electron density and the diamagnetic energy of two representative discharges #40763 and 40772. A mode around 20 kHz is observed, although the line average densities are significantly different, $n_e \approx 0.3 \times 10^{19} \text{ m}^{-3}$ and $n_e \approx 0.45 \times 10^{19} \text{ m}^{-3}$ respectively. This density independence further supports that the nature of the mode is not Alfvénic.

4.2.3 Mass to charge ratio and electron temperature dependence

Frequently in discharges with freshly lithium-coated walls, small lithium flakes can be detached and enter the plasma provoking rapid raises and drops of radiation signals. Figure 4.4 shows an example of an ECR heated deuterium discharge with magnetic configuration 100-44-64 and small negative current, in which these low Z impurities enter into the plasma repetitively (see caption). The rapid raises of radiation are mainly due to line radiation coming from excitations of Li^{+1} and Li^{+2} , from a slight decrease in electron temperature and from a small increment in the effective charge and electron density due to the ionisation of Li^{+1} and Li^{+2} . The effect on the fundamental mode and its harmonics can be seen in the

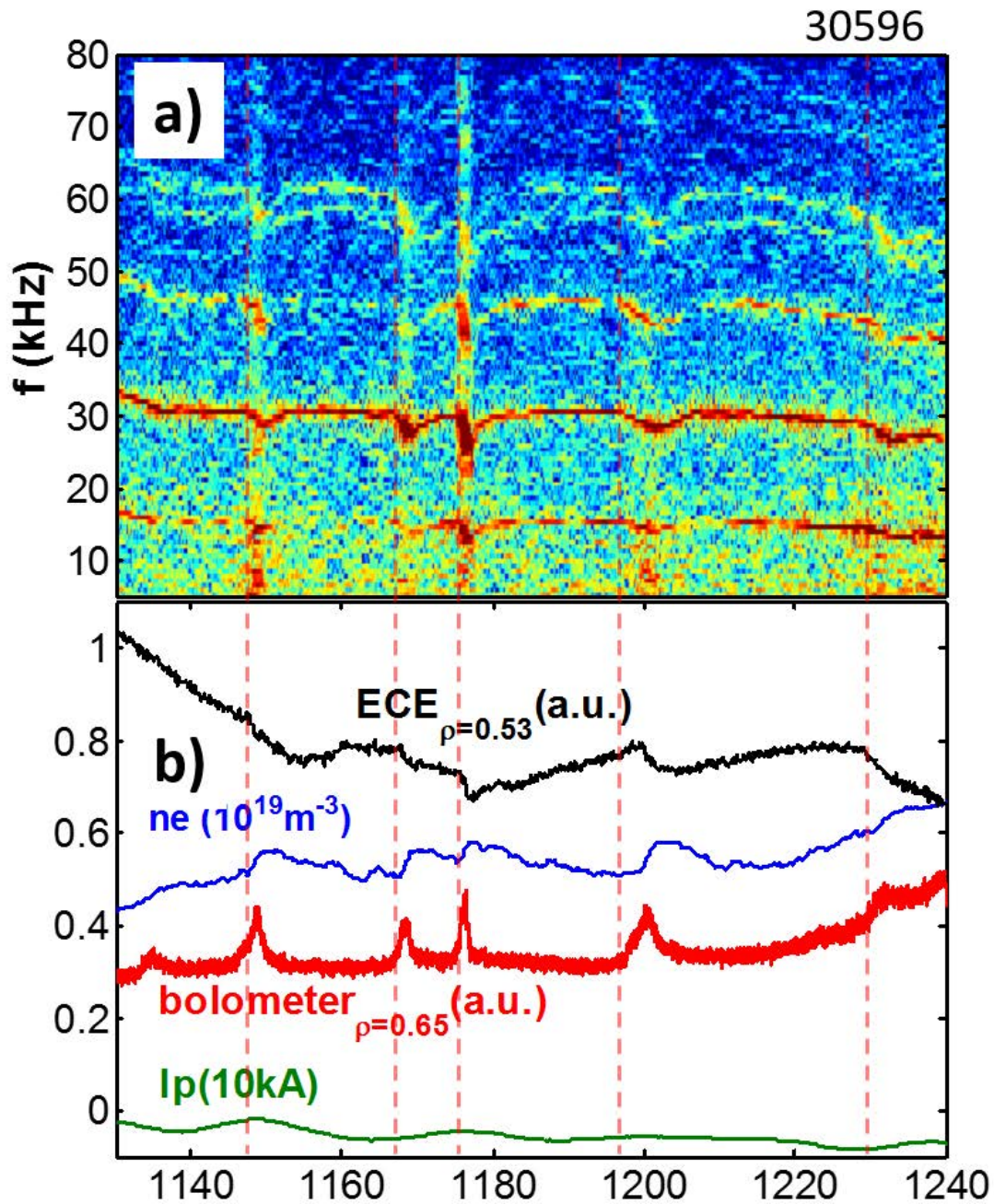


Figure 4.4 Discharge #30596 with lithium impurities entering the deuterium plasma repetitively during ECR heating. a) Power spectrogram of bolometer viewing in the center of plasma; b) plasma parameters time evolutions: electron temperature measured by ECE at $\rho = 0.53$, line averaged density, bolometer signal with impact parameter $\rho = 0.65$, and plasma current. Vertical lines indicate the moments when the second harmonic starts to drop the frequency.

spectrogram of a bolometer signal with impact parameter $\rho \approx 0$ represented in figure 4.4a. After each impurity entrance, the modes intensities notably increase and their frequencies drop and recover their previous levels, approximately. As it is shown, the time evolution of local electron temperature (and n_e) roughly follows that of modes frequency and radiation signal, but with a little delay (more evident as the plasma current becomes more negative). Then, other changing parameters at the plasma periphery must be modifying the modes frequency before electrons cool down. Taking into account that the mass to charge ratios of lithium ions with respect to deuterium ions are 3.5 for Li^{+1} and 1.75 for Li^{+2} , and that the ionisation potentials are 5.4 eV and 75.6 eV, respectively, one changing parameter is the effective ion mass. This observation and all the dependences above described, have led us to consider that these modes are likely of acoustic nature.

4.3 Identification of acoustic mode

Figure 4.5 shows a representative discharge (TJ-II #30588) to illustrate the main features of these modes. It is an ECR heated deuterium plasma with slowly increasing electron density up to $0.5 \times 10^{19} \text{ m}^{-3}$ until ECR heating switch-off (vertical dashed line). The time evolution of some global plasma parameters is shown in figures 4.5a and 4.5b (see caption). Ions are heated through collision with electrons and their temperature stays rather constant between 70–80 eV. The diamagnetic energy roughly increases with \bar{n}_e , H_α light intensity also linearly increases with density if there is no edge confinement change. Although **not shown**, the electron temperature deduced from central ECE channel is higher than the central electron temperature which is typically less than 1.2 keV, this mismatch is due to the fast electron contamination. The hard X-ray signal (HXR), which follows the fast electron losses with energies above 80 keV, rapidly goes up in the beginning of the discharge when fast electrons are generated (see super-high value from ECE(0) at the beginning), then decays slowly during the discharge.

Figure 4.5c shows the spectrogram of one bolometer signal with impact parameter $\rho = 0$. The frequency of the intense fundamental mode evolves from 22 to 16 kHz and is accompanied by two clearly defined harmonics. The mode appears once $\bar{n}_e > 0.2 \times 10^{19} \text{ m}^{-3}$ and keeps high intensity level in radiation fluctuations, although the frequency decreases with electron temperature as the density rises. The Fourier analysis of the Mirnov coil signal and ECE signals spectra have the same behaviour, they only shows the initial part of the first and second harmonics found by bolometry. Observe that the appearance of magnetic oscillation coincides with the sudden HXR signal drop (see figures 4.5b and 4.5e), which suggests that the magnetic component is generated due to a temporal change of fast electron distribution.

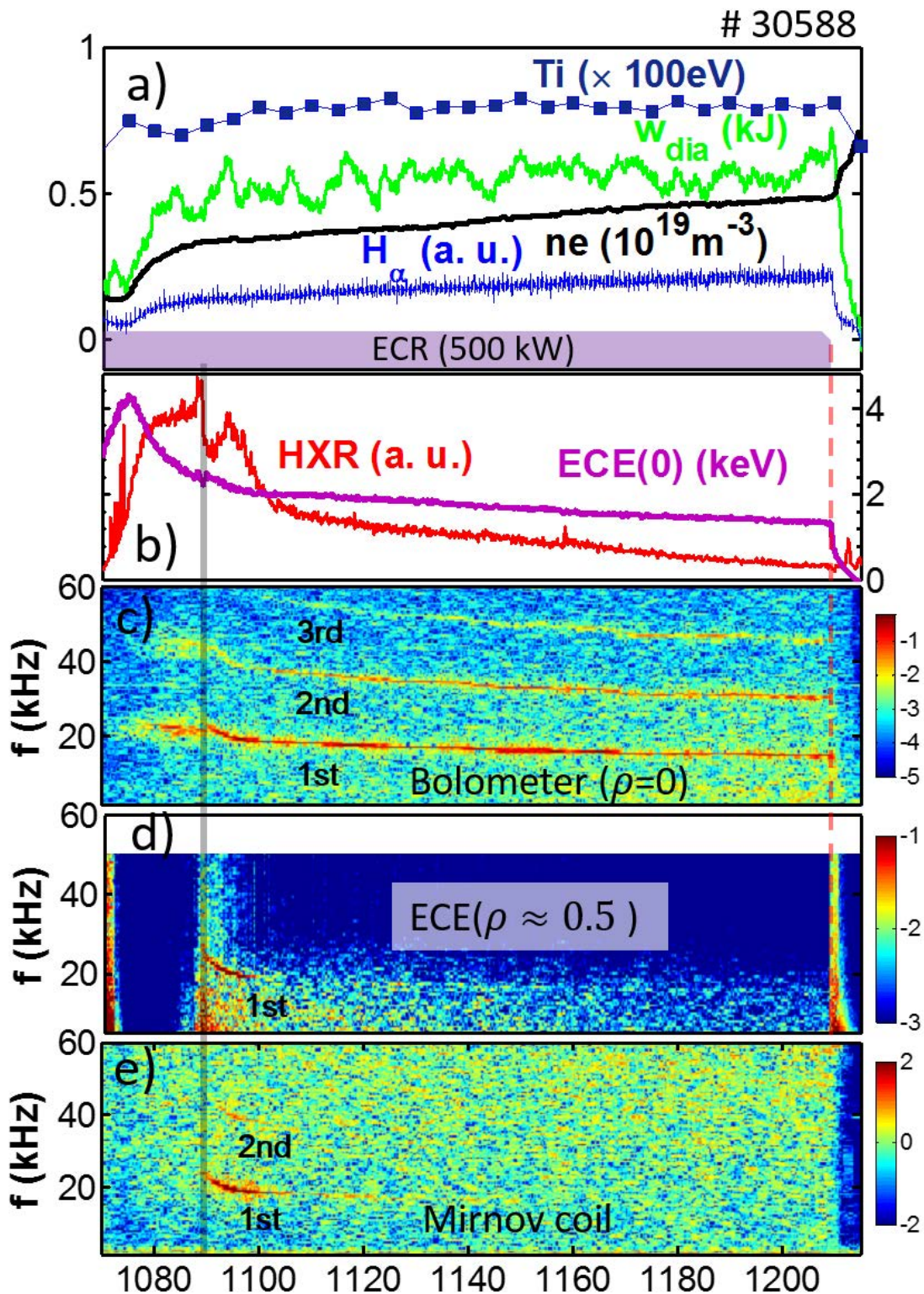


Figure 4.5 ECR heated deuterium discharge #30588. a)-b) Time traces of ion temperature, diamagnetic energy, line-density, H_{α} intensity, hard X-ray flux and central ECE signal; c) radiation signal spectrogram from a bolometer with impact parameter $\rho = 0$; d)e) spectrogram of ECE and Mirnov coil signal respectively.

The absence of electron temperature fluctuation (see figures 4.5d) and the fact that the modes change character from magnetic to electrostatic indicate that the intense radiation oscillations should come from density fluctuations. It must be noticed that neither Langmuir probes nor bolometers looking at the plasma edge can detect the electrostatic part of the modes. These facts would imply that the plasma is compressible, and suggest that the mode is core localized and, very possibly, acoustic. Two types of acoustic modes have been taken as possible candidates, GAM and ISW.

According to the formula in [107] the GAM frequency is:

$$f_{\text{GAM}} = \frac{\sqrt{2}}{2\pi R} \left[\frac{T_i}{m_i} \left(\frac{7}{4} + \frac{T_e}{T_i} \right) \right]^{0.5} = \frac{\sqrt{2}}{2\pi R} C_s, \quad (4.1)$$

while the ion sound wave frequency is given by

$$f_{\text{ISW}} = \frac{n}{2\pi R} C_s. \quad (4.2)$$

Here n is toroidal mode number and the ion sound speed is taken as

$$C_s = \sqrt{\frac{T_i}{m_i} \left(\frac{7}{4} + \frac{T_e}{T_i} \right)}. \quad (4.3)$$

This value is calculated using electron temperature from Thomson scattering data, typical 80 eV for T_i and 1.2 times the deuterium mass as effective ion mass m_i . The fundamental GAM and ISW frequencies are plotted versus ion sound speed C_s (evaluated at $\rho = 0.5$) in figure 4.6a for a series of discharges in the same magnetic configuration under the same ECR heating. The observed frequencies are compatible with the acoustic frequency range, below that of GAM but close to ISW. An apparently negative linear correlation between mode frequency and \bar{n}_e is noticed in figure 4.6b, which responds to the decrease of electron temperature with increasing density in these plasmas. In figure 4.6c we estimate the radial profile of the GAM (continuous line) and ISW (dashed line) frequencies evaluated for discharge #30588 (figure 4.5) at $t = 1180$ ms. In the background we join the spectra obtained from bolometer chords at different impact parameters. Since the used signals are line-integrals, only chords with $\rho \geq 0.3$ are shown. Here the fluctuation level reaches (see colour bar) $\approx 3\%$, although larger values are seen in other time instants (see fig. 4.5c). Again, the frequency is clearly below that of GAM, but intersects ISW frequency at around $\rho \approx 0.6$, which is also the range where the bolometers observe the most intense oscillation (see color bar). The mode is only detectable up to $\rho \approx 0.7$, just inside the rational $\iota = 8/5$ location.

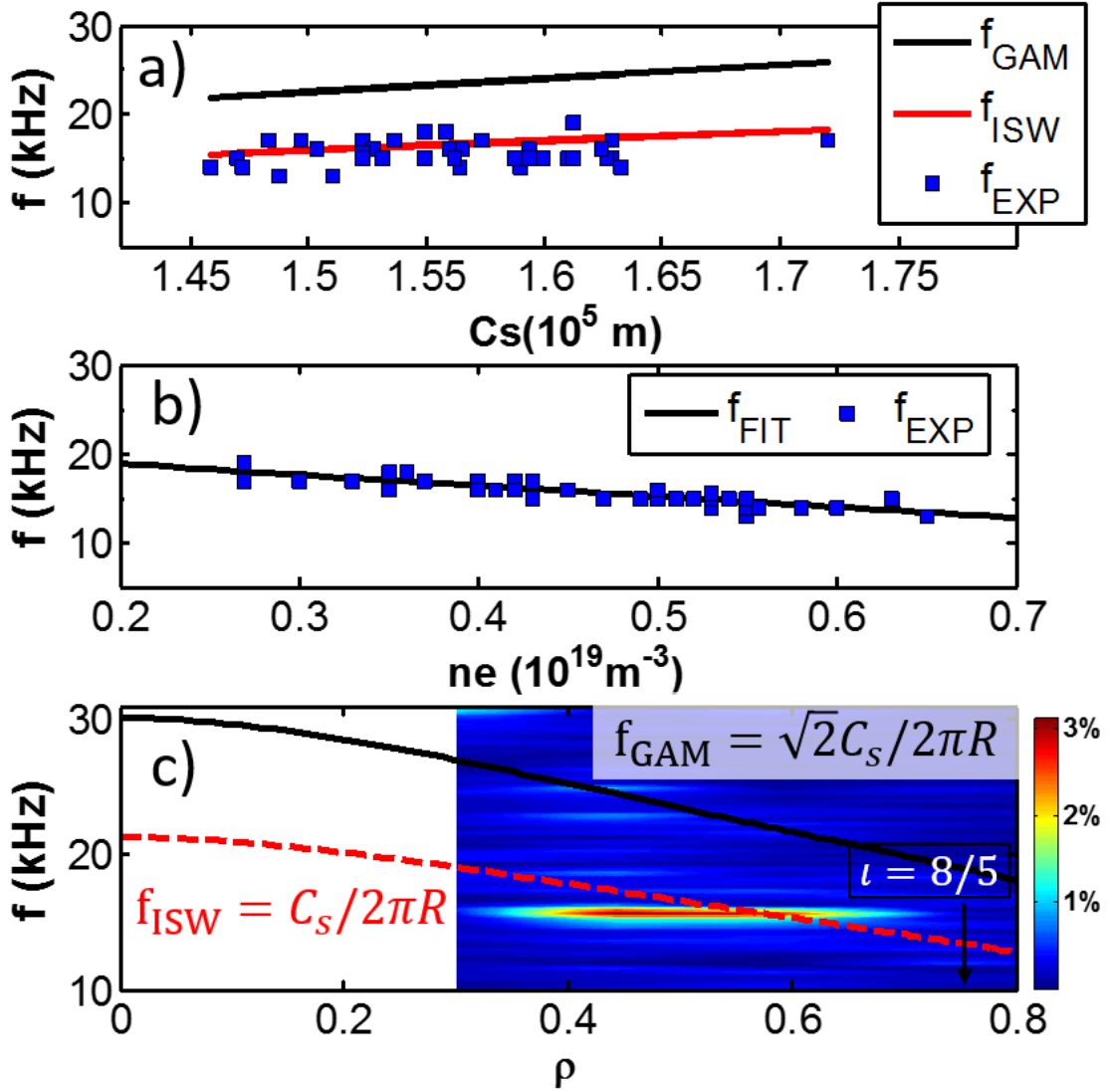


Figure 4.6 a) GAM and ISW frequencies at $\rho = 0.5$ estimated from equations (4.1) and (4.2) (lines), and experimental data (dots). b) Observed frequency versus \bar{n}_e and linear fit. c) Radial profiles $f_{\text{GAM}}(\rho)$ and $f_{\text{ISW}}(\rho)$ for discharge #30588 at Thomson scattering time, and spectra of bolometer chords versus impact parameter (see $\delta I/I$ percentage in colour bar). The approximate location of the $\iota = 8/5$ rational surface is indicated. $n = 1$ is used in Eq. (4.2).

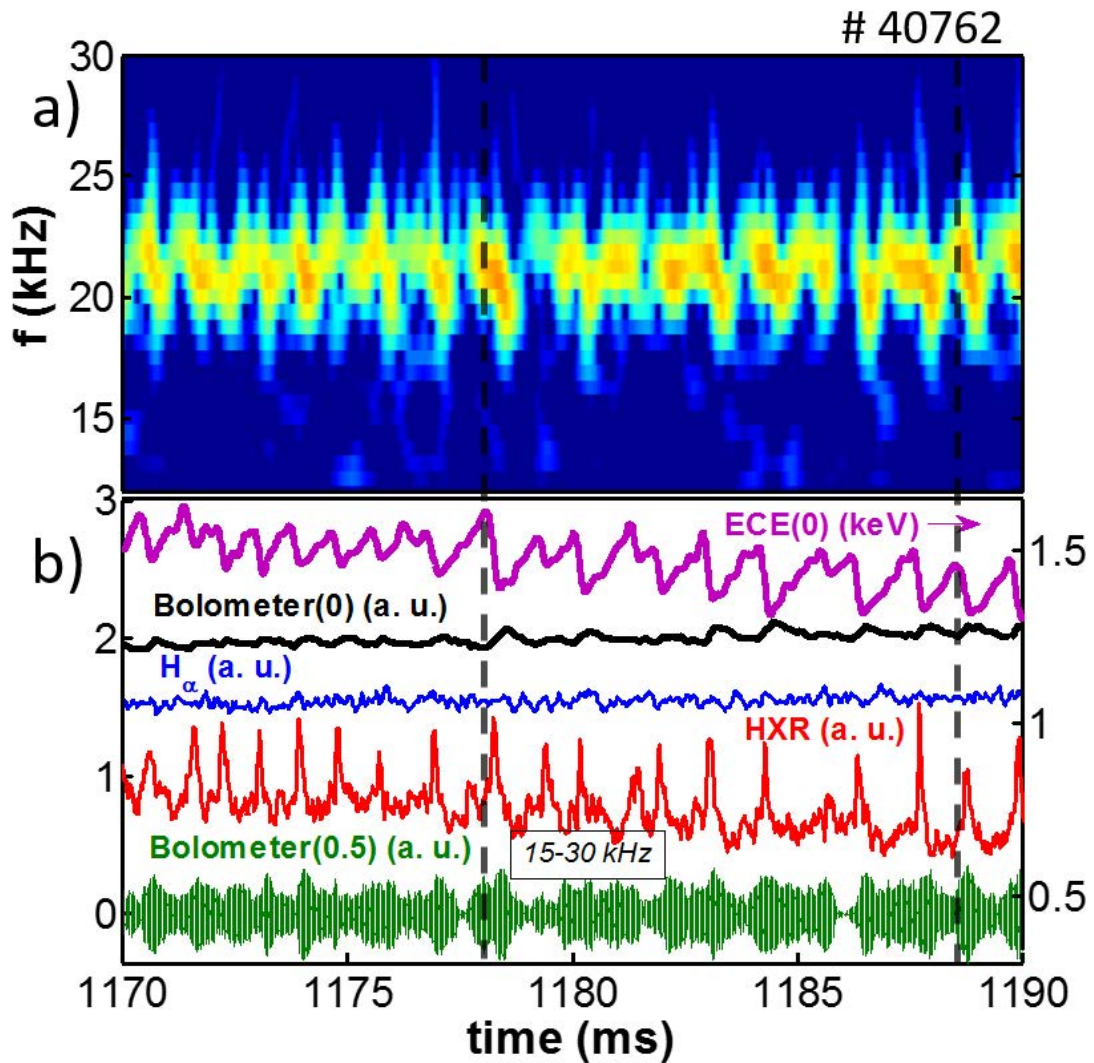


Figure 4.7 Discharge # 40762. a) power of wavelet spectrogram of bolometer chord with $\rho = 0.5$; (b) time evolution of central ECE, HXR and the radiation oscillation due to the mode.

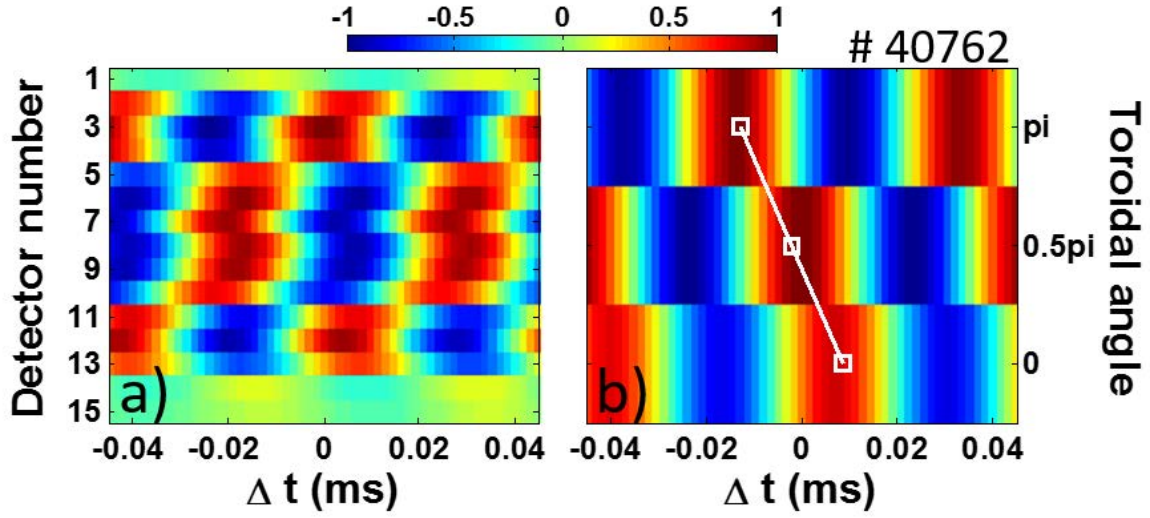


Figure 4.8 Discharge # 40762. Correlation of bolometer array signals (see diagnostic layout in figure 4.1) with the reference channel 8 ($\rho = 0$), in the frequency range of the acoustic mode shown in figure 4.7a. a) poloidal and b) toroidal correlation (see text). The time interval used is 1180–1185 ms. White line in b) indicates the toroidal propagation by following the maximum correlation. The fitted slope is $d\phi/dt = -145.6$ rad/ms.

The relationship between acoustic modes and fast electrons is evidenced in figure 4.7. There, it can be seen how HXR-signal pulses are strongly correlated with the frequency chirping down (about 5 kHz) of the mode detected at $\rho = 0.5$. Although no T_e fluctuations are detected at the mode frequency, the time evolution of the ECE(0) signal is sawtoothing, in coincidence with the spiky HXR signal. It is worthy to mention that no phase inversion is found in the T_e profile, the H_α signal does not show pulsed response and, as expected, the central radiation signal shows the opposite time evolution than that of the ECE(0). This means that the central temperature collapse is not due to thermal plasma. The upper frequency value of the observed mode, $f = 25$ kHz, matches the acoustic scaling showed in figure 4.6b for a hydrogen plasma, with $T_e(\rho = 0.5) = 490$ eV, $T_i = 80$ eV, and $m_i = 1.2m_p$.

4.4 Acoustic mode structure and its harmonics

Correlation bolometry has been applied to reveal the acoustic mode structure as shown in figures 4.8a and 4.8b. In the poloidal plane no global propagation trend is visible. Instead, only two abrupt changes of the correlation sign take place, between channels 10 and 11 and between 4 and 5, separating a wide central region with a rather constant phase. This pattern is compatible with a $m = 2$ standing-wave behaviour, like the structure represented in figure

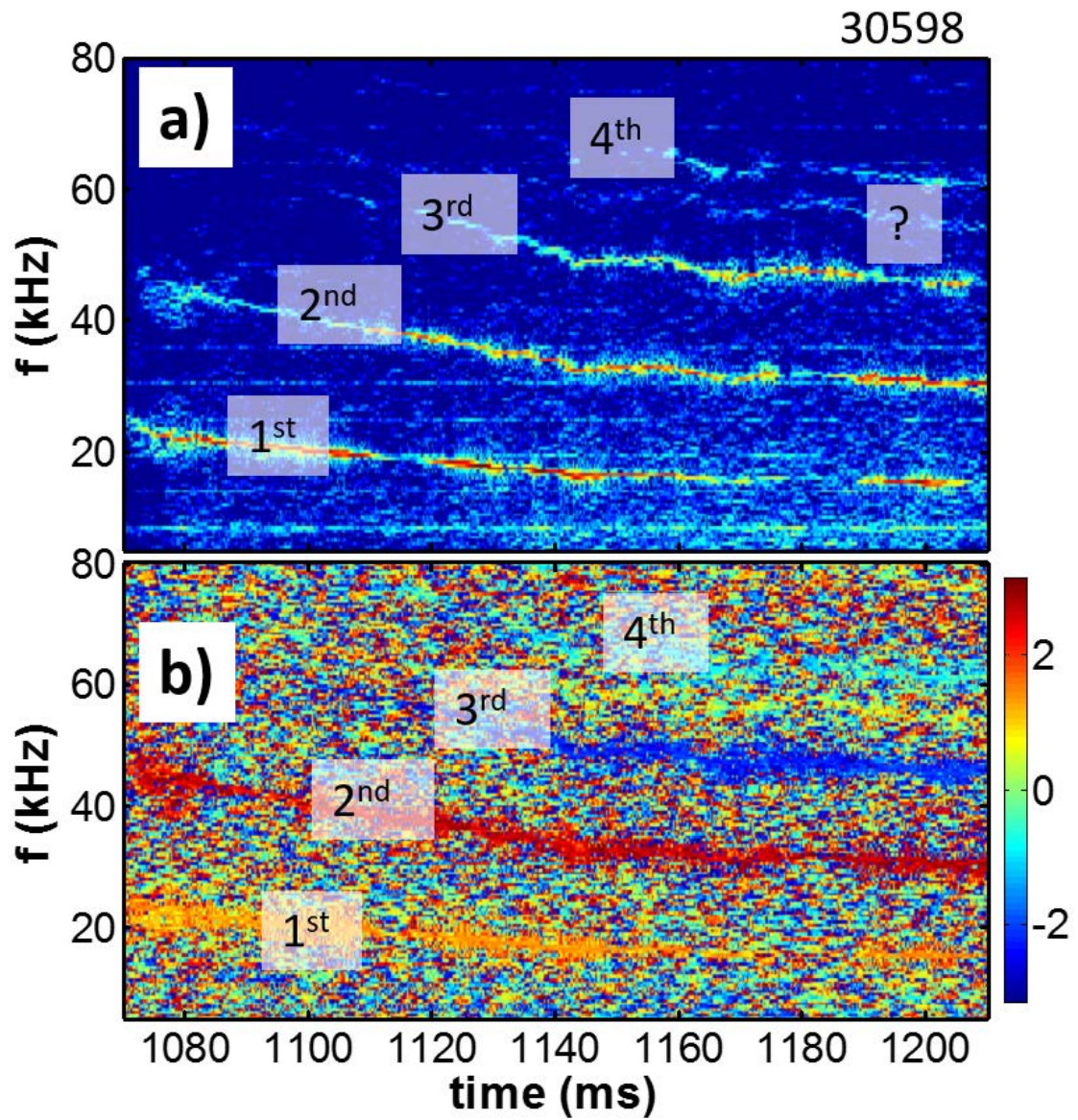


Figure 4.9 Discharge #30598. a) Power spectrogram of bolometer in sector A; b) phase spectrogram of two bolometers viewing at the same poloidal angle but separated $\pi/2$ toroidally.

4.1. As in the previous example the mode does not extend beyond $\rho = 0.7$. In fact, there is a sharp decrease of radial correlation (for a radial separation of only 1.8 cm) when comparing #2 ($\rho = 0.65$) with #14 ($\rho = 0.74$). For this magnetic configuration this takes place in the vicinity of the rational 8/5.

Figure 4.8b shows the correlation of three equivalent bolometer signals ($\rho = 0.5$) separated toroidally by $\pi/2$ (see figure 4.1b). The pattern exhibits a pure propagation behaviour in the negative direction, that is, counter the toroidal magnetic field direction. The linear fitting gives an estimation of the mode number $n = \omega / (d\phi/dt) = -2\pi \times 22 / 145.6 = -0.95 \approx -1$.

Harmonics of the modes are more commonly seen in deuterium rather than hydrogen discharges. As shown in figure 4.9 for deuterium plasma, up to 4 harmonics are visible. However the modes are not necessarily continuous, and their intensities can be slightly changing. Notice that the first harmonic does not always appear as the most intense one. In fact, the second harmonic can be more intense than the first one, that in occasions becomes weak or even disappears. Even the third harmonic in figure 4.9a around $t = 1180$ ms can reach the highest amplitude, whilst the first and the second are almost mute.

The toroidal cross phase spectrum is plotted in figure 4.9b using two bolometers looking at the same poloidal plane but separated toroidally by a quarter of the device. For each harmonic, the phase doesn't change throughout the whole discharge, which means that the toroidal structure is well established and kept although the plasma is evolving. For different harmonics, the phases vary: for the first harmonic, the phase shifting is around 1.5 radians corresponding to a mode number $n = 1$; for the second harmonic, the phase shifting is around 3, which is about twice of the first one, then indicating that the second one has mode number $n = 2$; for the third one, the phase is about -1.5, which can be interpreted as $2\pi - 1.5 = 4.8$, matching the expected mode number $n = 3$; for the fourth harmonic, the phase is about -0.5, which is close to zero, and according to the fact that two bolometers are separated by a quarter, near zero phase shifting is indicating that the mode number is 4. Modes that show harmonics in both, frequency and mode number, are consistent with the basic assumption of ISW as in Eq. (4.2). However, for the poloidal structure, it is much harder to judge the poloidal mode number because the bolometer signals are line integrals. We have estimated that the first harmonic is an $m = 2$ standing like structure in the poloidal plane, where density fluctuation shows up and down symmetry with respect to the middle plane. The observed mode $m = 2$ may be due to high plasma shaping effect in TJ-II configuration, but further investigation is needed. Harmonics are barely reported for the GAM driven by turbulence in the plasma edge; however for EGAM, second and even higher harmonics are measured to be intense [108]. Nonlinear MHD theory has predicted the existence of a second harmonic in density fluctuation but not in electric field. However, when nonlinear mechanisms of the

fast particle population are taken into account, second harmonics of both density and electric field are resolved [109].

4.5 Density limit for acoustic mode in relation to island unlocking

In figure 4.10a we show time traces from discharge #35503, operated with deuterium, which is a kind of discharge commonly used in the TJ-II to study the low density ($\approx 0.65 \times 10^{19} \text{ m}^{-3}$) confinement transition [110, 80]. During the initial density ramp-up phase, the acoustic mode is observed. The fundamental mode frequency decrease follows the decrease of the electron temperature in figure 4.10b. The mode coherency and intensity increase as the density increases, until the critical value is reached. A few milliseconds later (see vertical grey line on the left) the density reaches $\approx 0.73 \times 10^{19} \text{ m}^{-3}$, slightly above the critical value. Then the acoustic mode disappears and is replaced by another mode. According to figures 4.10c and 4.10d, it must have a different nature. In fact, the mode frequency increases with density and is detected by Mirnov coils and peripheral bolometers. This is the consequence of island rotation following the $E \times B$ flow [79, 111]. In particular, a magnetic mode associated to the 8/5 helicity rotating at a speed compatible with the $E \times B$ drift velocity is identified for equivalent discharges [80]. The momentum of plasma flow increases with density and, at some threshold value, islands (say 8/5) can be unlocked. In the present case, the magnetic mode is detected at an initial frequency of 10 kHz, which would correspond to $E \times B$ drift velocity of about 2 km/s. The tearing mode keeps increasing its frequency until the density reaches its maximum value. During the density ramp-down phase the situation reverses: the tearing mode brakes, the islands get locked and the acoustic mode is recovered.

The study of correlation of modes using the bolometer array signals (see figure 4.1) in the poloidal plane is revealed in figure 4.11. An acoustic mode structure is visible in figures 4.11a and 4.11c, which is similar to the one in figure 4.8. Obviously it is a $m = 2$ standing wave behaviour, although there seems to be a continuous propagation from channel #6 to #4. This could be due to the drawback of line integral diagnostic; however, a sharp change of correlation sign is clearly seen between channels #10 and #11. The feature of core localization is also present: the correlations are absent between core and edge viewing bolometer signals such as channels #14 ($\rho = 0.74$), #1 ($\rho = 0.82$) and #15 ($\rho = 0.92$), and the values are rather weak for less peripheral channels #2 ($\rho = 0.65$) and #13 ($\rho = 0.58$). Figure 4.11b gives the correlation structure of the tearing mode that corresponds to rational $\iota = 8/5$ existing at $\rho = 0.85$. The correlation values are high throughout all the channels and

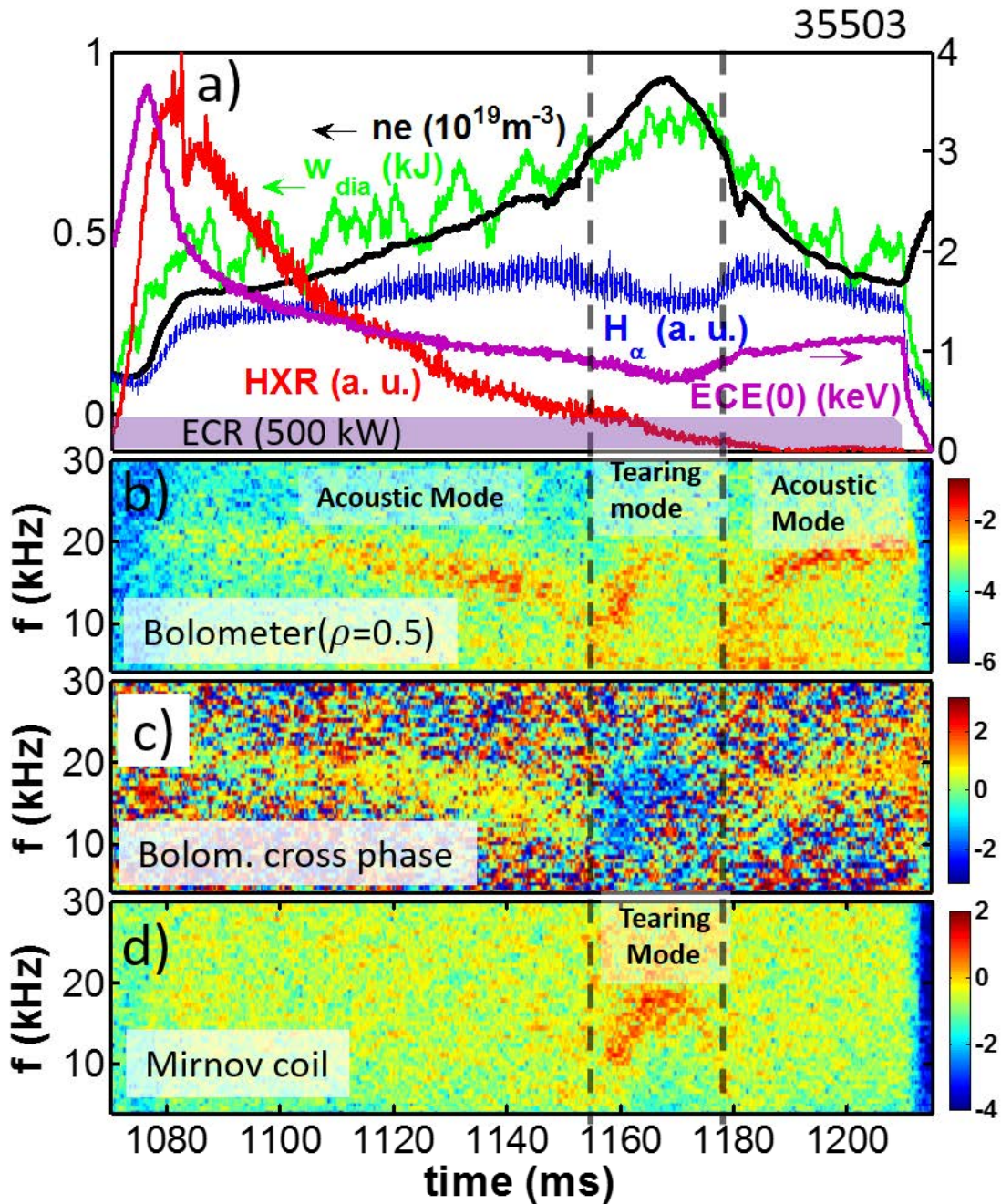


Figure 4.10 Discharge #35503. a) Time traces of \bar{n}_e , diamagnetic energy, H_{α} , hard X-rays and central ECE signal; b-c) cross-power and cross-phase spectrogram between two bolometer chords with the same impact parameter $\rho \approx 0.5$ but different viewing angle; d) cross-power spectrogram of two Mirnov coils.

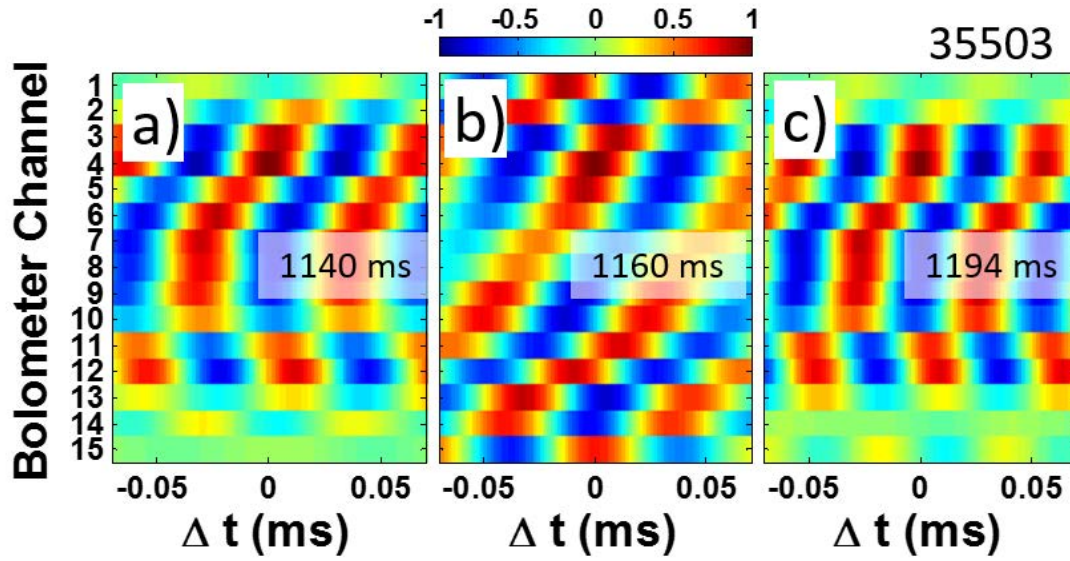


Figure 4.11 Discharge #35503. Correlation of bolometer array signals (see diagnostic layout in figure 4.1) with the reference channel 4 ($\rho = 0.4$) for three modes appearing at different discharge conditions: a) before b) after c) back confinement transition.

a clear propagation structure is evident. After comparing figure 4.11b with figures 4.11a and 4.11c, the correlation pattern from an island structure, which is rotating and global, is clearly distinct from that of an acoustic mode, which is standing and localized.

4.6 Discussion

Acoustic modes have been identified in TJ-II as the cause of intense radiation (density) fluctuations, likely due to plasma compressibility during ECR heating. Unless the magnetic component is present, no direct mode-induced thermal or fast particle transport is observed. In order to determine the acoustic nature of these modes, GAM and ISW have been considered likely candidates owing to their capacity to compress plasma. On the one hand, GAM is induced by geodesic curvature, which is universal for toroidal devices, and it exhibits standing wave character for density perturbations in the poloidal plane, but it is toroidally symmetric. On the other hand, ISW is a longitudinal wave that is expected to propagate along the dominant magnetic field direction, i.e., toroidally. When comparing with TJ-II phenomenology, the coherent radiation fluctuations are compatible with standing-wave structures in the poloidal plane but the measured frequencies are lower than for standard GAM. This could be understood because the dispersion relation for energetic-particle-induced GAMs is affected by plasma parameters and the characteristics of the fast particle drive (see

e. g. [99, 112, 113]), which easily shifts the frequency down. However, the detected modes show also a toroidal structure: From our toroidal resolution the toroidal mode structure for the first harmonic must be $n = 1 + Nl$ where l is an integer and $N = 4$ is the periodicity of the TJ-II device. Since the closest frequency to the experimental result is found for $l = 0$, we have set $n = 1$ in Eq. (4.2) to draw figure 4.6. According to figure 4.9, the relation between harmonics of mode frequencies and toroidal mode number agrees with Eq. (4.2). Although at present these modes cannot be classified as GAM or ISW and a proper dispersion relation is needed to determine their nature, the acoustic mode amplitude increases when approaching the low density confinement transition, result similar to the reported behavior of the GAM observed in the tokamak ASDEX-Upgrade [114] when approaching the L-H confinement transition.

Chapter 5

Summary and discussion

In this Thesis, three broad types of MHD modes have been identified.

In chapter 2, we have identified two rotation states for the magnetic island: stable rotation scaling like the ExB drift and unstable rotation with an added diamagnetic drift. Stable rotation is compatible with stable L- or H-mode states. Using the parameters of the plasmas here studied the islands are expected to rotate with the ExB drift [115], in agreement with frequency scaling we have found. Faster ExB drifts related with the steepening of plasma profiles can enhance magnetic screening and island shrinking [116] during the H-mode, thus explaining why the rotation modes are strongly weakened despite the larger rotation speeds. The formation of the barriers at or by the magnetically resonant regions can render the latter unstable and give rise to bursting-chirping modes. As an indication for theoretical work, we conjecture that when the barrier resists the resonant layer is thin; when it breaks, transport flows cross rapidly this layer and establish a density gradient there. The islands structure grows again (increasing coherent magnetic fluctuations) in an environment where the rotation approaches the diamagnetic drift in the ExB frame [115]. A rapid relaxation of the density gradient in the resonant layer provokes the rapid frequency chirping-down. Owing to continuous energy supply in the centre, the gradients build up anew and the cycle restarts. Unfortunately, we do not have enough spatio-temporal resolution to distinguish local density flattening in the resonant locations.

In Chapter 3, we have identified three types of Alfvén waves in TJ-II: HAE, GAE and MIAE. We have proposed that MIAEs are due to new frequency gaps opened by the existence of magnetic islands. Furthermore, rotating islands interact with existing AEs giving rise to new modes of Alfvénic nature. This is important because conventional studies are based on MHD equilibria without considering islands. However this is an important ingredient because we have seen that not only new gaps can be opened by the islands, but also the the resulting MIAE can disturb GAE if they share a common mode number. This is also true for

rotating islands, which can interact with Alfvén waves, either disturbing them or exciting new modes.

In Chapter 4, acoustic modes are first identified in TJ-II during ECR heating at low line-averaged electron density. The poloidal modal structure is compatible with Geodesic Acoustic Modes (GAM). Toroidally, however, the modes show harmonics both in wave number and frequency, and they propagate counter to the magnetic field. The modes are found in the proximity of low-order rationals of the rotational transform and are excited by fast-electron populations, but they disappear at the onset of $-i$ -islands rotation. The strong relationship between fast electrons and mode excitation is evident in discharges where burst of HXR signals correlate with the bursting behavior of the mode intensity. According to the theoretical model first proposed by Fu [99], this is an indicator of net energy transfer in velocity space from the fast electrons –lost from the core– to the wave. Additionally, low order magnetic islands locked at the periphery are needed to enable for acoustic mode excitation by fast electrons. It is well known that in TJ-II, the confinement of fast electrons increases in the vicinity of a magnetic island [106, 27], thus providing a long enough time to favor wave-particle interaction. Actually, it is known that the population of fast electrons decreases dramatically when the confinement transition is approached [117], which is when the acoustic mode becomes undetectable and the island rotation mode becomes apparent. Note that, after the back transition, the acoustic mode is recovered possibly because the islands stop, thus easing again the accumulation of fast particles nearby.

In order to summarize, we recall that these studies have been performed in low magnetic shear plasmas. In these conditions, small islands that are not detrimental for plasma operation can have impact on both thermal and fast particle populations via MHD. Even if it is still not known what leads the complex dynamics of transport barriers and related confinement states, we pose the physics of magnetic islands as a necessary ingredient. With respect to Alfvén waves, magnetic islands can favor the appearance of new gaps, and also couple with other Alfvén eigenmode. Finally, owing to the ability of magnetic islands to modify the distribution of fast electrons, acoustic modes can be excited in their vicinity. If these aspects can be assessed, toroidal confinement devices may gain a way to act externally on: transport barrier quality, fast particles through interaction with Alfvén waves and, possibly, plasma turbulence due to the radial electric field component of acoustic modes. This could be tested in present-day stellarators (e.g. W7-X) using heating and configuration control techniques.

References

- [1] John Sheffield. The physics of magnetic fusion reactors. *Reviews of Modern Physics*, 66(3):1015, 1994.
- [2] Allen H. Boozer. Physics of magnetically confined plasmas. *Rev. Mod. Phys.*, 76:1071–1141, Jan 2005.
- [3] Mitsuru Kikuchi, Karl Lackner, and Minh Quang Tran. Fusion physics. 2012.
- [4] B.A. Carreras, G. Grieger, J.H. Harris, J.L. Johnson, J.F. Lyon, O. Motojima, F. Rau, H. Renner, J.A. Rome, K. Uo, M. Wakatani, and H. Wobig. Progress in stellarator/heliotron research: 1981–1986. *Nuclear Fusion*, 28(9):1613, 1988.
- [5] G Grieger, CD Beidler, H Maassberg, E Harmeyer, F Herrnegger, J Junker, J Kisslinger, W Lotz, P Merkel, J Nührenberg, et al. Physics and engineering studies for wendelstein 7-x. In *Proceedings of the 13th International Conference on Plasma Physics and Controlled Nuclear Fusion Research, Washington, DC*, volume 3, pages 525–532, 1990.
- [6] Allen H. Boozer. Non-axisymmetric magnetic fields and toroidal plasma confinement. *Nuclear Fusion*, 55(2):025001, 2015.
- [7] A. Reiman and H. Greenside. Calculation of three-dimensional mhd equilibria with islands and stochastic regions. *Computer Physics Communications*, 43(1):157 – 167, 1986.
- [8] RJ La Haye. Neoclassical tearing modes and their control). *Physics of Plasmas (1994-present)*, 13(5):055501, 2006.
- [9] G. Gantenbein, H. Zohm, G. Giruzzi, S. Günter, F. Leuterer, M. Maraschek, J. Meskat, Q. Yu, ASDEX Upgrade Team, and ECRH-Group (AUG). Complete suppression of neoclassical tearing modes with current drive at the electron-cyclotron-resonance frequency in asdex upgrade tokamak. *Phys. Rev. Lett.*, 85:1242–1245, Aug 2000.
- [10] Y. Narushima, K.Y. Watanabe, S. Sakakibara, K. Narihara, I. Yamada, Y. Suzuki, S. Ohdachi, N. Ohyabu, H. Yamada, Y. Nakamura, and the LHD Experimental Group. Dependence of spontaneous growth and suppression of the magnetic island on beta and collisionality in the lhd. *Nuclear Fusion*, 48(7):075010, 2008.
- [11] K. Narihara, K. Y. Watanabe, I. Yamada, T. Morisaki, K. Tanaka, S. Sakakibara, K. Ida, R. Sakamoto, N. Ohyabu, N. Ashikawa, M. Emoto, H. Funaba, M. Goto, H. Hayashi, H. Idei, K. Ikeda, S. Inagaki, N. Inoue, O. Kaneko, K. Kawahata,

- T. Kobuchi, A. Komori, S. Kubo, R. Kumazawa, S. Masuzaki, J. Miyazawa, S. Morita, O. Motojima, S. Murakami, S. Muto, T. Mutoh, Y. Nagayama, Y. Nakamura, H. Nakanishi, K. Nishimura, N. Noda, T. Notake, S. Ohdachi, Y. Oka, K. Ohkubo, M. Osakabe, S. Ozaki, B. J. Peterson, A. Sagara, K. Saito, H. Sasao, M. Sasao, K. Sato, M. Sato, T. Seki, T. Shimozuma, C. Shoji, S. Sudo, H. Suzuki, A. Takayama, M. Takechi, Y. Takeiri, N. Tamura, K. Toi, N. Tokuzawa, Y. Torii, K. Tsumori, T. Watari, H. Yamada, S. Yamaguchi, S. Yamamoto, K. Yamazaki, and Y. Yoshimura. Observation of the “self-healing” of an error field island in the large helical device. *Phys. Rev. Lett.*, 87:135002, Sep 2001.
- [12] C.C. Hegna. Healing of magnetic islands in stellarators by plasma flow. *Nuclear Fusion*, 51(11):113017, 2011.
- [13] Todd E. Evans, Richard A. Moyer, Keith H. Burrell, Max E. Fenstermacher, Ilon Joseph, Anthony W. Leonard, Thomas H. Osborne, Gary D. Porter, Michael J. Schaffer, Philip B. Snyder, Paul R. Thomas, Jonathan G. Watkins, and William P. West. Edge stability and transport control with resonant magnetic perturbations in collisionless tokamak plasmas. *Nat Phys*, 2(6):419–423, 06 2006.
- [14] R. Nazikian, C. Paz-Soldan, J. D. Callen, J. S. deGrassie, D. Eldon, T. E. Evans, N. M. Ferraro, B. A. Grierson, R. J. Groebner, S. R. Haskey, C. C. Hegna, J. D. King, N. C. Logan, G. R. McKee, R. A. Moyer, M. Okabayashi, D. M. Orlov, T. H. Osborne, J.-K. Park, T. L. Rhodes, M. W. Shafer, P. B. Snyder, W. M. Solomon, E. J. Strait, and M. R. Wade. Pedestal bifurcation and resonant field penetration at the threshold of edge-localized mode suppression in the dIII-d tokamak. *Phys. Rev. Lett.*, 114:105002, Mar 2015.
- [15] J.H. Harris, J.L. Cantrell, T.C. Hender, B.A. Carreras, and R.N. Morris. A flexible heliac configuration. *Nuclear Fusion*, 25(5):623, 1985.
- [16] Carlos Alejaldre, Jose Javier Alonso Gozalo, Jose Botija Perez, Francisco Castejón Magaña, Jose Ramon Cepero Diaz, Jose Guasp Perez, A Lopez-Fraguas, Luis García, Vladimir I Krivenski, R Martin, et al. Tj-ii project: a flexible heliac stellarator. *Fusion Science and Technology*, 17(1):131–139, 1990.
- [17] E Ascasíbar, J Qin, and A López-Fraguas. Magnetic surface mapping experiments in tj-ii heliac. In *J. Plasma Fusion Res. SERIES*. 1998.
- [18] A López-Fraguas, E Ascasíbar, JA Romero, I García-Cortés, JA Jiménez, A López Sánchez, J Quin, and M Otte. Magnetic surface mapping in tj-ii heliac. 2002.
- [19] FL Tabares, D Tafalla, Balbi, B Branas, T Estrada, Garci I, F Medina, MA Ochando, et al. Impact of wall conditioning and gas fuelling on the enhanced confinement modes in tj-ii. *Journal of nuclear materials*, 313:839–844, 2003.
- [20] D Tafalla, E de la Cal, B Brañas, and F.L Tabarés. Plasma–wall interaction in the spanish stellarator tj-ii. diagnostics and first results. *Journal of Nuclear Materials*, 266–269:1273 – 1278, 1999.

- [21] F L Tabarés, M A Ochando, F Medina, D Tafalla, J A Ferreira, E Ascasibar, R Balbín, T Estrada, C Fuentes, I García-Cortés, J Guasp, M Liniers, I Pastor, M A Pedrosa, and the TJ-II Team. Plasma performance and confinement in the TJ-II stellarator with lithium-coated walls. *Plasma Physics and Controlled Fusion*, 50(12):124051, 2008.
- [22] E. Ascasíbar, T. Estrada, M. Liniers, M. A. Ochando, F. L. Tabarés, D. Tafalla, J. Guasp, R. Jiménez-Gómez, F. Castejón, D. López-Bruna, A. López-Fraguas, I. Pastor, A. Cappa, C. Fuentes, J. M. Fontdecaba, and TJ-II Team. Global energy confinement studies in tj-ii nbi plasmas. *Contributions to Plasma Physics*, 50(6-7):594–599, 2010.
- [23] A. Baciero F. Castejón D. López-Bruna J. M. Fontdecaba M. Liniers K. J. McCarthy F. Medina I. Pastor B. Sun B. Zurro M. A. Ochando, E. Ascasíbar and the TJ-II Team. Study of tj-ii density limit dependence on magnetic configuration. In *41st EPS Conference on Plasma Physics*, page P2.074. European Physical Society, June 2014.
- [24] Ángela Fernández, Konstantin M Likin, Pedro Turullols, Jorge Teniente, Ramón Gonzalo, Carlos del Río, Javier Martí-Canales, Mario Sorolla, and Romualdo Martín. Quasioptical transmission lines for ecrh at tj-ii stellarator. *International Journal of Infrared and Millimeter Waves*, 21(12):1945–1957, 2000.
- [25] H Maassberg, CD Beidler, U Gasparino, M Romé, KS Dyabilin, NB Marushchenko, S Murakami, et al. The neoclassical “electron root” feature in the wendelstein-7-as stellarator. *Physics of Plasmas (1994-present)*, 7(1):295–311, 2000.
- [26] L Rodríguez-Rodrigo, F Medina, MA Ochando, A López Fraguas, and TJII Team. Generation of fast electrons in tj-ii. In *Proc. 26th EPS Conf. on Controlled Fusion and Plasma Physics, Maastricht, The Netherlands, ECA J*, volume 23, pages 353–356, 1999.
- [27] F Medina, MA Pedrosa, MA Ochando, L Rodriguez, C Hidalgo, AL Fraguas, BA Carreras, et al. Filamentary current detection in stellarator plasmas. *Review of Scientific Instruments*, 72(1):471–474, 2001.
- [28] C Fuentes, M Liniers, G Wolfers, J Alonso, G Marcon, R Carrasco, J Guasp, M Acedo, E Sánchez, M Medrano, et al. Neutral beam injection optimization at tj-ii. *Fusion engineering and design*, 74(1):249–253, 2005.
- [29] M. Ochando G. Wolfers J. A. Sebastián-R. Carrasco F. Martín B. Rojo K. J. McCarthy E. Ascasíbar B. Zurro M. Liniers, J. Guasp. A study of ion trajectories in the neutral beam duct of tj-ii stellarator. In *40 EPS Conference on Plasma Physics*, page P1.173. European Physical Society, June 2013.
- [30] J L Velasco, K Allmaier, A López-Fraguas, C D Beidler, H Maassberg, W Kernbichler, F Castejón, and J A Jiménez. Calculation of the bootstrap current profile for the tj-ii stellarator. *Plasma Physics and Controlled Fusion*, 53(11):115014, 2011.
- [31] MA Ochando, F Medina, B Zurro, A Baciero, KJ McCarthy, MA Pedrosa, C Hidalgo, E Sánchez, J Vega, AB Portas, et al. Up-down and in-out asymmetry monitoring based on broadband radiation detectors. *Fusion science and technology*, 50(2):313–319, 2006.

- [32] R. Jiménez-Gómez, A. Könies, E. Ascasíbar, F. Castejón, T. Estrada, L. G. Eliseev, A. V. Melnikov, J.A. Jiménez, D. G. Pretty, D. Jiménez-Rey, M.A. Pedrosa, A. de Bustos, and S. Yamamoto. Alfvén eigenmodes measured in the TJ-II stellarator. *Nuclear Fusion*, 51(3):033001, 2011.
- [33] F Medina, L Rodriguez-Rodrigo, J Encabo-Fernández, A López-Sánchez, P Rodriguez, and C Rueda. X-ray diagnostic systems for the tj-ii flexible heliac. *Review of scientific instruments*, 70(1):642–644, 1999.
- [34] I. García-Cortés, E. de la Luna, F. Castejón, J.A. Jiménez, E. Ascasíbar, B. Brañas, T. Estrada, J. Herranz, A. López-Fraguas, I. Pastor, J. Qin, J. Sánchez, F.L. Tabarés, D. Tafalla, V. Tribaldos, B. Zurro, TJ-II Team, and S.V. Shchepetov. Edge-localized-mode-like events in the tj-ii stellarator. *Nuclear Fusion*, 40(11):1867, 2000.
- [35] J A Jiménez, E de la Luna, I García-Cortés, and S V Shchepetov. Localized electromagnetic modes in mhd stable regime of the tj-ii heliac. *Plasma Physics and Controlled Fusion*, 48(5):515, 2006.
- [36] B.Ph. van Milligen, T. Estrada, R. Jiménez-Gómez, A. Melnikov, C. Hidalgo, J.M. Fontdecaba, L. Krupnik, L.G. Eliseev, S.V. Perfilov, and the TJ-II team. A global resonance phenomenon at the TJ-II stellarator. *Nuclear Fusion*, 51(1):013005, 2011.
- [37] Alexander V Melnikov, Leonid G Eliseev, Maria A Ochando, Kenichi Nagaoka, Enrique Ascasibar, Alvaro Cappa, Francisco Castejon, Teresa Estrada, Carlos Hidalgo, Sergey E Lysenko, et al. A quasi-coherent electrostatic mode in ecrh plasmas on tj-ii. *Plasma and Fusion Research*, 6:2402030–2402030, 2011.
- [38] M. A. Ochando, B. J. Sun, and D. López-Bruna. Long-lasting core coherent modes in tj-ii stellarator plasmas. In *Europhysics Conference Abstracts (42nd EPS Conference on Plasma Physics)*, volume 39E, page P4.161, Lisbonne, Portugal, June 2015.
- [39] L García, MA Ochando, BA Carreras, D Carralero, C Hidalgo, and B Ph van Milligen. Effect of fast electrons on the stability of resistive interchange modes in the tj-ii stellarator. *Physics of Plasmas (1994-present)*, 23(6):062319, 2016.
- [40] M. Greenwald, R. Boivin, P. Bonoli, R. Budny, C. Fiore, J. Goetz, R. Granetz, A. Hubbard, I. Hutchinson, J. Irby, B. LaBombard, Y. Lin, B. Lipschultz, E. Marmor, A. Mazurenko, D. Mossessian, T. Sunn Pedersen, C. S. Pitcher, M. Porkolab, J. Rice, W. Rowan, J. Snipes, G. Schilling, Y. Takase, J. Terry, S. Wolfe, J. Weaver, B. Welch, and S. Wukitch. Characterization of enhanced D_α high-confinement modes in Alcator C-Mod. *Physics of Plasmas*, 6(5):1943–1949, 1999.
- [41] A. E. Hubbard, R. L. Boivin, R. S. Granetz, M. Greenwald, J. W. Hughes, I. H. Hutchinson, J. Irby, B. LaBombard, Y. Lin, E. S. Marmor, A. Mazurenko, D. Mossessian, E. Nelson-Melby, M. Porkolab, J. A. Snipes, J. Terry, S. Wolfe, S. Wukitch, B. A. Carreras, V. Klein, and T. Sunn Pedersen. Pedestal profiles and fluctuations in c-mod enhanced d-alpha h-modes. *Physics of Plasmas*, 8(5):2033–2040, 2001.
- [42] A. E. Hubbard, D. G. Whyte, R. M. Churchill, I. Cziegler, A. Dominguez, T. Golfopoulos, J. W. Hughes, J. E. Rice, I. Bessmyatnov, M. J. Greenwald, N. Howard, B. Lipschultz, E. S. Marmor, M. L. Reinke, W. L. Rowan, J. L. Terry, and

- Alcator C-Mod Group. Edge energy transport barrier and turbulence in the i-mode regime on alcator c-mod(a). *Physics of Plasmas*, 18(5):056115, 2011.
- [43] K H Burrell, M E Austin, D P Brennan, J C DeBoo, E J Doyle, P Gohil, C M Greenfield, R J Groebner, L L Lao, T C Luce, M A Makowski, G R McKee, R A Moyer, T H Osborne, M Porkolab, T L Rhodes, J C Rost, M J Schaffer, B W Stallard, E J Strait, M R Wade, G Wang, J G Watkins, W P West, and L Zeng. Quiescent H-mode plasmas in the DIII-D tokamak. *Plasma Physics and Controlled Fusion*, 44(5A):A253, 2002.
- [44] T.H. Osborne, G.L. Jackson, Z. Yan, R. Maingi, D.K. Mansfield, B.A. Grierson, C.P. Chrobak, A.G. McLean, S.L. Allen, D.J. Battaglia, A.R. Briesemeister, M.E. Fenstermacher, G.R. McKee, P.B. Snyder, and The DIII-D Team. Enhanced h-mode pedestals with lithium injection in diii-d. *Nuclear Fusion*, 55(6):063018, 2015.
- [45] C P Perez, H R Koslowski, T C Hender, P Smeulders, A Loarte, P J Lomas, G Saibene, R Sartori, M Becoulet, T Eich, R J Hastie, G T A Huysmans, S Jachmich, A Rogister, F C Schüller, and JET EFDA contributors. Washboard modes as ELM-related events in JET. *Plasma Physics and Controlled Fusion*, 46(1):61, 2004.
- [46] F.L. Waelbroeck, I. Joseph, E. Nardon, M. Bécoulet, and R. Fitzpatrick. Role of singular layers in the plasma response to resonant magnetic perturbations. *Nuclear Fusion*, 52(7):074004, 2012.
- [47] K Toi, R Akiyama, H Arimoto, A Ejiri, K Ida, H Idei, H Iguchi, O Kaneko, K Kawahata, A Komori, S Kubo, K Matsuoka, T Morisaki, S Morita, K Nishimura, S Okamura, A Sagara, S Sakakibara, C Takahashi, Y Takita, K Tanaka, K Tsumori, J Xu, H Yamada, and I Yamada. H-mode transition in the chs heliotron/torsatron. *Plasma Physics and Controlled Fusion*, 36(7A):A117, 1994.
- [48] S Morita, T Morisaki, K Tanaka, S Masuzaki, M Goto, S Sakakibara, C Michael, K Narihara, S Ohdachi, R Sakamoto, A Sanin, K Toi, T Tokuzawa, L N Vyacheslavov, K Y Watanabe, and the LHD Experimental Group. Characteristics of H-mode-like discharges and elm activities in the presence of $\iota/2\pi = 1$ surface at the ergodic layer in LHD. *Plasma Physics and Controlled Fusion*, 48(5A):A269, 2006.
- [49] K Toi, S Ohdachi, F Watanabe, K Narihara, T Morisaki, S Sakakibara, S Morita, M Goto, K Ida, S Masuzaki, K Miyazawa, K Tanaka, T Tokuzawa, K W Watanabe, M Yoshinuma, and the LHD Experimental Group. Formation of edge transport barrier in the ergodic field layer of helical divertor configuration on the large helical device. *Plasma Physics and Controlled Fusion*, 48(5A):A295, 2006.
- [50] S Sakakibara, K Y Watanabe, Y Suzuki, Y Narushima, S Ohdachi, N Nakajima, F Watanabe, L Garcia, A Weller, K Toi, I Yamada, K Tanaka, T Tokuzawa, K Ida, H Yamada, A Komori, O Motojima, and the LHD Experimental Group. Mhd study of the reactor-relevant high-beta regime in the large helical device. *Plasma Physics and Controlled Fusion*, 50(12):124014, 2008.
- [51] I García-Cortés, D López-Bruna, F L Tabarés, T Estrada, F Medina, and the TJ-II Team. Spontaneous improvement of tj-ii plasmas confinement. *Plasma Physics and Controlled Fusion*, 44(8):1639–1649, 2002.

- [52] D López-Bruna, V I Vargas, and J A Romero. Are magnetic resonances practical transport controllers in fusion plasmas? the tj-ii experience. *Journal of Physics: Conference Series*, 591(1):012013, 2015.
- [53] D. López-Bruna, M.A. Ochando, A. López-Fraguas, F. Medina, and E. Ascasíbar. Relationship between mhd events, magnetic resonances and transport barriers in TJ-II plasmas. *Nuclear Fusion*, 53(7):073051, 2013.
- [54] D. López-Bruna, M. A. Pedrosa, M. A. Ochando, T. Estrada, B. P. van Milligen, A. López-Fraguas, J. A. Romero, D. Baião, F. Medina, C. Hidalgo, et al. Magnetic resonances and electric fields in the TJ-II heliac. *Plasma Physics and Controlled Fusion*, 53:124022, 2011.
- [55] T. Estrada, E. Ascasíbar, T. Happel, C. Hidalgo, E. Blanco, R. Jiménez-Gómez, M. Liniers, D. López-Bruna, F.L. Tabarés, and D. Tafalla. L-H transition experiments in TJ-II. *Contributions to Plasma Physics*, 50(6-7):501–506, 2010.
- [56] T. Estrada, E. Ascasíbar, E. Blanco, A. Cappa, F. Castejón, C. Hidalgo, B.Ph. van Milligen, and E. Sánchez. Limit cycle oscillations at the l–i–h transition in tj-ii plasmas: triggering, temporal ordering and radial propagation. *Nuclear Fusion*, 55(6):063005, 2015.
- [57] T Estrada, T Happel, L Eliseev, D López-Bruna, E Ascasíbar, E Blanco, L Cupido, J M Fontdecaba, C Hidalgo, R Jiménez-Gómez, L Krupnik, M Liniers, M E Manso, K J McCarthy, F Medina, A Melnikov, B van Milligen, M A Ochando, I Pastor, M A Pedrosa, F L Tabarés, D Tafalla, and TJ-II Team. Sheared flows and transition to improved confinement regime in the TJ-II stellarator. *Plasma Physics and Controlled Fusion*, 51(12):124015, 2009.
- [58] C. Hidalgo, M. A. Pedrosa, C. Silva, D. Carralero, E. Ascasibar, B. A. Carreras, T. Estrada, F. Tabarés, D. Tafalla, J. Guasp, M. Liniers, A. López-Fraguas, B. van Milligen, and M. A. Ochando. Multi-scale physics mechanisms and spontaneous edge transport bifurcations in fusion plasmas. *EPL (Europhysics Letters)*, 87(5):55002, 2009.
- [59] A.V. Melnikov, L.G. Eliseev, T. Estrada, E. Ascasibar, A. Alonso, A.A. Chmyga, C. Hidalgo, A.D. Komarov, A.S. Kozachek, L.I. Krupnik, S.M. Khrebtov, M. Liniers, S.E. Lysenko, J.L. de Pablos, I. Pastor, M.A. Pedrosa, S.V. Perfilov, M.V. Ufimtsev, and Yu.I. Tashchev. Changes in plasma potential and turbulent particle flux in the core plasma measured by heavy ion beam probe during L–H transitions in the TJ-II stellarator. *Nuclear Fusion*, 53(9):092002, 2013.
- [60] J L Velasco and F Castejón. Study of the neoclassical radial electric field of the tj-ii flexible heliac. *Plasma Physics and Controlled Fusion*, 54(1):015005, 2012.
- [61] C Gutiérrez-Tapia, J J Martinell, D López-Bruna, A V Melnikov, L Eliseev, C Rodríguez, M A Ochando, F Castejón, J García, B P van Milligen, and J M Fontdecaba. Analysis of TJ-II experimental data with neoclassical formulations of the radial electric field. *Plasma Physics and Controlled Fusion*, 57(11):115004, 2015.

- [62] D. López-Bruna, J. A. Romero, A. López-Fraguas, J. M. Reynolds, E. Blanco, T. Estrada, M. A. Ochando, R. Jiménez-Gómez, O. Bondarenko, D. Tafalla, J. Herranz, E. Ascasíbar, V. I. Vargas, and TJ-II Team. Magnetic resonances in ECR-heated plasmas of the TJ-II heliac. *Contributions to Plasma Physics*, 50(6-7):600–604, 2010.
- [63] F L Tabarés, E. Ascasibar, E. Blanco, F. Medina, I. Pastor, and Tafalla. Direct generation of NBI plasmas in TJ-II with lithium-coated walls. *Stellarator News*, (144):1–3, 2014.
- [64] M.A. Pedrosa, C. Silva, C. Hidalgo, D. Carralero, B. van Milligen, and J. Morera. Inward and outward propagation of the floating potential fluctuations in the plasma edge of the tj-ii stellarator. *Nuclear Fusion*, 51(7):073027, 2011.
- [65] F.L. Tabarés, M. Ochando, D. Tafalla, F. Medina, K. McCarthy, J. M. Fontdecaba, M. Liniers, J. Guasp, E. Ascasíbar, T. Estrada, I. Pastor, and TJ-II Team. Energy and particle balance studies under full boron and lithium-coated walls in TJ-II. *Contributions to Plasma Physics*, 50(6-7):610–615, 2010.
- [66] J. Sánchez, M. Acedo, A. Alonso, J. Alonso, P. Alvarez, E. Ascasíbar, A. Baciero, R. Balbín, L. Barrera, E. Blanco, J. Botija, A. de Bustos, E. de la Cal, I. Calvo, A. Cappa, J.M. Carmona, D. Carralero, R. Carrasco, B.A. Carreras, F. Castejón, R. Castro, G. Catalán, A.A. Chmyga, M. Chamorro, L. Eliseev, L. Esteban, T. Estrada, A. Fernández, R. Fernández-Gavilán, J.A. Ferreira, J.M. Fontdecaba, C. Fuentes, L. García, I. García-Cortés, R. García-Gómez, J.M. García-Regaña, J. Guasp, L. Guimaraes, T. Happel, J. Hernanz, J. Herranz, C. Hidalgo, J.A. Jiménez, A. Jiménez-Denche, R. Jiménez-Gómez, D. Jiménez-Rey, I. Kirpichev, A.D. Komarov, A.S. Kozachok, L. Krupnik, F. Lapayese, M. Liniers, D. López-Bruna, A. López-Fraguas, J. López-Rázola, A. López-Sánchez, S. Lysenko, G. Marcon, F. Martín, V. Maurin, K.J. McCarthy, F. Medina, M. Medrano, A.V. Melnikov, P. Méndez, B. van Milligen, E. Mirones, I.S. Nedzelskiy, M. Ochando, J. Olivares, J.L. de Pablos, L. Pacios, I. Pastor, M.A. Pedrosa, A. de la Peña, A. Pereira, G. Pérez, D. Pérez-Risco, A. Petrov, S. Petrov, A. Portas, D. Pretty, D. Rapisarda, G. Rattá, J.M. Reynolds, E. Rincón, L. Ríos, C. Rodríguez, J.A. Romero, A. Ros, A. Salas, M. Sánchez, E. Sánchez, E. Sánchez-Sarabia, K. Sarkisian, J.A. Sebastián, C. Silva, S. Schepetov, N. Skvortsova, E.R. Solano, A. Soletto, F. Tabarés, D. Tafalla, A. Tarancón, Yu. Tashev, J. Tera, A. Tolkachev, V. Tribaldos, V.I. Vargas, J. Vega, G. Velasco, J.L. Velasco, M. Weber, G. Wolfers, and B. Zurro. Confinement transitions in TJ-II under Li-coated wall conditions. *Nuclear Fusion*, 49:104018, 2009.
- [67] A. Hasegawa and C. Uberoi. Alfvén waves. Doe critical review series, Department of Energy, Washington, DC (USA), 1982.
- [68] WW Heidbrink. Basic physics of alfvén instabilities driven by energetic particles in toroidally confined plasmas. *Physics of Plasmas (1994-present)*, 15(5):055501, 2008.
- [69] C.Z Cheng, Liu Chen, and M.S Chance. High-n ideal and resistive shear alfvén waves in tokamaks. *Annals of Physics*, 161(1):21 – 47, 1985.
- [70] S. Yamamoto, K. Toi, N. Nakajima, S. Ohdachi, S. Sakakibara, K. Y. Watanabe, M. Goto, K. Ikeda, O. Kaneko, K. Kawahata, S. Masuzaki, T. Morisaki, S. Morita,

- S. Murakami, K. Narihara, Y. Oka, M. Osakabe, Y. Takeiri, K. Tanaka, T. Tokuzawa, K. Tsumori, H. Yamada, I. Yamada, and K. Yamazaki. Observation of helicity-induced alfvén eigenmodes in large-helical-device plasmas heated by neutral-beam injection. *Phys. Rev. Lett.*, 91:245001, Dec 2003.
- [71] Alessandro Biancalani, Liu Chen, Francesco Pegoraro, and Fulvio Zonca. Continuous spectrum of shear alfvén waves within magnetic islands. *Phys. Rev. Lett.*, 105:095002, Aug 2010.
- [72] C. R. Cook and C. C. Hegna. Analytical theory of the shear alfvén continuum in the presence of a magnetic island. *Physics of Plasmas*, 22(4):–, 2015.
- [73] W. Chen, Z. Qiu, X. T. Ding, H. S. Xie, L. M. Yu, X. Q. Ji, J. X. Li, Y. G. Li, J. Q. Dong, Z. B. Shi, Y. P. Zhang, J. Y. Cao, X. M. Song, S. D. Song, M. Xu, Q. W. Yang, Yi. Liu, L. W. Yan, and X. R. Duan. Observation and theory of nonlinear mode couplings between shear alfvén wave and magnetic island in tokamak plasmas. *EPL (Europhysics Letters)*, 107(2):25001, 2014.
- [74] S V Annibaldi, F Zonca, and P Buratti. Excitation of beta-induced alfvén eigenmodes in the presence of a magnetic island. *Plasma Physics and Controlled Fusion*, 49(4):475, 2007.
- [75] M. A. Ochando, D López-Bruna, F Medina, A Cappa, E Ascasíbar, A López-Fraguas, S Yamamoto, and the TJ-II Team. Plasma current dependence of coherent modes frequency in low-density NBI heated discharges in the TJ-II stellarator. In *39th EPS Conference on Plasma Physics, Europhysics Conference Abstracts*, volume 36F, page P4.063, july 2012.
- [76] D. A. Spong, R. Sanchez, and A. Weller. Shear alfvén continua in stellarators. *Physics of Plasmas (1994-present)*, 10(8):3217–3224, 2003.
- [77] S. P. Hirshman, W. I. van Rij, and P. Merkel. Three-dimensional free boundary calculations using a spectral green’s function method. *Comput. Phys. Comm.*, 43(3):143, 1986.
- [78] B. Ph. van Milligen, T. Estrada, E. Ascasibar, D. Tafalla, D. Lopez-Bruna, A. Lopez Fraguas, J. A. Jimenez, I. Garcia-Cortes, A. Dinklage, and R. Fischer. Integrated data analysis at tj-ii: The density profile. *Review of Scientific Instruments*, 82(7):073503, 2011.
- [79] D. López-Bruna, J.A. Romero, R. Jiménez-Gómez, M.A. Pedrosa, M. Ochando, T. Estrada, A. López-Fraguas, F. Medina, J. Herranz, T. Kalhoff, E. Ascasíbar, A. de la Peña, F. Lapayese, and J. Alonso. First dynamic magnetic configuration scans in ecrh plasmas of the TJ-II heliac. *Nuclear Fusion*, 49(8):085016, 2009.
- [80] B.Ph. van Milligen, L. García, B.A. Carreras, M.A. Pedrosa, C. Hidalgo, J.A. Alonso, T. Estrada, and E. Ascasíbar. Mhd mode activity and the velocity shear layer at tj-ii. *Nuclear Fusion*, 52(1):013006, 2012.
- [81] B J Sun, D López-Bruna, M A Ochando, and M A Pedrosa. Low frequency coherent modes in TJ-II plasmas. In *41st European Physical Society Conference on Plasma Physics, ECA*, volume 38, page P2.090, 2014.

- [82] D. López-Bruna, F. Castejón, T. Estrada, J.A. Romero, J.A. Jiménez, E. Ascasíbar, and the TJ-II Team. Effects of ohmic current in the TJ-II stellarator. *Nuclear Fusion*, 44(5):645, 2004.
- [83] J.A. Romero, L. Pacios, A. de la Peña, F. Lapayese, and E. Ascasíbar. Magnetic configuration sweep control in heliac type stellarators. *Nuclear Fusion*, 54(4):043008, 2014.
- [84] A.V. Melnikov, M. Ochando, E. Ascasibar, F. Castejon, A. Cappa, L.G. Eliseev, C. Hidalgo, L.I. Krupnik, A. Lopez-Fraguas, M. Liniers, S.E. Lysenko, J.L. de Pablos, S.V. Perfilov, S.E. Sharapov, D.A. Spong, J.A. Jimenez, M.V. Ufimtsev, B.N. Breizman, HIBP group, and the TJ-II team. Effect of magnetic configuration on frequency of nbi-driven alfvén modes in tj-ii. *Nuclear Fusion*, 54(12):123002, 2014.
- [85] S da Graça, G D Conway, P Lauber, M Maraschek, D Borba, S Günter, L Cupido, K Sassenberg, F Serra, M E Manso, the CFN reflectometry group, and the ASDEX Upgrade Team. Localization of mhd and fast particle modes using reflectometry in asdex upgrade. *Plasma Physics and Controlled Fusion*, 49(11):1849, 2007.
- [86] N. A. Crocker, W. A. Peebles, S. Kubota, E. D. Fredrickson, S. M. Kaye, B. P. LeBlanc, and J. E. Menard. Three-wave interactions between fast-ion modes in the national spherical torus experiment. *Phys. Rev. Lett.*, 97:045002, Jul 2006.
- [87] K Toi, F Watanabe, T Tokuzawa, A Shimizu, T Ido, K Ida, S Ohdachi, S Sakakibara, S Yamamoto, H Funaba, et al. Nonlinear interaction between alfvén eigenmode and geodesic acoustic mode excited by energetic ions in the large helical device. In *European Conference Abstracts, 35th EPS Plasma Physics Conference*, volume 32D, page P1.054, 2008.
- [88] S Zegenhagen. *Destabilization of Alfvén Eigenmodes by Fast Particles in W7-AS*. Dr. rer. nat., Mathematisch-Naturwissenschaftlichen Fakultät, Greifswald, Germany, Ernst-Moritz-Arndt-University, February 2006.
- [89] M Hirsch, J Baldzuhn, C Beidler, R Brakel, R Burhenn, A Dinklage, H Ehmler, M Endler, V Erckmann, Y Feng, J Geiger, L Giannone, G Grieger, P Grigull, H-J Hartfuß, D Hartmann, R Jaenicke, R König, H P Laqua, H Maaßberg, K McCormick, F Sardei, E Speth, U Stroth, F Wagner, A Weller, A Werner, H Wobig, S Zoletnik, and for the W7-AS Team. Major results from the stellarator Wendelstein 7-AS. *Plasma Physics and Controlled Fusion*, 50(5):053001, 2008.
- [90] S Yamamoto, E Ascasíbar, R Jiménez-Goméz, S Kobayashi, S Ohshima, K Nagaoka, D Spong, B Blackwell, D Pretty, K Nagasaki, et al. Studies of energetic-ion-driven mhd instabilities in helical plasmas with low magnetic shear. In *Proc. 24th Int. Conf. on Fusion Energy (San Diego, CA, 2012)*, pages 5–2, 2012.
- [91] S Yamamoto, K Nagasaki, Y Suzuki, T Mizuuchi, H Okada, S Kobayashi, B Blackwell, K Kondo, G Motojima, N Nakajima, et al. Observation of magnetohydrodynamic instabilities in Heliotron J plasmas. *Fusion science and technology*, 51(1):92–96, 2007.

- [92] H. Peraza-Rodríguez, R. Sánchez, J. Geiger, J.M. Reynolds, and V. Tribaldos. Application of the siesta code to the calculation of mhd equilibria for the wendelstein 7-x stellarator. In *41st EPS Conference on Plasma Physics*, page P2.072, Berlin, 23 - 27 June 2014. European Physical Society.
- [93] Niels Winsor, John L. Johnson, and John M. Dawson. Geodesic acoustic waves in hydromagnetic systems. *Physics of Fluids*, 11(11):2448–2450, 1968.
- [94] P H Diamond, S-I Itoh, K Itoh, and T S Hahm. Zonal flows in plasma—a review. *Plasma Physics and Controlled Fusion*, 47(5):R35, 2005.
- [95] George R McKee, Raymond J Fonck, Marcin Jakubowski, Keith H Burrell, Klaus Hallatschek, Rick A Moyer, Dmitry L Rudakov, W Nevins, Gary D Porter, Paul Schoch, et al. Experimental characterization of coherent, radially-sheared zonal flows in the diiii-d tokamak. *Physics of Plasmas (1994-present)*, 10(5):1712–1719, 2003.
- [96] G D Conway, B Scott, J Schirmer, M Reich, A Kendl, and the ASDEX Upgrade Team. Direct measurement of zonal flows and geodesic acoustic mode oscillations in asdex upgrade using doppler reflectometry. *Plasma Physics and Controlled Fusion*, 47(8):1165, 2005.
- [97] K. J. Zhao, T. Lan, J. Q. Dong, L. W. Yan, W. Y. Hong, C. X. Yu, A. D. Liu, J. Qian, J. Cheng, D. L. Yu, Q. W. Yang, X. T. Ding, Y. Liu, and C. H. Pan. Toroidal symmetry of the geodesic acoustic mode zonal flow in a tokamak plasma. *Phys. Rev. Lett.*, 96:255004, Jun 2006.
- [98] CJ Boswell, HL Berk, DN Borba, Tomas Johnson, SD Pinches, and SE Sharapov. Observation and explanation of the jet $n=0$ chirping mode. *Physics Letters A*, 358(2):154–158, 2006.
- [99] G. Y. Fu. Energetic-particle-induced geodesic acoustic mode. *Phys. Rev. Lett.*, 101:185002, Oct 2008.
- [100] R. Nazikian, G. Y. Fu, M. E. Austin, H. L. Berk, R. V. Budny, N. N. Gorelenkov, W. W. Heidbrink, C. T. Holcomb, G. J. Kramer, G. R. McKee, M. A. Makowski, W. M. Solomon, M. Shafer, E. J. Strait, and M. A. Van Zeeland. Intense geodesic acousticlike modes driven by suprathermal ions in a tokamak plasma. *Phys. Rev. Lett.*, 101:185001, Oct 2008.
- [101] A V Melnikov, V A Vershkov, L G Eliseev, S A Grashin, A V Gudozhnik, L I Krupnik, S E Lysenko, V A Mavrin, S V Perfilov, D A Shelukhin, S V Soldatov, M V Ufimtsev, A O Urazbaev, G Van Oost, and L G Zimeleva. Investigation of geodesic acoustic mode oscillations in the t-10 tokamak. *Plasma Physics and Controlled Fusion*, 48(4):S87, 2006.
- [102] W Chen, XT Ding, LM Yu, XQ Ji, JQ Dong, QW Yang, Yi Liu, LW Yan, Y Zhou, W Li, et al. Egam induced by energetic electrons and nonlinear interactions among egam, baes and tearing modes in a toroidal plasma. *Physics Letters A*, 377(5):387–390, 2013.

- [103] H. Y. W. Tsui, K. Rypdal, Ch. P. Ritz, and A. J. Wootton. Coherent nonlinear coupling between a long-wavelength mode and small-scale turbulence in the text tokamak. *Phys. Rev. Lett.*, 70:2565–2568, Apr 1993.
- [104] T. Ido, M. Osakabe, A. Shimizu, T. Watari, M. Nishiura, K. Toi, K. Ogawa, K. Itoh, I. Yamada, R. Yasuhara, Y. Yoshimura, S. Kato, and The LHD Experiment Group. Identification of the energetic-particle driven gam in the lhd. *Nuclear Fusion*, 55(8):083024, 2015.
- [105] C. B. Deng, D. L. Brower, B. N. Breizman, D. A. Spong, A. F. Almagri, D. T. Anderson, F. S. B. Anderson, W. X. Ding, W. Guttenfelder, K. M. Likin, and J. N. Talmadge. Energetic-electron-driven instability in the helically symmetric experiment. *Phys. Rev. Lett.*, 103:025003, Jul 2009.
- [106] M. A. Ochando, F. Medina, L. Rodríguez-Rodrigo, M. A. Pedrosa, C. Hidalgo, and the TJ-II Team. Confinement of fast electrons at rational surfaces in the TJ-II stellarator. In *Proc. 12th IAEA Int. Stellarator Workshop*, Madison (WI) USA, 1999.
- [107] F. Zonca and L. Chen. Radial structures and nonlinear excitation of geodesic acoustic modes. *EPL (Europhysics Letters)*, 83(3):35001, 2008.
- [108] R. Nazikian. Nonlinear evolution and radial propagation of the energetic particle induced geodesic acoustic mode on diii-d. In *5th IAEA Technical Meeting on the "Theory of Plasma Instabilities"*, September 2011.
- [109] G. Y. FU. On nonlinear self-interaction of geodesic acoustic mode driven by energetic particles. *Journal of Plasma Physics*, 77:457–467, 8 2011.
- [110] D Carralero, I Calvo, S da Graça, B A Carreras, T Estrada, M A Pedrosa, and C Hidalgo. Shear-flow susceptibility near the low-density transition in tj-ii. *Plasma Physics and Controlled Fusion*, 54(6):065006, 2012.
- [111] B. J. Sun, D. López-Bruna, M. A. Ochando, and M. A. Pedrosa. Magnetic island rotation in TJ-II plasmas. In *42nd EPS Conference on Plasma Physics*, page P4.162. European Physical Society, June 2015.
- [112] D. Zarzoso, X. Garbet, Y. Sarazin, R. Dumont, and V. Grandgirard. Fully kinetic description of the linear excitation and nonlinear saturation of fast-ion-driven geodesic acoustic mode instability. *Physics of Plasmas*, 19(2), 2012.
- [113] D. Zarzoso, A. Biancalani, A. Bottino, Ph. Lauber, E. Poli, J.-B. Girardo, X. Garbet, and R.J. Dumont. Analytic dispersion relation of energetic particle driven geodesic acoustic modes and simulations with nemorb. *Nuclear Fusion*, 54(10):103006, 2014.
- [114] G. D. Conway, C. Angioni, F. Ryter, P. Sauter, and J. Vicente. Mean and oscillating plasma flows and turbulence interactions across the *l-h* confinement transition. *Phys. Rev. Lett.*, 106:065001, Feb 2011.
- [115] F. L. Waelbroeck. Theory and observations of magnetic islands. *Nuclear Fusion*, 49(10):104025, 2009.

-
- [116] Y. Narushima, F. Castejón, S. Sakakibara, K.Y. Watanabe, S. Ohdachi, Y. Suzuki, T. Estrada, F. Medina, D. López-Bruna, M. Yokoyama, M. Yoshinuma, K. Ida, S. Nishimura, LHD Experiment Group, and TJ-II Experiment Group. Experimental study of the poloidal flow effect on magnetic island dynamics in lhd and tj-ii. *Nuclear Fusion*, 51(8):083030, 2011.
- [117] V. I. Vargas, D. López-Bruna, J. Guasp, J. Herranz, T. Estrada, F. Medina, M.A. Ochando, J. L. Velasco, J. M. Reynolds, J. A. Ferreira, D. Tafalla, F. Castejon, and A. Salas. Density dependence of particle transport in ECH plasmas of the TJ-II stellarator. Technical Report 1162, Ciemat, Madrid, Spain, Febrero 2009.